UNIVERSITY OF CALIFORNIA
SANTA CRUZ

SEARCH FOR WW AND WZ RESONANCE PRODUCTION IN $\ell\nu qq$ FINAL STATES IN pp COLLISIONS AT $\sqrt{s} = 13$ TEV WITH THE ATLAS DETECTOR

A dissertation submitted in partial satisfaction of the requirements for the degree of

DOCTOR OF PHILOSOPHY

in

PHYSICS

by

Natasha Woods

December 2019

The Dissertation of Natasha Woods is approved:

Abraham Seiden, Chair

Mike Hance

Bruce Schumm

Quentin Williams
Vice Provost and Dean of Graduate Studies

Table of Contents

List of Figures

List of Tables

Abstract

Search for WW and WZ resonance production in $\ell\nu qq$ final states in pp collisions at $\sqrt{s} = 13$ TeV with the ATLAS detector

by

Natasha Woods

This thesis reviews a search for WW and WZ resonance production using data from pp collisions at $\sqrt{s} = 13$ TeV using the ATLAS detector, corresponding to an integrated luminosity of 139 fb^{-1}. Diboson resonances are predicted in a number of Standard Model (SM) extensions, such as Extended Gauge Models, Extra dimensions, and technicolor models. This search looks for resonances where one W boson decays leptonically and the other W or Z boson decays hadronically. This serach is sensitive to diboson resonance production via vector-boson fusion as well as quark-antiquark annihilation and gluon-gluon fusion mechanisms. No significant excess of events is observed with respect to the Standard Model backgrounds. As the dominant backgrounds in this search contain gluons, classifying jets as quark or gluon intiated would make this analysis more sensitive to new physics. Towards this end, this thesis considers the prospects for adding a quark gluon tagger based on the number of tracks in jets and reviews the calibration of the number of tracks in jets.

A loving dedication.

å

Acknowledgments

Proper acknowledgments of everyone else who helped you graduate. Write later.

another intro???

Part I

Theoretical Motivation

Chapter 1

The Standard Model of Particle Physics

1.1 Introduction

By determining the dynamics of the most elementary degrees of freedom, particle physics hopes to uncover the fundamental laws of the universe. The definition of elementary has evolved through time and currently refers to matter and force mediating particles: fermions and bosons, respectively. The Standard Model of Particle Physics (SM) describes the quantum behavior of three of the four fundamental forces: weak, strong, and electromagnetic, via boson and fermion interactions. Gravity is not included in the SM and still under investigation.

1.2 Quantum Field Theory

In the SM, forces (and particles) are represented as fields. In this context, fields are mathematical objects that define a tensor (e.g. scalar, vector, etc) at every point on a manifold, here the manifold is space-time. These fields obey laws dictated by Quantum Field Theory (QFT). Particles arise naturally in QFT as quantizied field excitations localized in spacetime.

According to Noether's theorem, symmetries of a field give rise to conserved quantities (e.g. time-translation invariance leads to energy conservation). Often in the history of physics, a conserved quantity of a field is found and then the underlying symmetry of the field is inferred. Gauge symmetries are symmetries among the internal degrees of freedom of the field (components of the tensor), which give rise to quantities associated with fields. By specifying the symmetries of a system the dynamics and conserved quantities of the system may be succinctly defined.

1.3 $U(1)_{EM}$ Local Gauge Invariance

The Lagrangian of Quantum Electrodynamics (QED) describes the electromagnetic force. QED may be derived by requiring local $U(1)_{EM}$ gauge invariance of the free dirac fermion Lagrangian, ψ:

$$\mathcal{L} = i\bar{\psi}\gamma^{\mu}\partial_{\mu}\psi - m\bar{\psi}\psi \tag{1.1}$$

This symmetry may be represented as a complex number with unit modulus, $e^{i\theta}$. U(1) gauge invariance requries this gauge transformation of ψ will leave the Lagrangian unchanged.

$$\psi(x) \to \psi'(x) = e^{i\theta(x)}\psi(x) \tag{1.2}$$

NB: This transformation is a local gauge transformation as θ depends on the spacetime coordinate.

By requiring this symmetry of the free Dirac fermion Lagrangian:

$$\mathcal{L} = i\bar{\psi}\gamma^\mu \partial_\mu \psi - m\bar{\psi}\psi \tag{1.3}$$

The mass term is unaffected, but the kinetic term is modified due to $\theta(x)$.

$$\mathcal{L} \to \mathcal{L}' = i\bar{\psi}e^{-i\theta(x)}\gamma^\mu \partial_\mu \psi e^{i\theta(x)} - m\bar{\psi}e^{-i\theta(x)}\psi e^{i\theta(x)} \tag{1.4}$$

$$= i\psi\gamma^\mu(\partial_\mu\psi + i\psi\partial_\mu\theta) - m\bar{\psi}\psi \tag{1.5}$$

The $\partial_\mu\theta$ terms breaks the gauge invariance of the Lagrangian. By introducing a new field, A_μ we can recover the gauge invariance of the derivative. Now redefining the derivative as the covariant derivative:

$$D_\mu\psi \equiv (\partial_\mu - iqA_\mu)\psi \tag{1.6}$$

And letting A_μ transform under U(1) as:

$$A_\mu \to A_\mu + \delta A_\mu \tag{1.7}$$

The transformed covariant derivative becomes:

$$D_\mu\psi \to D_\mu\psi' = (\partial_\mu - iqA_\mu)\psi' \tag{1.8}$$

$$= (\partial_\mu - iq(A_\mu + \delta A_\mu))\psi e^{i\theta} \tag{1.9}$$

$$= e^{i\theta}D_\mu + ie^{i\theta}\psi(\partial_\mu\theta - q\delta A_\mu)) \tag{1.10}$$

The covariant derivative can be made gauage invariant by setting the last term to zero.

$$\delta A_\mu = \frac{1}{q}\partial_\mu \theta \tag{1.11}$$

So now A_μ transforms as:

$$A_\mu \to A_\mu + \frac{1}{q}\partial_\mu \theta \tag{1.12}$$

Finally, replacing the derivative with the covariant derivative the Dirac Lagrangian we have:

$$\mathcal{L} = i\bar{\psi}\gamma^\mu D_\mu \psi - m\bar{\psi}\psi - \frac{1}{4}F_{\mu\nu}F^{\mu\nu} \tag{1.13}$$

$$= \mathcal{L}_{QED} \tag{1.14}$$

Here $F_{\mu\nu} \equiv \partial_\mu A_\nu - \partial_\nu A_\mu$. This last term in the Lagrangian is the kinetic energy of the gauge boson field.

So we have derived the QED Lagrangian. By requiring the free Dirac Lagrangian to be invariant under U(1) transformations we have generated a new gauge boson field, A_μ, which describes the photon. As expected the photon interacts with fermions.

Stepping back, a global U(1) gauge symmetry of the free Dirac Lagrangian implies we cannot measure the absolute phase of a charged particle. A local U(1) gauge symmetry changes the phase of fields differently across space time. For this type of transformation to leave the Lagrangian invariant, we had to introduce an additional field, A_μ, which "communicates" these phase changes across space-time. In less formal language this effectively means: if the field at one location changes, this change is conferred to other particles via A_μ.

1.4 Yang-Mills Gauge Theories

Requiring $U(1)_{EM}$ gauge invariance of the free Dirac Lagrangian gave us QED. Requiring different gauge symmetries we can derive the structure of other interactions. Any gauge symmetry may be written as:

$$\psi_i \to exp(i\theta^a T^a_{ij})\psi_j \tag{1.15}$$

Here θ is a dimensionless real parameter and T is the generator of the gauge symmetry group. With this the covariant derivative can be written as:

$$D_\mu \psi_i \equiv \partial_\mu \psi_i + igA^a_\mu T^a_{ij}\psi_j \tag{1.16}$$

Then the gauge field must transform as:

$$A^a_\mu \to A^a_\mu - \frac{1}{g}\partial_\mu \theta^a - f^{abc}\theta^b A^c_\mu \tag{1.17}$$

Here f is the structure constant of the gauge group. The field strength tensor is given by:

$$F^a_{\mu\nu} \equiv \partial_\mu A^a_\nu - \partial_\nu A^a_\mu - gf^{abc}A^b_\mu A^c_\nu \tag{1.18}$$

$$F^a_{\mu\nu} \to F^a_{\mu\nu} - f^{abc}\theta^b F^c_{\mu\nu} \tag{1.19}$$

This gives the Yang-Mills Lagrangian:

$$\mathcal{L}_{YM} = -\frac{1}{4}F^{a\mu\nu}F^a_{\mu\nu} + i\bar{\psi_i}\gamma^\mu D_\mu \psi_i + m\bar{\psi_i}\psi_i \tag{1.20}$$

1.5 Particles in the Standard Model

The SM consists of fermions (half-interger spin matter constituents) and bosons (integer spin force meditators). Fermions are spinor representations of the Poincare group and can be further separated into leptons and quarks. Bosons are the result of requiring a particular symmetry among the spinor fields:

$$SU(3)_C \times SU(2)_L \times U(1)_Y \tag{1.21}$$

$SU(3)_C$ is the symmetry group of the strong force and generates eight gluon fields, G_μ. $SU(2)_L$ is the symmetry group of the Electroweak force and generates three electroweak boson fields, and $U(1)_Y$ generates the photon field, where Y is the weak-hypercharge:

$$Y = 2(Q - T_3) \tag{1.22}$$

Q is the electromagnetic charge, and T_3 is the z-component of the weak isospin. Weak isospin is the charge associated with the $SU(2)_L$ symmetry. The corresponding covariant derivative is then:

$$D_\mu \phi \equiv (\partial_\mu + ig_1 B_\mu Y_{L/R} + [ig_2 W_\mu^\alpha T^\alpha]_L + [ig_3 G_\mu^\alpha \tau^\alpha]_C)\psi \tag{1.23}$$

It is important to note that the gauge symmetry of the SM yields a particular structure of the fermion representations. So for a given fermion to interact with a given gauge field it must have a non-zero corresponding Noether charge for that gauge symmetry. If the corresponding Noether charge is zero, that fermion transforms as a singlet and does not participate in that gauge interaction.

Fermions are divided into quarks and leptons based on their transformations under $SU(3)_C$. Quarks transform as color triplets. Leptons transform as color singlets and consequently do not interact with gluons. Fermions may be further classified by their $SU(2)_L$ interactions. Only the left-chiral part of fermions (denoted by L here) transform as $SU(2)_L$ doublets, the right-chiral part forms singlets under this gauge. Lastly, all these groups of particles come in three generations, each a heavier copy of the previous, but with differing flavor quantum numbers. This is summarized in Table 1.1 and shown in Figures 1.1 and 1.2.

SM Fermion Gauge Group	First Generation	Second Generation	Third Generation	$(SU(3)_C, SU(2)_L, U(1)_Y)$ Representations
Left-handed quarks	$\begin{pmatrix} u_L^r & u_L^g & u_L^b \\ d_L^r & d_L^g & d_L^b \end{pmatrix}$	$\begin{pmatrix} c_L^r & c_L^g & c_L^b \\ s_L^r & s_L^g & s_L^b \end{pmatrix}$	$\begin{pmatrix} t_L^r & t_L^g & t_L^b \\ b_L^r & b_L^g & b_L^b \end{pmatrix}$	$(3, 2, \frac{1}{6})$
Right-handed quarks	(u_R^r, u_R^g, u_R^b) (d_R^r, d_R^g, d_R^b)	(c_R^r, c_R^g, c_R^b) (s_R^r, s_R^g, s_R^b)	(t_R^r, t_R^g, t_R^b) (b_R^r, b_R^g, b_R^b)	$(3, 1, \frac{2}{3})$ $(3, 1, -\frac{1}{3})$
Left-handed leptons	$\begin{pmatrix} \nu_e^L \\ e_L \end{pmatrix}$	$\begin{pmatrix} \mu_e^L \\ \mu_L \end{pmatrix}$	$\begin{pmatrix} \tau_e^L \\ \tau_L \end{pmatrix}$	$(1, 2, -\frac{1}{2})$
Right-handed leptons	e_R	μ_R	τ_R	$(1, 1, -1)$

Table 1.1: Representations of the SM fermions under $SU(3)_C \times SU(2)_L \times U(1)_Y$ gauge symmetry group. $SU(2)_L$ gauge transformations allow one to go between rows and $SU(3)_C$ transformations allow one to go between columns in these fermion representations. [REWORD]

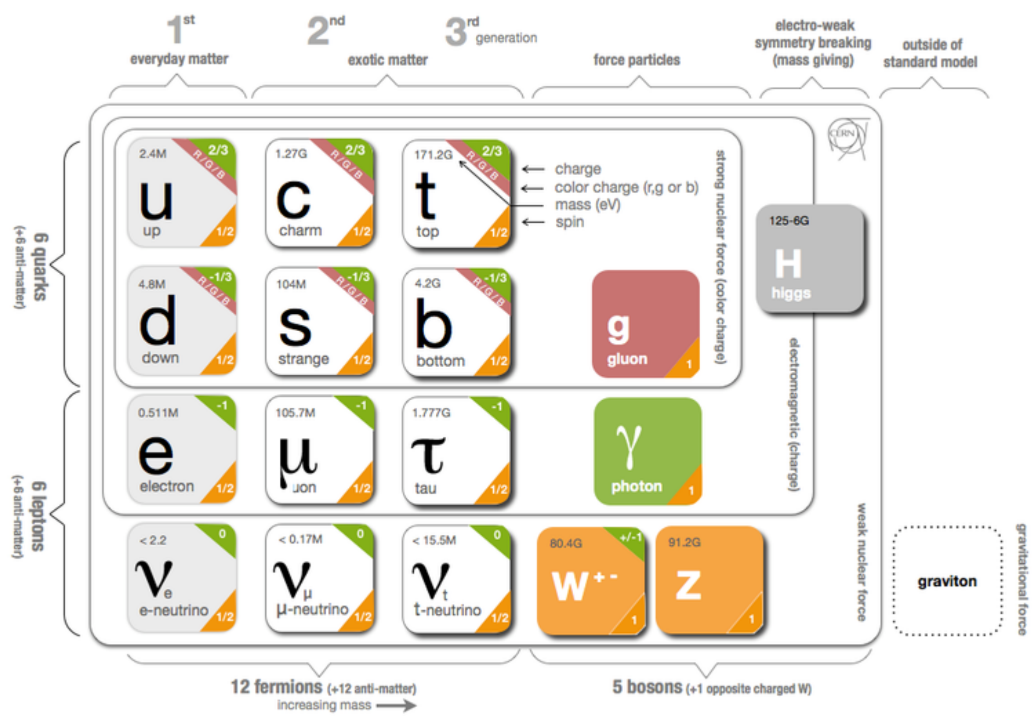

Figure 1.1: The particles of the Standard Model.

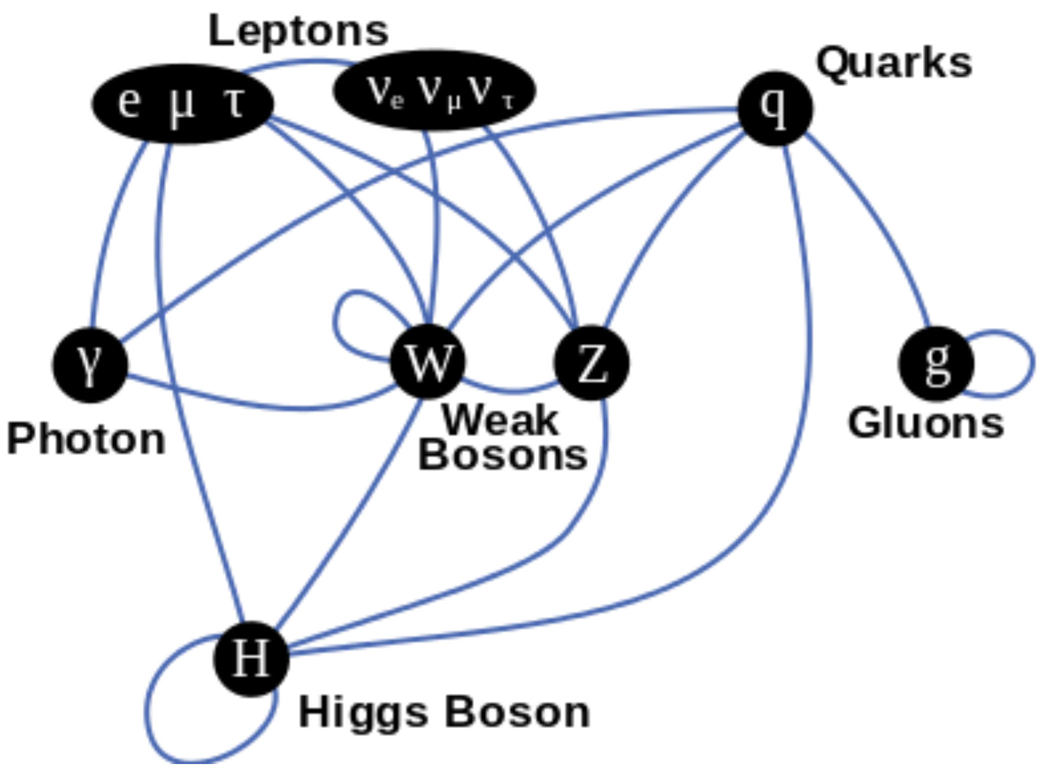

Figure 1.2: Summary of how Standard Model particles interact with other Standard Model particles.

Now we can understand the SM Lagrangian density as a Yang-Mills theory with the gauge group: $SU(3)_C \times SU(2)_L \times U(1)_Y$ with an additional SU(2) complex scalar Higgs field doublet that will be discussed later.

$$
\begin{aligned}
\mathcal{L}_{SM} = \; & \underbrace{-\frac{1}{4}B_{\mu\nu}B^{\mu\nu} - \frac{1}{4}W^a_{\mu\nu}W^{a\mu\nu} - \frac{1}{4}G^\alpha_{\mu\nu}G^{\alpha\mu\nu}}_{\text{Kinetic Energies and Self-Interactions of Gauge Bosons}} \\
+ \; & \underbrace{\bar{L}_i\gamma^\mu(i\partial_\mu - \frac{1}{2}g_1 Y_{iL}B_\mu - \frac{1}{2}g_2\sigma^a W^a_\mu)L_i}_{\text{Kinetic Energies and EW Interactions of Left-handed Fermions}} \\
+ \; & \underbrace{\bar{R}_i\gamma^\mu(i\partial_\mu - \frac{1}{2}g_1 Y_{iR}B_\mu)R_i}_{\text{Kinetic Energies and EW Interactions of Right-Handed Fermions}} \\
+ \; & \underbrace{\frac{ig_3}{2}\bar{Q}j\gamma^\mu\lambda^\alpha G^\alpha_\mu Q_j}_{\text{Strong Interactions between Quarks and Gluons}} \\
+ \; & \underbrace{\frac{1}{2}|(i\partial_\mu - \frac{1}{2}g_1 B_\mu - \frac{1}{2}g_2\sigma^a W^a_\mu)\Phi|^2 - V(\Phi)}_{\text{Electroweak Boson Masses and Higgs Couplings}} \\
- \; & (\underbrace{y^d_{kl}\bar{L}_k\Phi R_l + y^u_{kl}\bar{R}_k\widetilde{\Phi}L_l + h.c.)}_{\text{Fermion Mass terms and Higgs Couplings}}
\end{aligned}
$$

Here several abstract spaces are being spanned:

– a spans the three $SU(2)_L$ gauge fields with generators expanded in Pauli matrics, $T^\alpha = \frac{1}{2}\sigma^a$

– α spans the eight $SU(3)_C$ gauge fields, with generators expanded in Gell-Mann matrices, $\tau^\alpha = \frac{1}{2}\lambda^\alpha$

– L/R represent left and right projections of Dirac fermion fields. The Strong interaction is not chiral, so Q = L+R

– μ and ν are four-vector indices

– i, j, k are summed over the three generations of SM particles.

1.6 Higgs Mechanism

The SM Lagrangian without the addition of a Higgs field does not allow for gauge boson and fermion mass terms: $\frac{1}{2}m_A^2 A_\mu A_\mu$ and $m(\bar{\psi}\psi)$, as these terms are not gauge invariant. By introducing the Higgs field, mass terms for these particles may be included in a gauge invariant way. This field is a complex doublet with a potential $V(\Phi)$:

$$\Psi = \begin{pmatrix} \Phi^\dagger \\ \Phi^0 \end{pmatrix} \tag{1.24}$$

$$V(\Phi) = \mu^2 \Phi^\dagger \Phi + \lambda |\Phi^\dagger \Phi|^2 \tag{1.25}$$

The minima of this field occurs for $|\Phi| = \sqrt{\frac{\mu^2}{2\lambda}} \equiv \frac{v}{2}$. This yields degenerate minima, this symmetry is broken by choosing a specific minima (a.k.a. spontaneous symmetry breaking). By convention $\Phi_{min} = \frac{1}{\sqrt{2}} \begin{pmatrix} 0 \\ v \end{pmatrix}$ is chosen. This means the ground state of the Higgs field (Higgs vacuum) is non-zero, $\sqrt{\frac{-\mu^2}{\lambda}}$. The Higgs Field may now be expanded around this new ground state:

$$\Phi(x) = \frac{1}{\sqrt{2}} \begin{pmatrix} 0 \\ v + h(x) \end{pmatrix} \tag{1.26}$$

This non-zero Higgs vacuum now generates mass terms for the gauge bosons from the following term in the Lagrangian:

$$|(-\frac{1}{2}g_1 B_\mu - \frac{1}{2}g_2\sigma^a W_\mu^a)\Phi|^2 = \frac{1}{2}m_W^2 W_\mu^+ W^{-\mu} + \frac{1}{2}m_Z^2 Z_\mu Z^\mu \tag{1.27}$$

where:

$$W_\mu^\pm \equiv \frac{1}{\sqrt{2}}(W_\mu^1 \mp iW_\mu^2) \tag{1.28}$$

$$Z_\mu \equiv \frac{1}{\sqrt{g_1^2 + g_2^2}}(g_2 W_\mu^2 - g_1 B_\mu) \tag{1.29}$$

$$m_W = \frac{vg_2}{\sqrt{2}} \tag{1.30}$$

$$m_Z = \frac{v}{\sqrt{2}}\sqrt{g_1^2 + g_2^2} \tag{1.31}$$

The Higgs field also generates a mass term for the Higgs boson and self-interactions for the Higgs boson.

1.7 Electroweak Theory

$SU(2)_L$ generates $W^\pm, W^0$ gauge bosons, which would be massless if $SU(2)_L$ was a perfect symmetry. These bosons are massive as this symmetry is broken. The mass eigenstates, Z and γ given by:

$$\begin{pmatrix} Z_\mu \\ A_\mu \end{pmatrix} = \begin{pmatrix} cos\theta_W & -sin\theta_W \\ sin\theta_W & cos\theta_W \end{pmatrix} \begin{pmatrix} W_\mu^3 \\ B_\mu \end{pmatrix} \tag{1.32}$$

Here θ_W is the Weinberg angle given by:

$$cos\theta_W = \frac{g_2}{\sqrt{g_1^2 + g_2^2}} = \frac{m_W}{m_Z} \tag{1.33}$$

1.8 Quantum ChromoDynamics

As mentioned earlier the Strong Force, which binds the proton together, is mediated by gluons. Quantum Chromodynamics is the QFT which describes the interactions of quarks and gluons via $SU(3)_C$ symmetry. QCD contains features not present in Electroweak Interactions due to $SU(3)_C$ generators not commuting (a.k.a. $SU(3)_C$ is a non-abelian group). For example, in QCD there is color confinement and asymptotic freedom due to the structure constants being non-zero. Requiring $SU(3)_C$ local gauge invariance implies:

$$\psi(x) \to \psi(x)^{'} = exp[ig_S\alpha(x) \cdot \hat{T}]\psi(x) \tag{1.34}$$

where $\alpha(x)$ is the local phase function, g_S is the strong coupling constant, and $\hat{T}$ are the eight generators of $SU(3)$ (note $\hat{T^a} = \frac{1}{2}\lambda^a a$, where λ^a are the Gell-Mann matrices). As the Gell-Mann matrices are 3x3, this means ψ has three degrees of freedom under these $SU(3)$ rotations. So we represent ψ under $SU(3)$ rotations as:

$$\psi = \begin{pmatrix} \psi_{red} \\ \psi_{green} \\ \psi_{blue} \end{pmatrix} \tag{1.35}$$

Consequently, particle fields transforming under $SU(3)$ rotations have three components which physicists describe as color components (red, green, and blue). A particle's corresponding antiparticle has the corresponding anticolor. This color is the "charge" of QCD and is conserved under $SU(3)$ rotations. Combining colors, color neutral states (e.g. red and antired, or red, green and blue) may be created. For the Free Dirac Lagrangian to remain invariant under $SU(3)$ transformations, we must again postulate a boson field that modifies the derivative. The gluon field tensor is given by ($\alpha = 1, ..., 8$):

$$G^k_{\mu\nu} = \partial^\mu G^\nu_\alpha - \partial^\nu G^\mu_\alpha - g_S f^{\alpha\beta\gamma} G^\mu_\beta G^\nu_\gamma \tag{1.36}$$

Here $f^{\alpha\beta\gamma}$ are the structure constants of $SU(3)$. Combining all this gives the QCD Lagrangian:

$$\mathcal{L}_{QCD} = \bar{\psi}_{qi} i\gamma^\mu (D_\mu)_{ij} \psi^{qj} - m\bar{\psi}^{qi}\psi_{qi} - \frac{1}{4} G^\alpha_{\mu\nu} G^{\alpha\mu\nu} \tag{1.37}$$

Here i are the color indicies, and q are the quark flavors. It is important to note that quarks transform under the fundamental representation of $SU(3)$, while gluons transform under the adjoint representation. This means quarks carry a single color charge (red, green, blue, antired, antigreen, antiblue) and gluons carry a color and anticolor charge.

Figure 1.3 shows the three dominant QCD interactions. Sincle gluons carry color charge, they interact with one another.This does not occur in QED, as photons do not have electric charge and therefore do not interact with each other. In QED, a bare electron's effective charge is largest closest to the electron and decreases as a function of distance. This is because the QED vacuum fills with particle antiparticle pairs spontaneously, which screen the charge of the bare electron. The larger the distance from the electron, the smaller the effective charge and therefore the weaker the force. So for a pair of electrons, as the distance between them increases the repulsive force decreases and they may be observed separately.

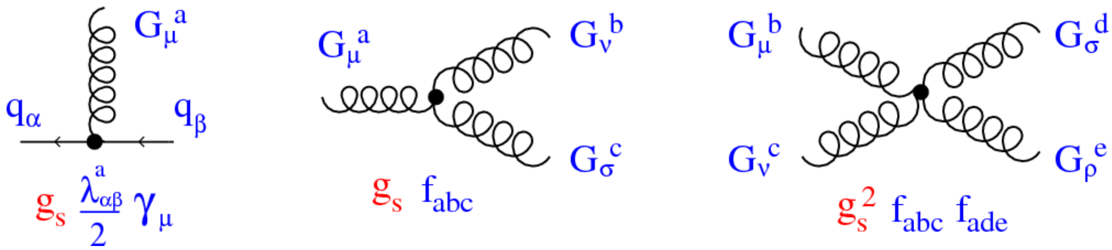

Figure 1.3: This figure shows the three dominant QCD interactions. From Ref. [14]

.

Bare quarks and gluons have not been observed. These particles have not been directly observed as they have not been found in isolation. Quarks and gluons group together to form color neutral objects, like baryons and mesons (qqq and $q\bar{q}$, respectively). This is because gluons have color charge and interact with each other. As the distance from a quark increases it's effective color charge increases due to the vacuum polarization in QCD. Color charge grows as the distance from the source increases (a.k.a. color is anti-screened in QCD). A quark's color charge increases with distance, so strong interactions become stronger at large distances (low momenta ineractions). At small distances (large momenta interactions) strong interactions are significantly weaker and considered nearly free. This effect of referred to as asymptotic freedom. At large distances, a quark's effective charge is large and the strong force is more significant. This force becomes so strong that quarks form colorless bound states instead of remaining free particles. This effect is known as color confinement. This running of all SM fields is shown in Figure 1.4.

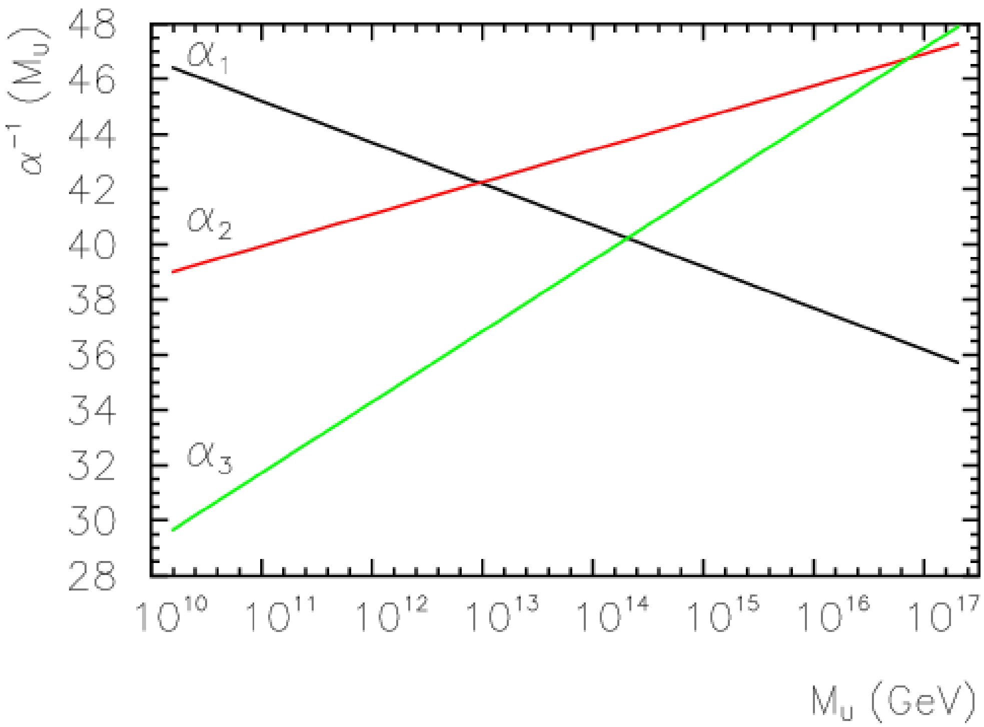

Figure 1.4: Strength of the U(1), SU(2), and SU(3) gauge couplings as a function of the energy scale of the interaction (Q). From Ref. [10]

Commonly the change in a particle's effective charge under a given force is quantified with $\beta(r) \equiv \frac{-de(r)}{d \ln r}$, where e(r) is the effective charge of a given particle under a force. In QED this function is positive but in QCD this function is negative leading to confinement and asymptotic freedom. Moreover, one can calculate how the coupling (α) of a force varies with energies. (More deeply this amounts to incorporating renormalization and vacuum polarization in the boson propagators). For QCD this is:

$$\alpha_S(x) = \frac{\alpha_S(\mu^2)}{1 + \beta_0 \alpha_S(\mu^2 ln(Q^2/\mu^2)} \tag{1.38}$$

$$\beta_0 = \frac{11N_c - 2n_f}{12\pi} \tag{1.39}$$

where Q is the momentum of the the force is probed at, μ^2 is the renormalization scale.

As stated previously, quarks and gluons have not been observed in isolation. Instead they form bound colorless states. Hadronization is the process by which quarks and gluons form hadrons. The process of hadronization is still an active area of research. One qualitative description is show in Figure BLAH. In this figure, as two quarks separate the color field between them is restricted to a tube with energy density of 1GeV/fm. As they separate further, the energy in the color field increases, until there is enough energy to produce $q\bar{q}$ pairs, which breaks the color field. This process repeats until quarks and antiquarks have low enough energy to form colorless hadrons. The resulting spray of hadrons is called a jet.

Since quarks and gluons carry different color charges, their respective jets have different properties. As quarks carry only a single color charge (vs. gluons which have color and anticolor charge), so their jets have less constituent particles. More precisely, the Altarelli-Parisi splitting functions [3] contain a factor C_A for gluon radiation off a gluon and C_F for gluon radiation off a quark ($C_A/C_F = 9/4$). These color factors are the prefactor in the Feynman diagrams for these processes [1], which leads to gluon jets having more constituents and therefore more tracks than quark jets. Gluon jets also tend to have a larger radius with lower momentum constituents than quarks. There are many novel techniques to distinguish quarks from gluons. For this study the number of charged particles will be focused on.

Chapter 2

Standard Model Successes and Limitations

The Standard Model has consistently described much of reality to an extreme degree of accuracy. It has predicted cross sections for strong and electroweak processes that span over ten order of magnitude correctly [see Fig 2.1] and contains no known logical inconsistencies. Despite the strength and reality of the Standard Model, it still fails to describe aspects of reality and suffers from aesthetic issues. To date, dark matter and energy comprise 95% of the universe, but are not accounted for in the SM. Additionally, neutrinos are known to have mass but are massless in the SM. There are mechanisms for introducing massive neutrinos in the SM, but these mechanisms create hierarchy problems.

Possibly the most significant aesthetic issue is the hierarchy between the electroweak and Planck scales. The electroweak scale is the scale of electroweak symmetry breaking. The Planck scale is the scale where the gravitational force is comparable in strength to the other forces. (This is also the scale where the gravitational potential energy of two objects separated by a distance r is equal to the energy of a photon with a wavelength r.) The Planck scale is where the SM breaks down, as there is not an experimentally verified theory of quantum gravity, and at this scale gravity cannot be ignored (like it can at the electro-weak scale). These scales differ by ~ 30 orders of magnitude. Understanding this difference in scales would not only explain the weakness of gravity at electroweak scales, but also hopefully lead to a QFT for gravity. (NB: This hierarchy can also be framed in terms of the corrections to the Higgs mass, which depend on the UV cutoff scale - where the SM is suppose to break, which is taken at the Planck scale. This leads the quantum corrections to the Higgs mass to force the Higgs mass to 10^{18} TeV.)

These stark contrasts in scales may indicate that a more fundamental theory exists. It is hoped that such a theory would explain and motivate some of the ad-hoc features of the SM. In particular, there currently are no experimentally verified explanations of why there are three generations of fermions, the values of the 19 SM parameters (6 quark masses, 3 charged lepton masses, 3 gauge couplings, Higgs parameters (μ^2, λ)), the structure of the fermion representations, etc.

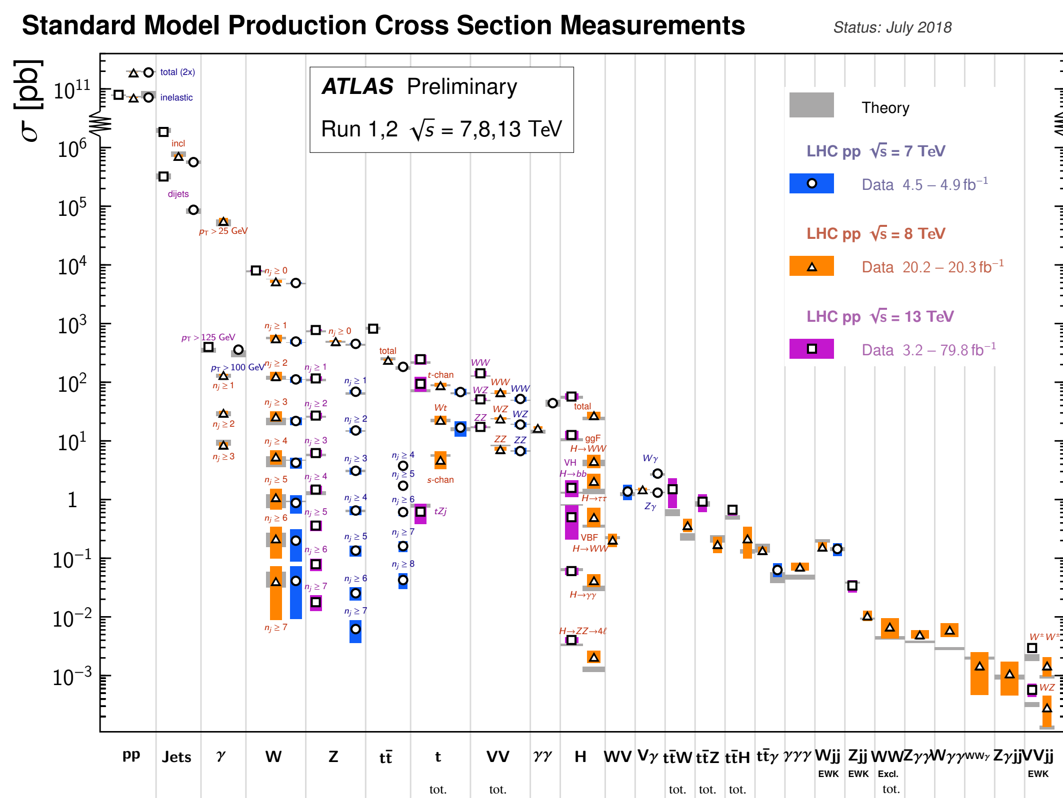

Figure 2.1: A comparison of cross section measurements at $\sqrt{s} = 7, 8, 13$ TeV from ATLAS compared to theoretical measurements. From Ref. [5]

.

Chapter 3

New Physics Models with Diboson Resonances

3.1 Randall Sundrum Bulk Model

The electroweak-planck hierarchy may be explained by the existence of extra dimensions, like the 5D Randall Sundrum Bulk Model ([15], [2]). In this model, there is one extra warped spatial dimension, y, with a metric:

$$ds^2 = e^{-2k|y|}\eta_{\mu\nu}dx^\mu dx^\nu + dy^2 \tag{3.1}$$

where $e^{-k|y|}$ is the warp factor of the extra dimension, which is compactified on a S^1/Z_2 orbifold (a.k.a. a circle where $y \rightarrow -y$). This can be visualized as every point in space time having a line extending from it a distance L, representing this fifth dimension. At the end of this line is the Planck brane. This fourth spatial dimension separates two 4-D branes: Planck brane and TeV brane. We live on the TeV brane, as shown in Figure 3.1. The Higgs field (and to a lesser degree the top quark and graviton fields) is localized near the TeV Brane, while the light fermion fields are localized more near the Planck brane. Fundamental parameters are set on the Planck brane. The warp factor may be scaled away from all dimensionless SM terms by field redefinitions. However, the only dimensionful parameter, $m_H^2 = v^2$ is rescaled by $\tilde{v} \sim e^{-kL} M_{Pl} \sim 1\text{TeV}$ for $kL \sim 35$, explaining why gravity is so weak on the TeV brane. Also, by localizing the light fermion fields near the Planck brane and top and graviton fields near the TeV brane, the light quarks will have smaller masses.

The two free parameters of this theory are M_{PL} and k. Based on this RS Bulk model, all SM particles should have Kaluza-Klein (KK) excitations. In particular, the graviton would have KK excitations that prefer to decay to WW or ZZ, which is why this analysis searches for RS Gravitons.

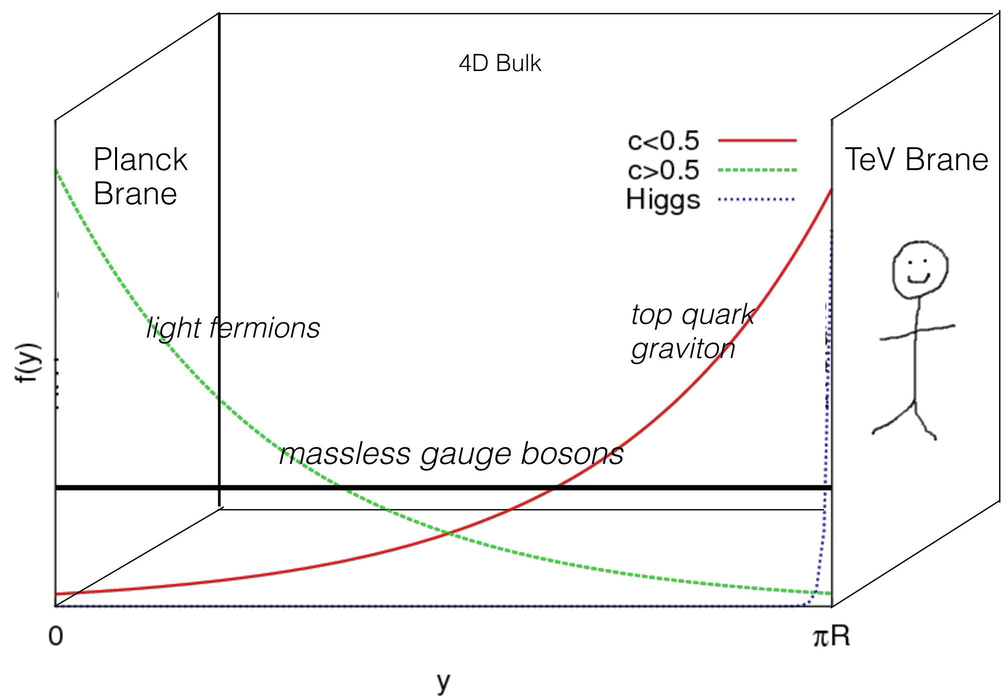

Figure 3.1: Cartoon of RS Bulk Model

.

3.2 Extended Scalar Sector

A further striking asymmetry of the SM is the simplicity of the scalar sector in comparison to the boson and fermion sectors. To date, the scalar sector has only one member, the Higgs boson. Therefore, it is natural to posit an extension to the scalar sector. From a theoretical standpoint this could also help generate baryon asymmetry through additional sources of CP violation. This analysis searches for a simple extension to the scalar sector as proposed in Ref. [16]. The extended scalar sector includes a real Higgs singlet (S) and complex $SU(2)_L$ doublet (Φ) (the SM Higgs), where mass eigenstates are mixtures of the fields. S has a vev of v and Φ has a vev of x. This then gives a Lagrangian of:

$$\mathcal{L} \supset (D^\mu\Phi)^\dagger D_\mu\Phi + \partial^\mu S\partial_\mu S - m^2\Phi^\dagger\Phi - \mu^2 S^2 + \lambda_1(\Phi^\dagger\Phi)^2 + \lambda_2 S^4 + \lambda_3\Phi^\dagger\Phi S^2 \quad (3.2)$$

The mass eigenstates of the scalar sector are then mixtures of S and Φ and the free parameters of the theory are m_H, $sin\alpha$, and $tan\beta = v/x$. The fields are then given by:

$$\Phi \equiv \begin{pmatrix} 0 \\ \frac{\tilde{h}+v}{\sqrt{2}} \end{pmatrix} \quad (3.3)$$

$$S \equiv \frac{h' + x}{\sqrt{2}} \quad (3.4)$$

Diagonalizing the mass matrix leads to the mass eigenstates h (discovered Higgs boson) and H (the physical particles):

$$\begin{pmatrix} h \\ H \end{pmatrix} = \begin{pmatrix} cos\alpha & -sin\alpha \\ sin\alpha & cos\alpha \end{pmatrix} \quad (3.5)$$

This suppressed h and H production and SM H couplings:

$$BR_{H\to SM} = sin^2\alpha \times \frac{\Gamma_{SM,H\to SM}}{\Gamma_{tot}} \tag{3.6}$$

Moreover, in the case that $m_H > m_h$, $H \to hh$ is possible. This further suppresses $H \to VV/ff$. This search is most sensitive to $H \to WW$.

3.3 Simple Standard Model Extensions

The RS Bulk model is motivated by resolving the hierarchy problem. Extending the Scalar sector is a natural space to look for new physics due to the complexity of fermion and boson groups. There are many other interesting and well motivated frameworks, but there is a lack of completely predictive models, due to model flexibility (free parameters). Therefore it is hard for experimentalists to know which theories to search for in data. However, as seen in 3[13], a "Simplified Model" approach may be taken. In the search for reasonably narrow width particles, as in this search, the search is not sensitive to all the details and free parameters of the theory. Generally such searches are only sensitive to the resonance mass and its interactions. Therefore, a theory's Lagrangian may be reduced to only retain this information (mass parameters and couplings). Experimental results using this framework may then be reinterpreted in a given theory.

In the simplified approach, a real vector field is represented under $SU(2)_L$ with vanishing hypercharge. This results in two charged and one neutral bosons. Defined as:

$$V^{\pm} = \frac{V_\mu^1 \mp iV_\mu^2}{\sqrt{2}} \tag{3.7}$$

$$V_\mu^0 = V_\mu^3 \tag{3.8}$$

The Lagrangian is then:

$$\mathcal{L} \supset -\frac{1}{4} D_{[\mu} V^a_{\nu]} D^{[\mu} V^{\mu]a} + \frac{m_V^2}{2} V^a_\mu V^{a\mu} + i g_V c_H V^a_\mu H^\dagger \tau^a \overleftrightarrow{D}^\mu H + \frac{g^2}{g_V} c_F V^a_\mu J^{\mu a}_F \tag{3.9}$$

In order the terms represent: the kinetic, V mass, Higgs-V interaction, and V-left-handed fermion interaction terms. Phenomenologically the three physical particles this predicts are degenerate, where V couples most strongly to VV, via the g_V coupling factor. The dominant production modes are DY and VBF.

Two versions of HVT are considered, Model A and B. Model A is a weakly coupled model where g_V 1, like the extended gauge symmetry discussed in Ref . [16]. Model B is a strongly coupled model, where $1 < g_V < 4\pi$. The width of the resonance grows with g_V so for this narrow resonance search only g_V is chosen to be less than 6 (so $\Gamma/M < 10\%$). More precisely, the coupling of these resonances to fermions scales as $g_f = g^2 c_F / g_V$, where g is the SM $SU(2)_L$ gauage coupling and c_F is the free parameter (expected to be of order 1 for Model A and B). This then means that for Model B the coupling is to fermions is more suppressed than for Model A, leading to a smaller DY production rate and BR to fermionic final states. The coupling of V to SM bosons scales as $g_H = g_V c_H$, where c_H is a free parameter on the order of 1 for Model A and B. So for small values of g_V (i.e. Model A - weakly coupled theories) the BR to gauge boson is smaller than for Model B. So weakly coupled vectors have large production cross sections and decay prominantly to leptons or jets, while strongly coupled vectors are produced less and decay predominantly to gauge bosons.

Vectors in Model A and B are generally produced via quark-anti-quark annihilation. The more rare production via vector-boson-fusion is considered by setting $g_H = 1$ and $g_F = 0$. In Model B diboson final states are enchanced as stated previously due to g_H and moreover the BR to WZ, WH, WW, and ZH are the same.

In summary, V couples most strongly to left-handed fermions and VV dependent on g_V.

Part II

Experimental Setup

Chapter 4

LHC

The Large Hadron Collider (LHC) is the highest-energy particle collider in the world. It was designed to expand the frontier of high energy particle collisions in energy and luminosity. This enables LHC experiments to test the Standard Model and search for new physics at higher energies than tested with previous colliders. Collisions at higher energies not only produce more massive particles but also more weakly interacting particles. Fig 4.1 shows production cross sections for various processes at hadron colliders. The rate for electroweak physics prcoesses including W and Z scale with the center-of-momentum energy, $\sqrt{s}$.

The LHC consists of a 26.7 km (17 miles) ring, approximately 100 m underground, outside Geneva, Switzerland. Counter-circulating proton (and occasionally heavy ions) beams collide inside four experiments along the beam line: ATLAS, CMS, LHCb, ALICE. ATLAS and CMS are general purpose detectors designed to explore high energy frontier. LHCb is designed to study the physics of b-quarks. ALICE specializes in studying heavy ion collisions.

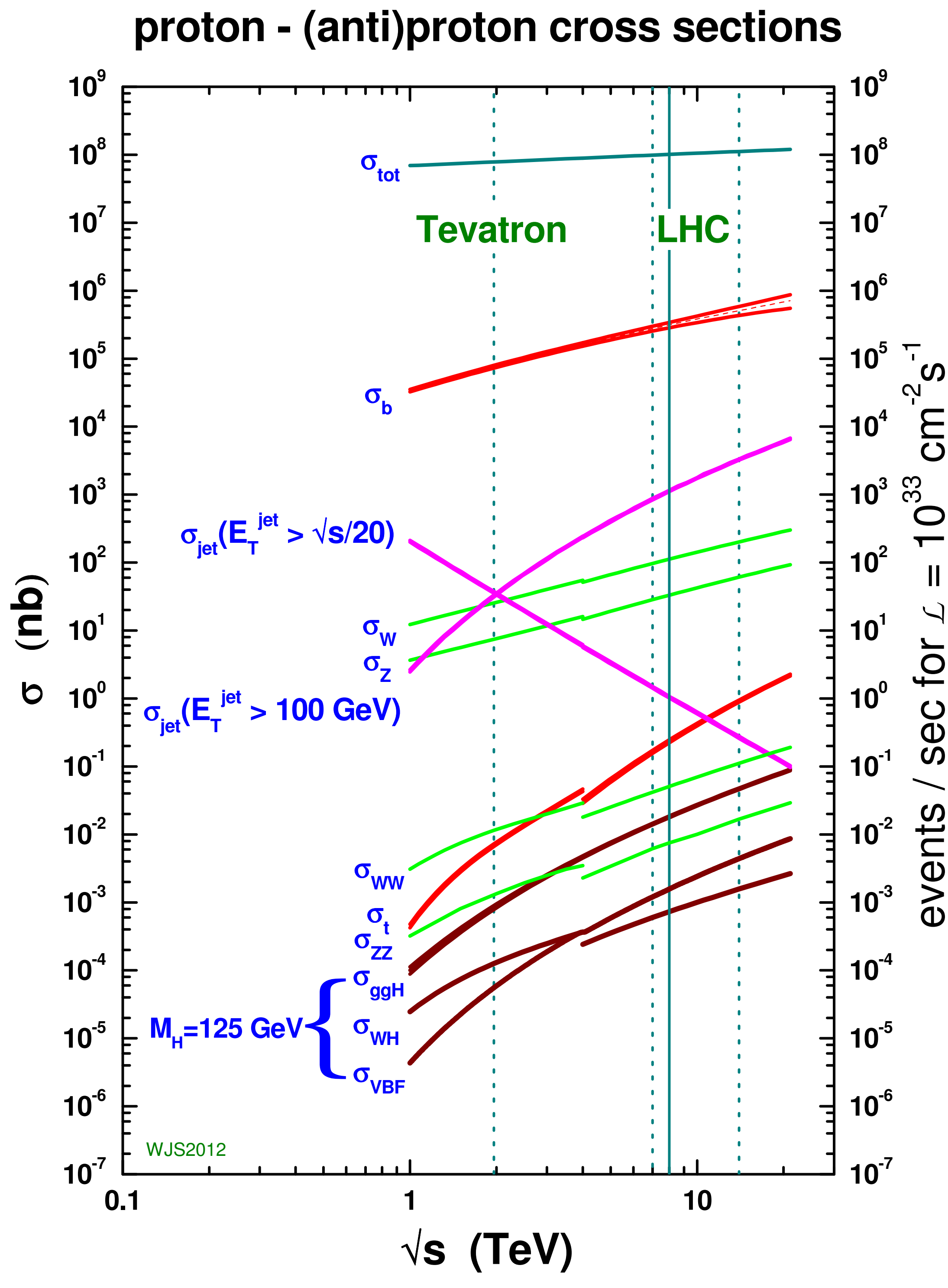

Figure 4.1: Scaling of cross sections with $\sqrt{s}$. Natasha: write more here

.

The first proton beams circulated in September, 2008. Nine days later an electrical fault lead to mechanical damage and liquid helium leaks in the collider. This incident delayed further operation until November 2009, when the LHC became the world's highest energy particle collider, at 1.18TeV per beam. This first operational run continued until 2013, reaching 7 and 8 TeV collision energies. During this run a particle who's properties were consistent with the Standard Model Higgs boson was discovered. The next operational began after a two year shutdown after upgrades to the LHC and experiments. This run lasted from 2013 to 2018 reaching 13 TeV collision energies. This analysis uses data from the second operational run.

4.1 LHC Layout and Design

The layout of the LHC is shown in Figure 4.2. The red and blue lines in the figure represent the counter-circulating proton beams. The LHC is divided into eight octants. Octant 4 contains the RF cavities that accelerate the protons and octant 6 contains the beam dump system. Octants 3 and 7 house the collimation systems for beam cleaning. The beams collide inside the four aforementioned experiments. Each octant contains a curved and straight section. The LHC magnets are built with NBTi superconductors cooled with super-fluid Helium to 2K, creating a 8.3T magnetic field to bend the proton beams.

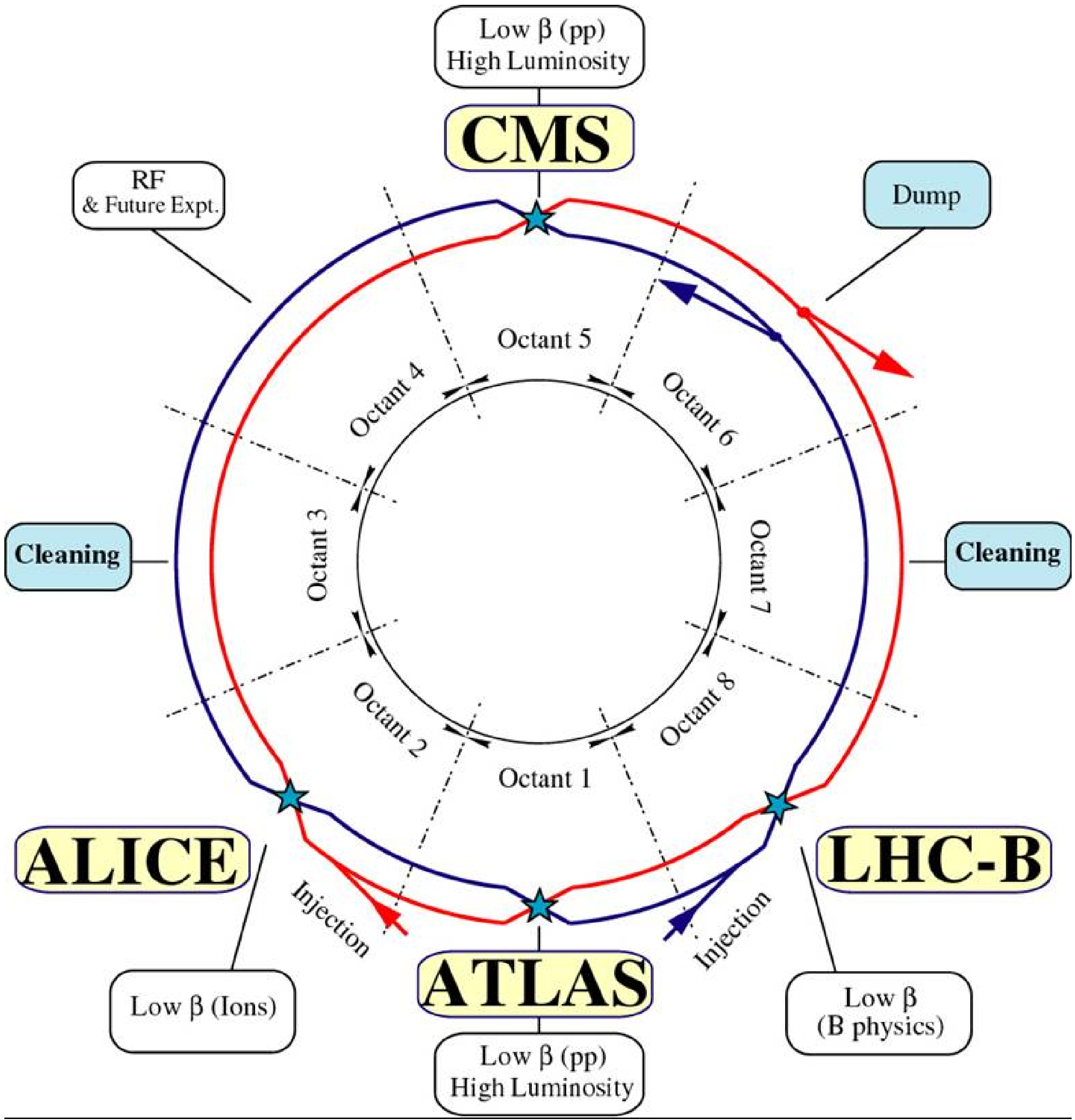

Figure 4.2: LHC Layout. Natasha write more
.

Four sequential particle accelerators are used to accelerate proton from rest as shown in Figure 4.3. First, Hydrogen gas is ionized to produce protons which are then accelerated to 50 MeV using Linac 2, a linear accelerator. The resulting proton beam is then passed to three circular particle accelerators: Proton Synchrotron Booster, Proton Synchrotron, and Super Proton Synchrotron (SPS), accelerating protons to 1.4, 25, and 450 GeV, respectively. Once the protons exit SPS, the are injected into the LHC at octant 2 and 8. Each proton bunch contains 10^{11} protons. The spacing between bunches is 25 ns, which means each beam contains 3564 bunches. However, some bunches are left empty due to injection and safety requirements, yield 2808 bunches per beam. Once the proton beams are injected they are accelerated to 13 TeV.

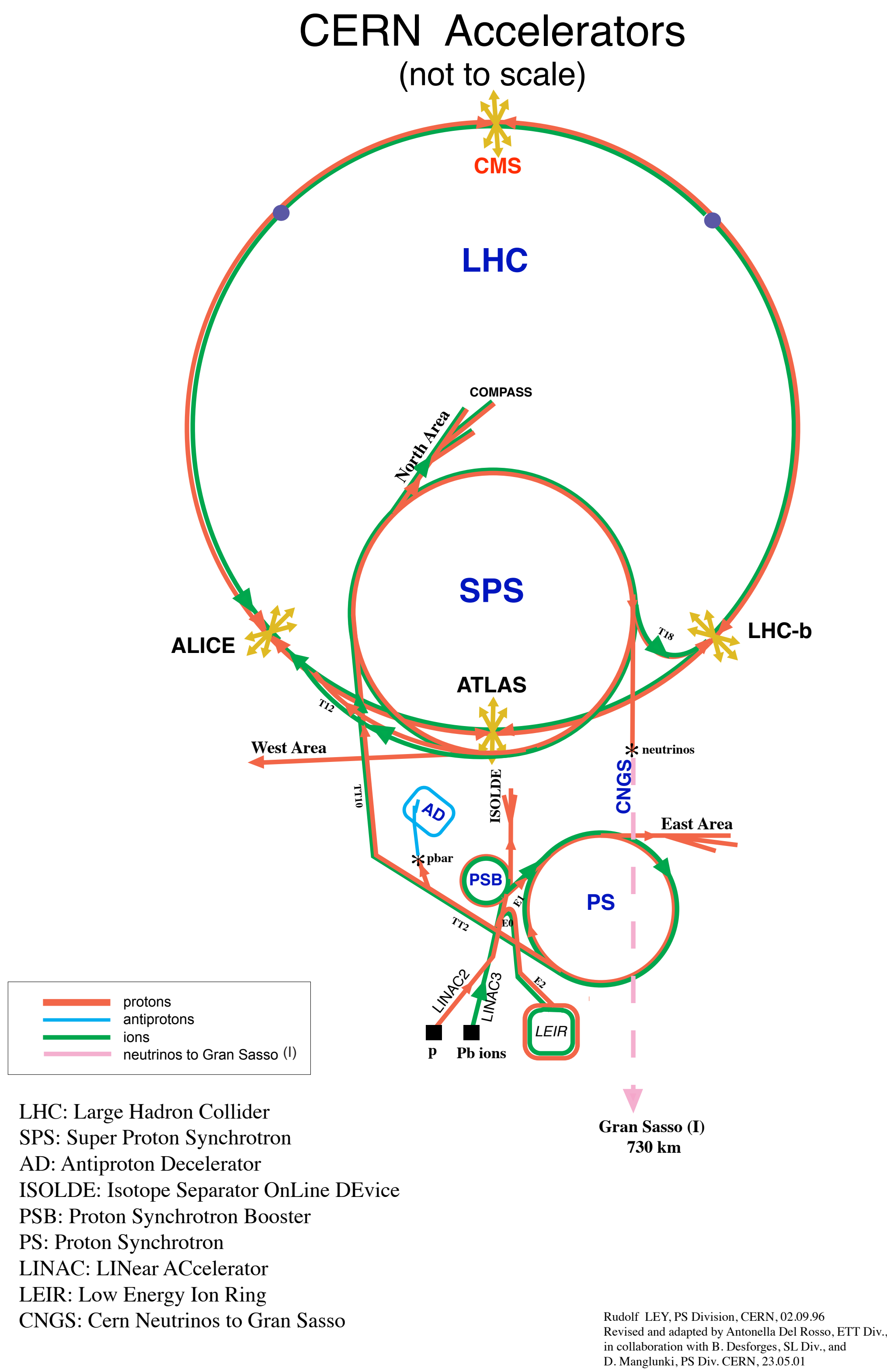

Figure 4.3: LHC Accelerator. Natasha write more

.

As many new physics models predict cross-sections below the weak scale it was important to design the LHC to be capable of collecting enough data, by running in high luminosity conditions. The machine luminosity depends only on beam parameters:

$$L = \frac{N_p^2 f}{4\epsilon\beta^*} F \tag{4.1}$$

where N_p is the number of protons per bunch, f is the bunch crossing frequency, ϵ is the transverse beam emittance, β^* is the amplitude function at the collision point, and F is the geometric luminosity reduction factor due to the beams crossing at an angle (rather than head-on).

This analysis uses data from Run 2, totally 139/fb. The peak luminosity was [Natasha add info here]. [Natasha add lumi and integrated lumi figures].

Chapter 5

The ATLAS Detector

The ATLAS detector measures the position, momentum and energy of particles produced in the proton collisions by using magnetic fields, silicon detectors, sampling calorimeters, and gaseous wire detectors. It is located approximately 100 m underground at Point-1 around the LHC beam line and weighs 7000 metric tons. The detector is 46 m long, 25 m high, 25 m wide as shown in Figure 5.2. The detector can be divided into three subsystems: the Inner Detector (ID), the Calorimeters, and the Muon Spectrometer (MS). Figure 5.3 shows an overview of how different particles interact in the detector.

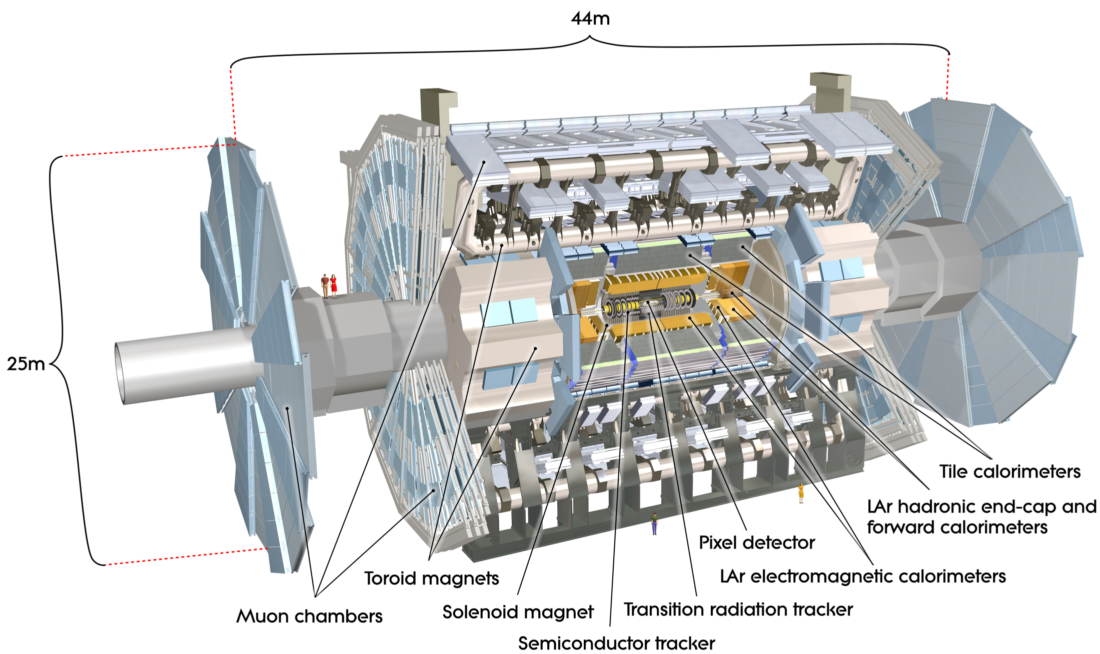

Figure 5.1: Big picture layout of ATLAS detector. Natasha: write more

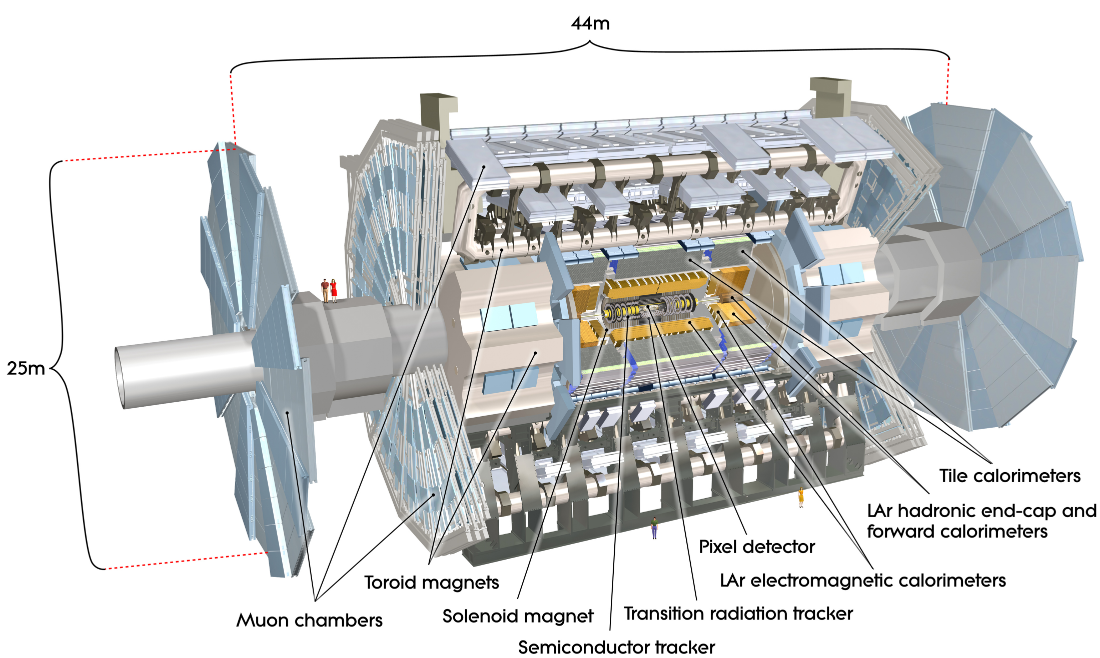

Figure 5.2: Big picture layout of ATLAS detector. Natasha: write more

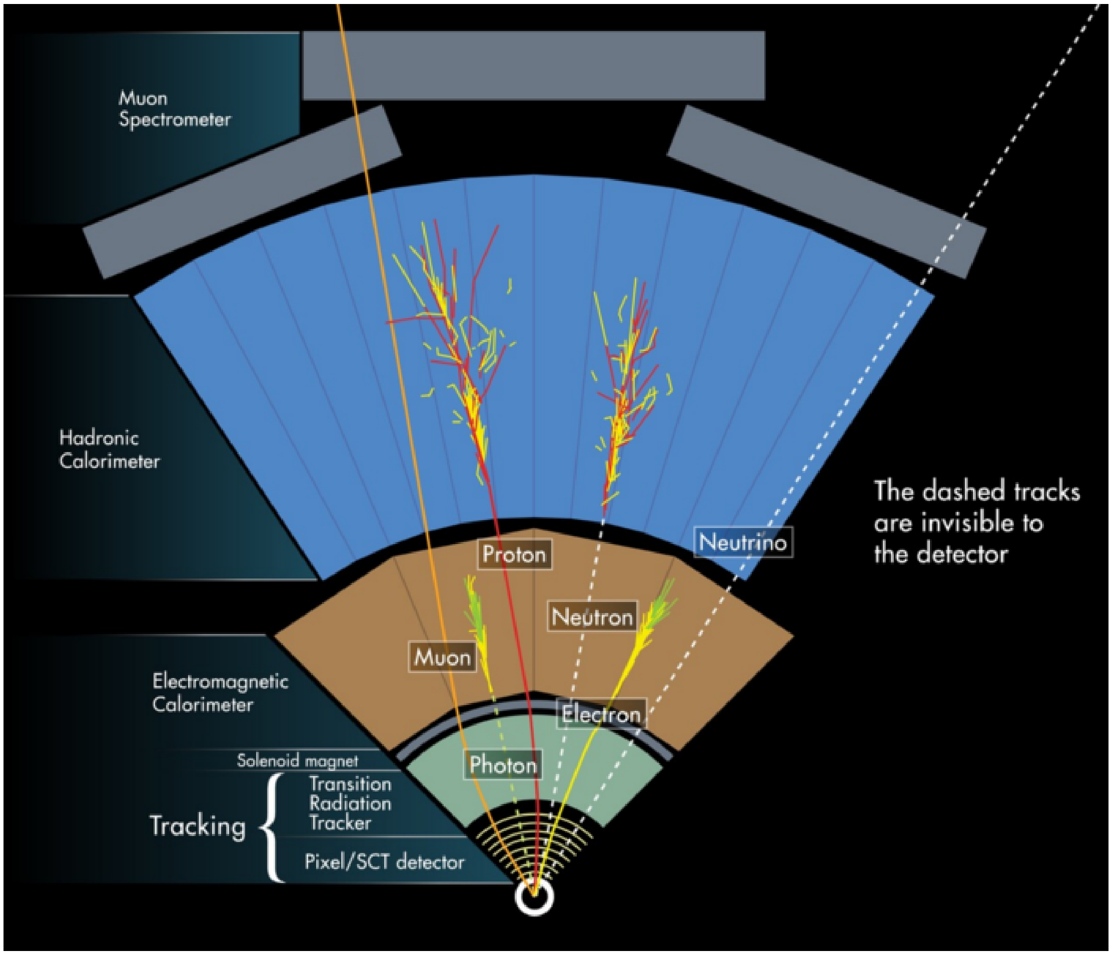

Figure 5.3: A simplified schematic of how different particles interact and are detected within ATLAS.

5.1 Coordinate System

The trajectory of particles within ATLAS is measured relative to the nominal interaction point. The z-axis points along the beam line, such that when the LHC is viewed from above, the counter-clockwise circulating beam points along the positive-z direction. The $x - y$ plane is transverse to the beam line, with the positive x-axis pointing towards the center of the LHC ring. The positive y-axis points vertically upward. The azimuthal angle, ϕ, is the angular distance about the z-axis, with $\phi = 0$ along the x-axis. The polar angle from the z-axis is denoted as θ. The polar angle is usually replaced by pseudo-rapidity, $\eta = -ln tan(\frac{\theta}{2})$. Pseudo-rapidity is preferred as $\Delta\eta$ is invariant under boosts along z and particle production is approximately invariant under η. Angular separation between particles in ATLAS are given by $\Delta R = \sqrt{\Delta\eta^2 + \Delta\phi^2}$. The distance from the beamline is given by $r = \sqrt{x^2 + y2}$

5.2 Inner Detector

The Inner Detector (ID) was designed to identify and reconstruct vertices, distinguish pions from electrons, and measure the momentum of charged particles. The ID uses three different technologies for particle reconstruction: the Pixel Detector, Semiconductor Tracker (SCT), and the Transition Radiation Tracker (TRT), shown in Figure 5.4 and 5.5. The entire ID is immersed in a 2T solendal magnetic field paralel to z, causing charged particles to bend in the transverse-plane, allowing particle momentum measurements.

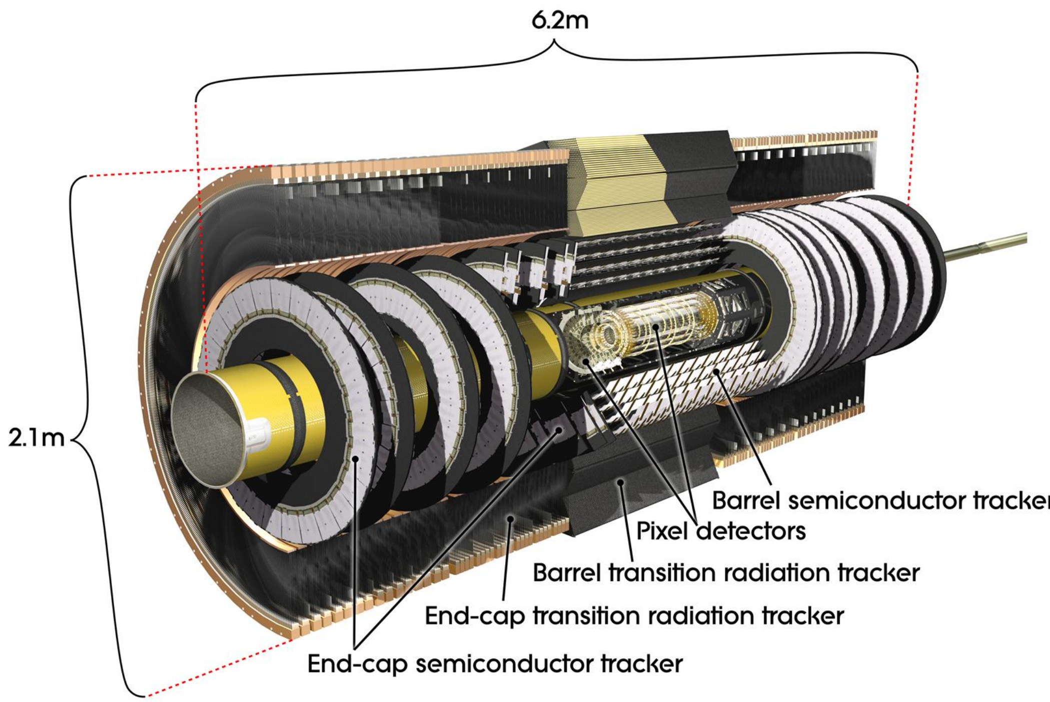

Figure 5.4: Layout of ATLAS Inner Detector

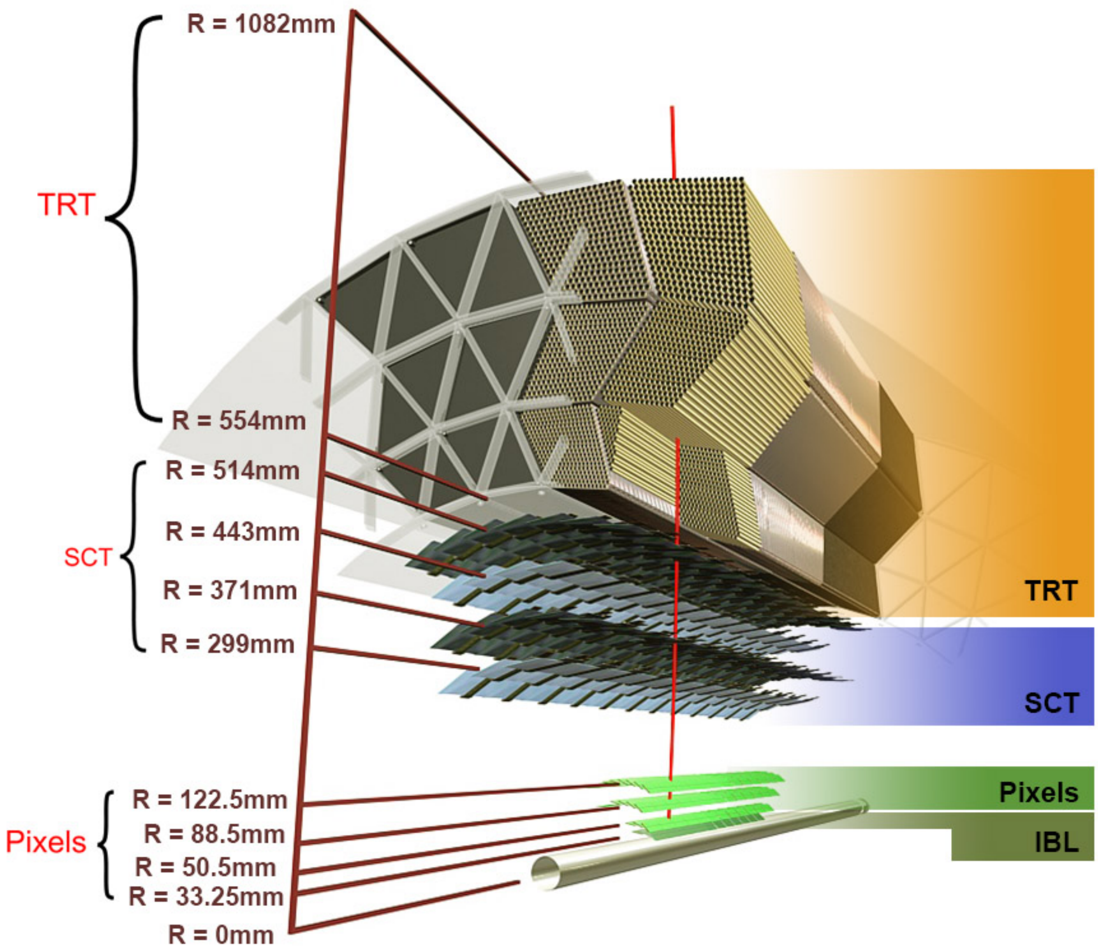

Figure 5.5: Layout of ATLAS ID Barrel System.

5.2.1 Pixel Detector

The pixel detector consists of four barrel layers between r = 32.7 and 122.5 mm, extending to $|z| = 400.5$mm. The innermost pixel barrel, the Insertable b-Layer (IBL), only extends to $|z| = 332$ mm. The pixel detectors closer to the beam line (larger η values) consists of six parallel cylindrical rings of pixel detectors transverse to the beam line. The entire pixel detector consists of 1744 identical pixel sensors each with 46080 readout channels, totaling about 80 million individual pixels. Most of the pixel sensors are $50 \times 400 \mu m^2$. The intrinsic measurement accuracy of a individual pixel detector in the barrel (end-cap) in $r - \phi$ is 10 μm and 115 μm in $z(r)$.

5.2.2 Semiconductor Tracker

The SCT is located outside the pixel detector and has the same barrel and endcap geometry as the pixel detector. SCT sensors are 80μm $\times$ 12 cm (80μm strip pitch). In the barrel the strips are parallel to the z-axis and are segmented in ϕ. In the endcaps, the strips extend radially. Sensors are grouped in modules containing two layers of strips rotated 40 mrad with respect to each other. This offset allows for the two-dimensional position of a track to be determined by identifying the crossing point of the strips that registered a hit. SCT modules measure tracks with an accuracy of 17 μm in $r - \phi$ and 580μm in $z(r)$ in the barrel (end-cap) region.

5.2.3 Transition Radiation Tracker

The transition radiation tracker (TRT), enveloping the SCT, is a gaseous straw-tube tracker mainly used for electron/pion track separation. Each straw is 4 mm in diameter and filled with a Xe-CO_2-O_2 gas mixture. An anode wire at the center of the straw is held a ground potential, while the walls of the straw are kept at -1.4kV. When a charged particle passing through the TRT ionizing the gaseous mixture, and the resulting ions form an avalanche on the anode wire with a grain of 10^4. The resulting signal from the anode wire is then digitized and amplified. Signals passing a low threshold cutoff are used to distinguish noise from tracks. Signals passing a high threshold cutoff are sensitive to transition radiation (TR). TR photons are emitted when charged particles pass between materials with different dielectric constants. The probability that a charged particle with energy E and mass m passing between two materials emits a TR photon in the keV range is proportional to $\gamma = E/m$. In the TRT staws these often then convert via the photoelectric effect, causing a large avalanche triggering the high-threshold. Since electrons have a smaller mass than pions, tracks from electrons are more likely to trigger the high threshold. Consequently, the high threshold TRT trigger provides electron identification information that is uncorrelated with calorimeter shower-shape information.

The barrel region of the TRT extends from r =563-1066 mm and $|z| < 712$ mm. Barrel Straws are 144 cm long (divided $\eta \approx 0$) and orientated parallel to the beam direction. End-cap straws extend radially and are 37 cm long. There are 53,544 straws in the barrel and 160,000 straws in the end-caps. Radiator mats of polypropylene/polyethylene fibers in the barrel are aligned perpendicular to the barrel straws (with holes for the straws to pass through). In the end-cap region, radiator foils are layered between the radial TRT straws.

The width of the signal pulse is sensitive to the distance between the charged particle track and the anode wire and allows for a hit resolution of 130μm. The TRT extends to $|\eta| = 2.0$ and provides about 36 hits per track.

5.3 Calorimeters

The ATLAS electromagnetic and hadronic calorimeters (EMC and HCAL, respectively) absorb and measure the energy of high energy hadrons, photons, and electrons with $|\eta| < 4.9$. Both systems use sampling calorimeters which consist of alternating layers of dense absorbing and active layers. In the absorbing layer particles interact and lose energy, creating showers. These showers are then detected and measured in the active layer. The amount of charge measured in the active material scales with the energy of the incident particle, and thus provides a measurement of the particle's energy. An overview of the layout of the calorimeter system is shown in Figure 5.6.

The EMC measures and contains the energy of electromagnetically interacting particles with 170k channels. It consists of layered accordion-shaped Lead absorber plates and electrodes immersed in liquid Argon. Using accordion-shaped electrode and absorbers ensures ϕ symmetry and coverage. The EMC is composed of a barrel part ($|\eta| < 1.475$), two end-caps ($1.375 < |\eta| < 3.2$), and a presampler ($|\eta| < 1.8$). The presampler, containing only liquid Argon, corrects for upstream energy losses of electrons and photons. The EMC barrel is segmented into three layers. The first layer has finest segmentation with readout cells extending $\Delta\eta \times \Delta\phi = 0.025/8 \times 0.1$. This provides a precise shower measurements used to separate prompt photons from $\pi^0 \rightarrow \gamma\gamma$ decays. The second layer has coarser segmentation and is approximately 16 radiation lengths long. A radiation length is the average distance an electron travels before losing all but $1/e$ of its energy to bremsstrahlung. The last layer is the most coarse and measures the tail of the electromagnetic shower. A schematic of the ECAL is shown in Figure **??**.

The hadronic calorimeter located outside the EMC and is used to contain and measure the energy of hadronically interacting particles. It consists of a tile calorimeter (TileCal), hadronic end-cap calorimeter (HEC), and liquid Argon forward calorimeter (FCAL). TileCal is located behind the LAr EMC and uses steel absorbers and liquid Argon as the active material. TileCal consists of three barrel layers in the central and forward regions, extending up to $|\eta| < 1.7$. Radiated photons from the steel tiles are collected via wavelength-shifting fibers connected to photomultiplier tubes, as shown in Figure 5.8. The HEC lies behind the EMC endcap wheels. It uses copper absorbers and liquid Argon as the active material and covers $1.5 < |\eta| < 3.2$. Finally, the FCAL covers $3.1 < |\eta| < 4.9$ and consists of three modules all using liquid Argon as the active material. The first module uses copper absorber and was designed for electromagnetic measurements. The second and third modules consist of tungsten absorber and are used to measure the kinematics of hadronically interacting particles. A schematic of the HCAL is shown in Figure 5.8.

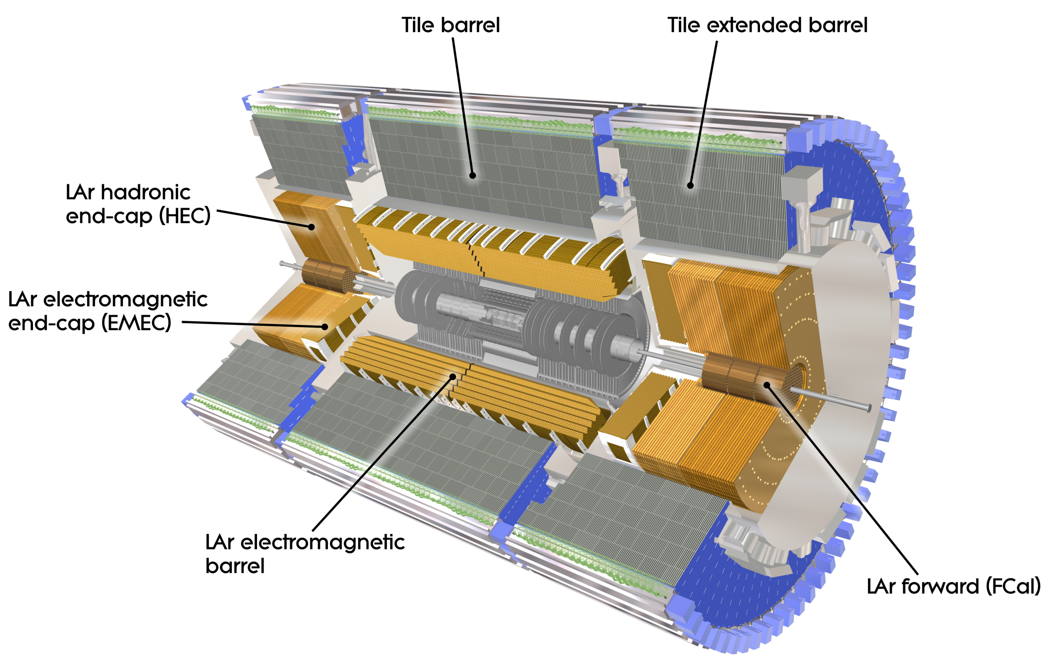

Figure 5.6: Overview of ATLAS electromagnetic and hadronic calorimeters.

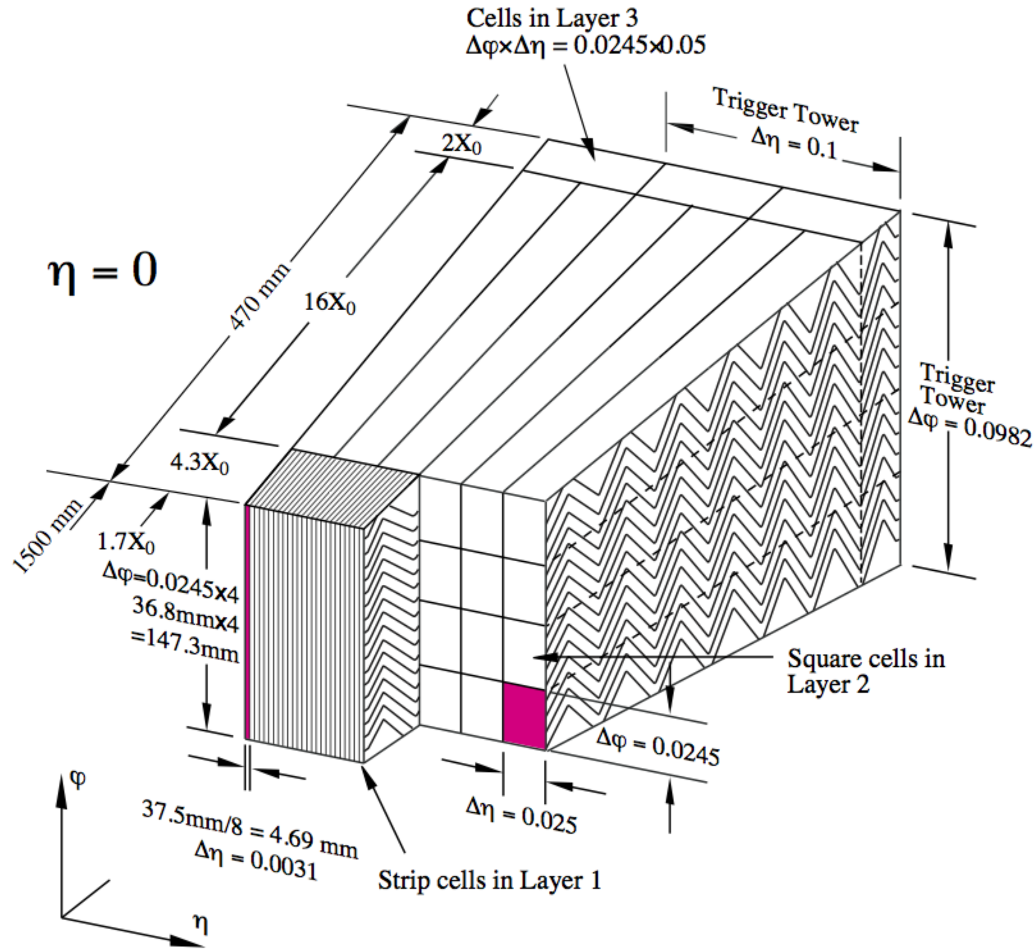

Figure 5.7: Schematic of ECAL.

Figure 5.8: Schematic of HCAL.

The energy resolution of the calorimeter subsystems are:

$\frac{\sigma_E}{E} = \frac{10\%}{\sqrt{E}} \bigoplus 0.7\%$ EMC

$\frac{\sigma_E}{E} = \frac{50\%}{\sqrt{E}} \bigoplus 3\%$ hadronic barrel –Natasha check if barrel and end-cap truly have same energy resolution

$\frac{\sigma_E}{E} = \frac{50\%}{\sqrt{E}} \bigoplus 3\%$ hadronic end-cap

$\frac{\sigma_E}{E} = \frac{100\%}{\sqrt{E}} \bigoplus 10\%$ hadronic end-cap

5.4 Muon Spectrometer

The muon spectrometer (MS) is the outermost detector system in ATLAS. Muons with a $p_T > 4$ GeV are energetic enough to reach the MS. To measure the momentum of these muons to barrel and end-cap toroid magnets are used covering $|\eta| < 1.4$ and $1.6 < |\eta| < 2.7$. For $1.4 < |\eta| < 1.6$, a combination of the barrel and end-cap toroidal magnetic fields bend muon trajectories. The detector in the barrel region form three concentric rings at $R = 5, 7.5, 10$m and are segmented in ϕ to accommodate the magnets. The end-cap region consists of three circular planes perpedicular to z and located at $|z| = 7.4, 14, 21.5$m from the interaction region. An additional detector at $|z| = 10.8$m covers the transition region between the barrel and end-cap.

The MS consists of four subsystems: Monitored Drift Tubes (MDT), Cathode Strip Chambers (CSC), Resistive Plate Chambers (RPC), and Thin Gap Chambers (TGC). The first two subsystems are used primarily for measuring muon track parameters, while the RPC and TGC subsystems are used for muon triggering. A schematic of this system is shown in Figure 5.9.

The MDT subsystem consists of precision tracking chambers for $|\eta| < 2.7$, except for the inner most end-cap layer ($2.0 < |\eta| < 2.7$), where CSCs are used. The basic unit of MDT chambers are thin walled Aluminum tubes with a diameter of 3 cm and length of 0.9-6.2 m. These tubes are filled with a mixture of Ar-CO_2 gas with a 50μm W-Rn wires running down the center of the tube which is kept at 3080 V. Since the maximum drift time of these chambers is 700 ns, they are not used for triggering. MDT chambers consist of 3-4 layers of tubes mounted on a rectangular support system, as seen in Figure 5.10, orientated along ϕ to measure the coordinate in the bending plane of the magnetic field with a resolution of 35 μm.

The MDT subsystem can only handle hit rate below 150Hz/cm^2. For this reason, CSCs are used in the innermost end-cap layer where hit rates are larger. CSCs can handle hit rates up to 1000Hz/cm^2. CSC are multiwire proportional chambers. These chambers are filled with a Ar-CO_2 gas mixture and evenly spaced wires kept at 1900 V. These wires are orientated in the radial direction but not read out. Instead on one side of the cathode are copper strips parallel to the wires, measuring η, while on the other side of the cathode are strips parallel to the wires measuring ϕ. The width between strips is approximately 1.5 mm providing a resolution of 60 μm in the bending-plane and 5 mm in the non-bending plane.

Since the CSC and MDT systems do not poor time resolution, the RPC and TGC systems are used for triggering. The RPC system is used in the barrel region ($|\eta| < 1.05$). RPC consist of two parallel resistive plates separated by a 2 mm insulated spacer with 100 mm spacing kept at 9.8 kV 5.11. A gaseous mixture of $C_2H_2F_4$, C_4H_{10}, and SF_6 fills the space between the two plates. Metallic strips on the outer faces of the plates are used to read out signals produced by the gas ionizing. The middle barrel layer consists of two layers of RPCs on either side of the MDT layer and one layer on the outermost MDT layer. Each layer contains two orthogonal sets of metallic strips providing η and ϕ measurements. The timing resolution of RPCs is 1.5 ns, and therefore may be used to identify bunch crossings.

Finally, the TGCs are used in the end-cap regions and primarily used to provide L1 trigger decisions and ϕ measurements. TGCs are multi-wire proportional chambers consisting of arrays of gold-coated tungsten wires placed between two cathode planes. These wires are separated by 1.8 mm and cathodes are 1.4 mm from the wires. Orthogonal to the wires, on the opposite side of the cathode plane are copper strips held at 2900 V. The chambers are filled with a mixture of CO_2

and n-pentane gas, the latter acts as a quenching gase to prevent avalances initiated by secondary γ-rays from the primary avalanche. Figure 5.12 is a schematic of a TGC. The timing resolution of TGCs is less than 25 ns and therefore are used for bunch crossing measurements.

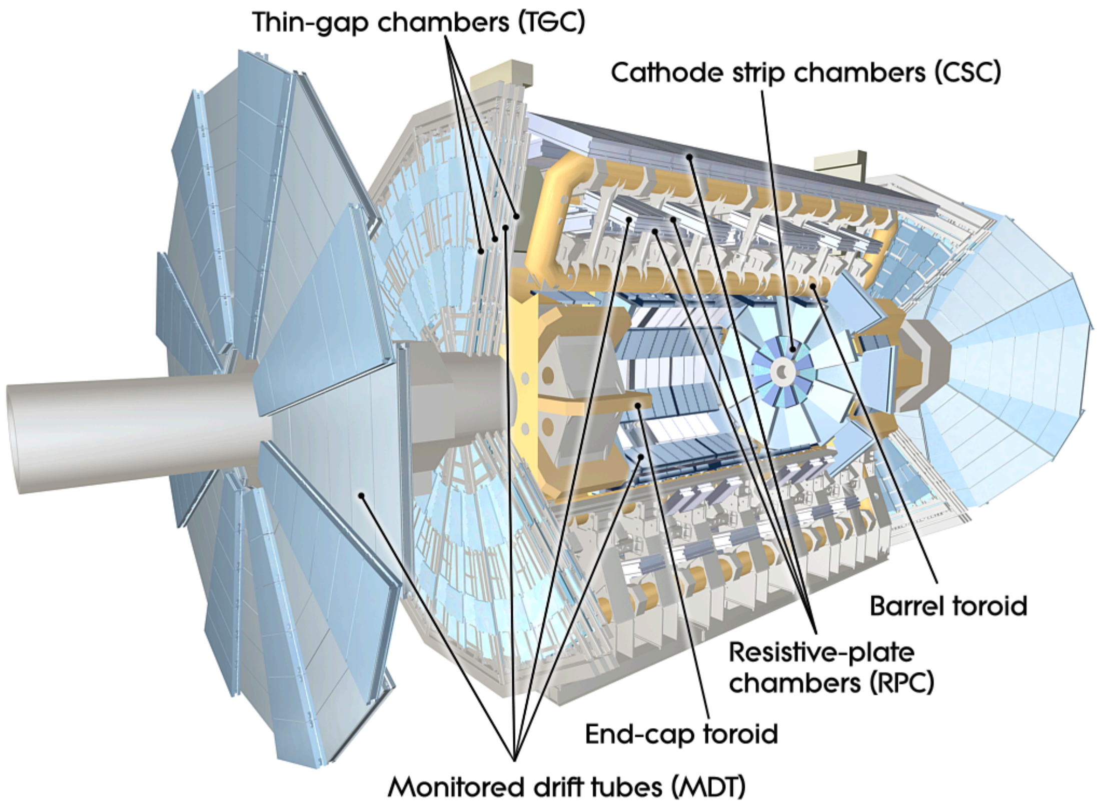

Figure 5.9: Schematic of Muon Spectrometer [cite G35]

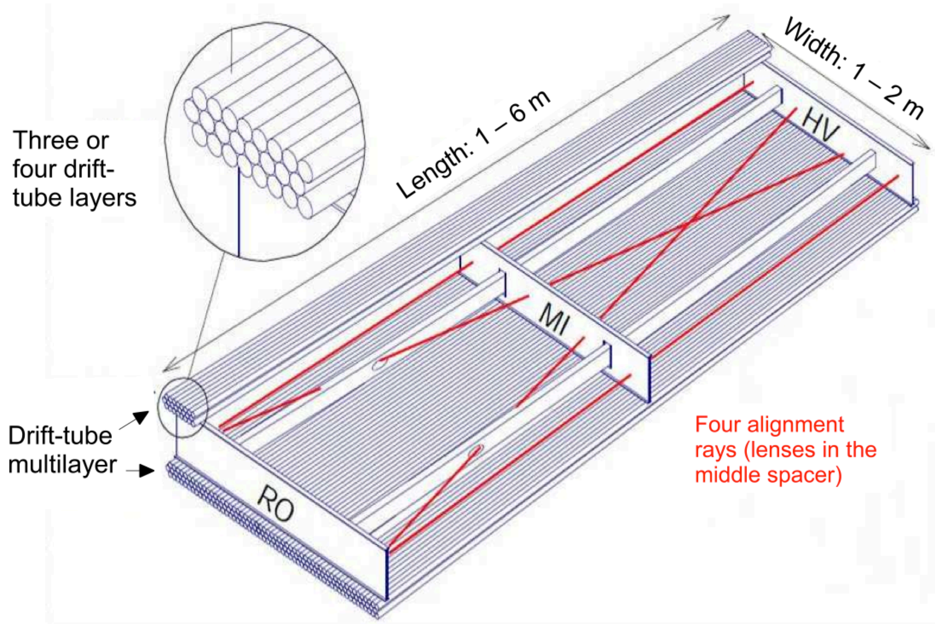

Figure 5.10: Schematic of MDT chamber. [cite G35]

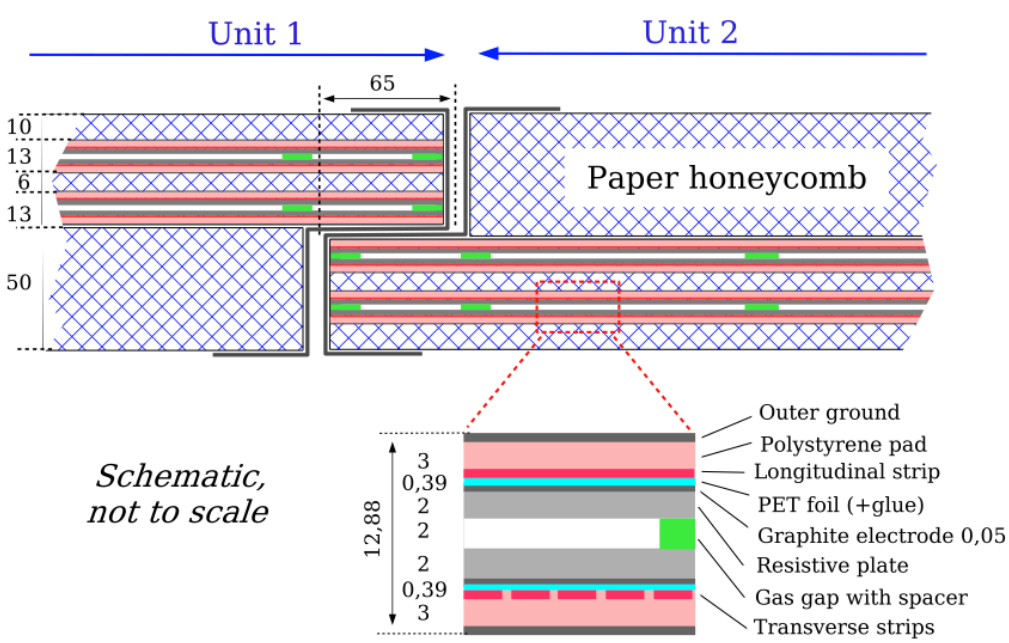

Figure 5.11: Schematic of RPC chamber, which is used for triggering in the central region of the detector [cite G35].

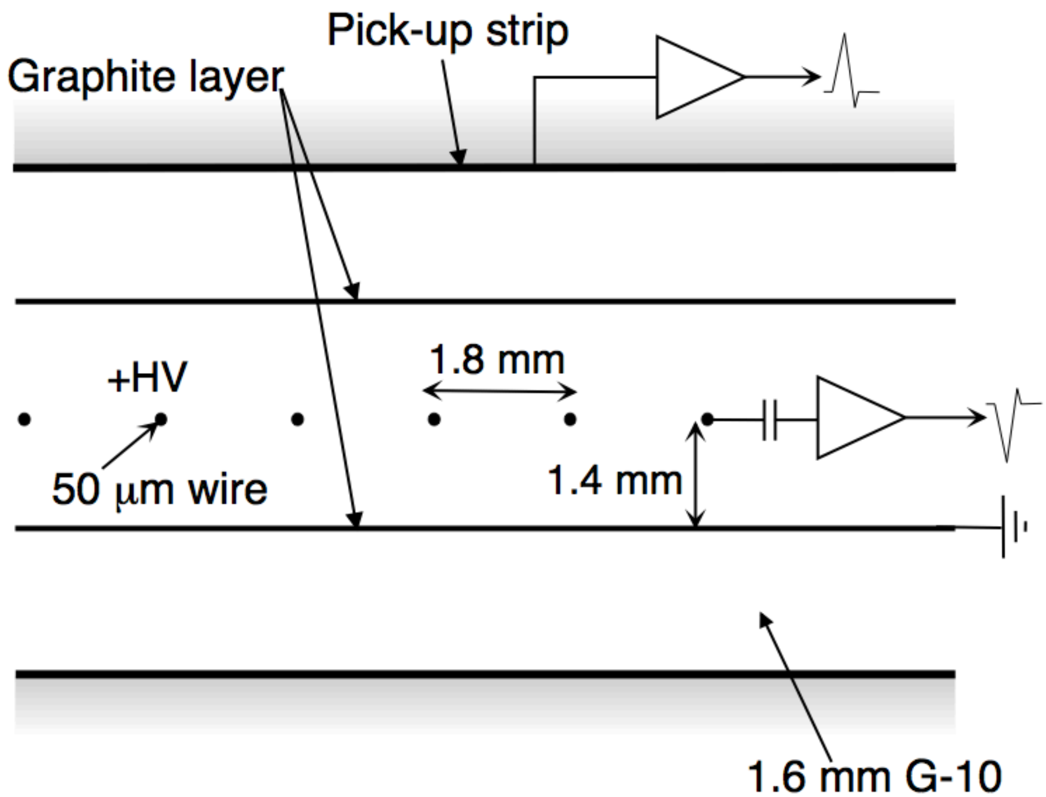

Figure 5.12: Schematic of TGC chamber, which is used for triggering in the muon end-cap region. [cite G35]

5.5 Magnet System

A particles with charge, q, and velocity v, moving in magnetic field, B, experiences a force, $F = qv \times B$. This force can cause charged particles to have a curved trajectory in magnetic fields, which the ID and MS use to determine the particles p_T. The central solenoid provides the magnetic field for the ID and the toroidal magnets provide the magnetic field for the MS.

The layout of the magnet system is shown in Figure 5.13. The central solenoid consists of a single-layer Al-stabilized NbTi conductor coil wound inside an Al support cylinder. The solenoid is 5.8 m long, 50 cm thick and has an inner radius of 1.23 m. It is cooled to 4.5 K to reach superconducting temperatures and shares the liquid argon calorimeter vacuum vessel to minimize material in the detector. A current of 7.730kA produces a 1.998 T solenodial magnetic field, pointing in the $+z$ direction.

The toroidal magnet system consists of a barrel and two end-cap toroidal magnets used to a magnetic field outside the calorimeters that is orientated along ϕ. Each barrel toroid is 25.3 m long with an inner and outer diameter of 9.4 and 20.1 m and weighs 830 tonnes. Endcap toroids are 5 m long with an inner and outer radius of 1.65 and 10.7 m. Both toroid systems use Al-stabilized Nb/Ti/Cu conductors. The magnetic field strength of the barrel and endcap regions are 0.5 and 1 T.

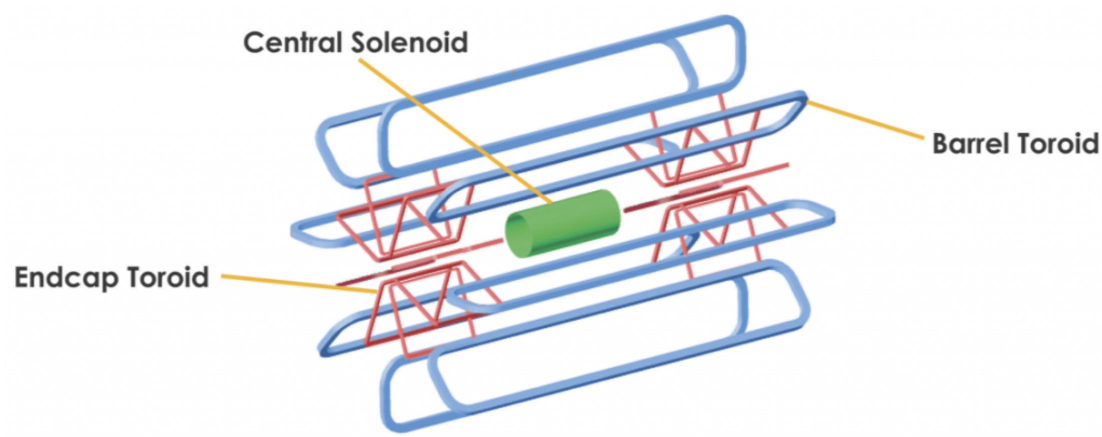

Figure 5.13: Layout of ATLAS magnet systems.

5.6 Trigger System

Since collisions occur every 25 ns and reading out all detector channels and storing that information is not currently feasible (saving 60 million megabytes per second), the majority of events are not kept for analysis. ATLAS uses a multi-stage trigger system to select approximately 1,000 of the 1.7 billion collisions that occur each second (corresponding to a rate of 1 kHz from the 40 MHz proton collision rate). The first stage of the trigger system is the hardware level (L1) trigger. This trigger reduces the event rate to 100 kHz by identifying Regions-of-Interest (ROIs) containing high p_T leptons, photons, jets, or E_T^{miss} by using information from RPCs, TGCs, and calorimeters to make a 2.5 μs decision. This information is then passed to a high-level trigger (HLT) which further decreases event rates to 1 kHz. The HLT uses finer granularity measurements from the MS and ID to preform simplified offline reconstruction to decide which events to keep.

Part III

Method

Chapter 6

Dataset and Simulated Samples

6.1 Dataset

This analysis uses pp collision data collected from 2015 to 2018 at $\sqrt{s} = 13$ TeV, corresponding to 139/fb of data as shown in Figure 6.1 and 6.2. From this dataset, only those events in which the tracker, calorimeters, and muon spectrometer have good data quality are used. For a given event, the solenoid and toroidal magnets must also be operating at their nominal field strengths. In addition to this, events must pass further quality checks to reject events where detector subsystems may have failed. These selections reject events that containing LAr noise bursts, saturation in the electromagnetic calorimeter, TileCal errors, and failures in event recovery due to tracker failures. Events with information missing from subsystems (usually due to busy detector conditions) are rejected. Events must also contain a primary vertex with at least two associated tracks, where the primary vertex is selected as the vertex with the largest $\sum p_T^2$ over tracks associated with the vertex and $p_T > 0.5$ GeV.

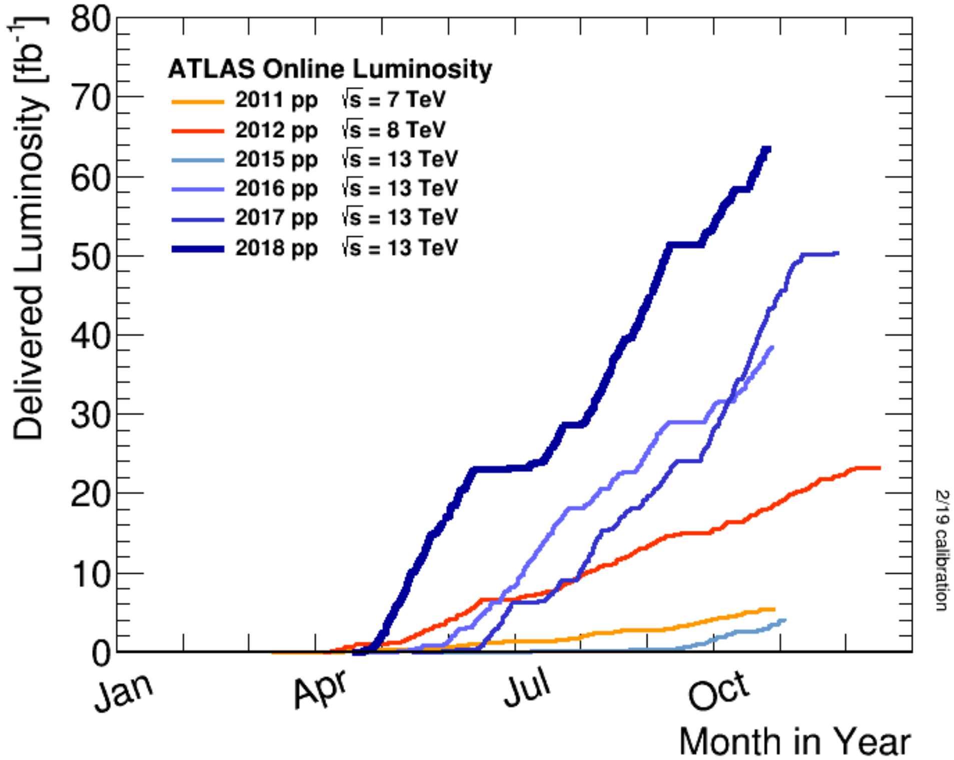

Figure 6.1: Integrated luminosity for data collected from ATLAS from 2011 - 2018

.

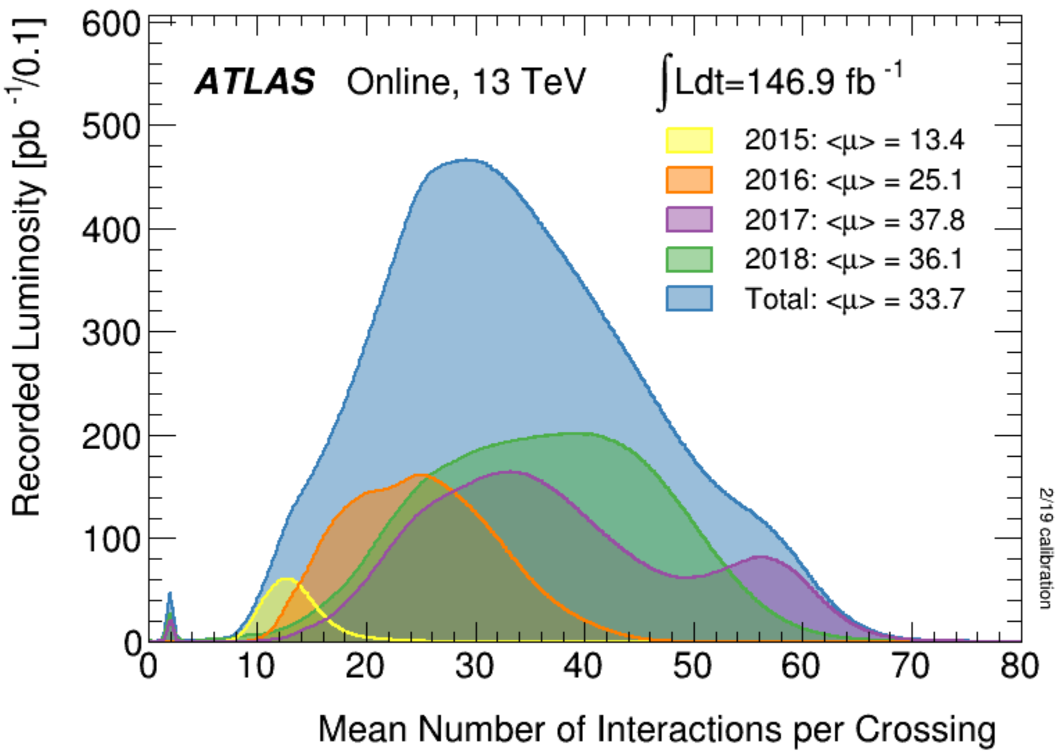

Figure 6.2: Mean number of interactions per crossing for data collected from ATLAS from 2011 - 2018

.

6.2 Simulated Samples

Samples are simulated in order to model backgrounds, evaluate signal acceptance, optimize event selection and estimate systematic and statistical uncertainties. The dominant backgrounds for this analysis are W/Z + jets, diboson (WZ/WW), $t\bar{t}$, single top and multijet production.

W/Z+jet events are simulated using Sherpa 2.2.1 at NLO [cite [29]] and merged with the Sherpa parton shower using the ME+PS prescription [11]. These events are then normalized to NNLO cross sections. The $t\bar{t}$ and single-top backgrounds are generated with Powheg-Box with NNPDF3.0NLO PDF sets in the matrix element calculation [cite[35]]. Top quarks are decayed using MadSpin [cite[36]]. For all processes, the parton shower, fragmentation, and underlying event are simulated using Pythia 8.320 with the A14 tune set[cite[ATL-PHYS-PUB-2014-02]]. Diboson processes are generated using Sherpa 2.2.1.

Signal samples are simulated using MadGraph 5-2.2.2 [cite 42] and Pythia 8.186 with NNPDF230LO. RS Graviton samples are generated with k/M_{PL}=1. HVT Model A and B samples are simulated with $g_H = -0.56$ and $g_f = -0.55$, as the difference in the width of the samples is smaller than detector resolution. Model C is generated by setting $g_H = 1$ and $g_f = 0$ to model VBF production of HVT bosons. Signals are generated for masses between 300 GeV and 6 TeV.

6.3 Object Selection

6.3.1 Electrons

Electrons are reconstructed from electromagnetic showers in the LAr EM calorimeter. During reconstruction cells of $\Delta\eta \times \Delta\phi = 0.025 \times 0.025$ are grouped into 3×5 clusters. These clusters are then scanned for local maxima that seed electron clusters. These clusters must then be matched to ID track from the PV. This requirement minimizes non-prompt electron and fake electron backgrounds. Electrons must pass identification and isolation requirements. Electron identification (loose, medium, tight) classification is based on the discriminant of the multivariate analysis that identifies electrons using a likelihood based method. For this analysis tight electrons are used. Electrons are also required to be isolated. The electron isolation is calculated by comparing the sum of the transverse momentum in a cone around the electron of size $\Delta R = 0.2$ to the transverse momentum of the electron. This quotient must be less than 3.5, to further reject non-prompt photons and other fake backgrounds (multijet). Electrons in this analysis are also required to have $p_T > 30$ GeV and $|\eta| < 2.47$. Electrons are also required to have $p_T > 30$ GeV.

Electrons are calibrated to determine a data-driven scale factors from $J/\Psi \to ee$, $Z \to ee$, $Z \to \ell\ell\nu$ processes. These corrections account for the non-uniform response of the detector by introducing modeling and reconstruction uncertainties.

6.3.2 Muons

As muons traverse the entire detector, they are reconstructed from ID and MS tracks. For this analysis the muon identification and isolation working points are chosen to minimize the contributions from non-prompt muons. Towards this end, the medium muon identification working point is used. For this working point, two types of reconstructed muons are used: combined and extrapolated muons (CB and ME, respectively). For CB muons, ID and MS tracks are reconstructed independently and a combined track fit is performed by adding or removing MS tracks to improve the fit quality. ME muons are reconstructed from only MS tracks with hits in at least two layers, which ensures the track originates from the

PV. ME muons extend the acceptance for muon reconstruction outside the ID from $2.5 < |\eta| < 2.7$. The medium identification working point uses CB and ME tracks. CB tracks must have at least 3 hits in two MDT layers. ME tracks are required to have at least three MDT/CSC hits. To further minimize contributions from fake muons, the selected muons are required to be isolated from other tracks, as muons from W, Z decays are often isolated from other particles. To insure the selected muons are isolated, the scalar sum of the transverse momentum of tracks in a cone of $\Delta R = 0.3$ compared to the transverse momentum of the muon must be less then 0.06. Muons are also required to have $p_T > 30$ GeV.

Muons are calibrated using well-studied resonances $J/\Psi \to \mu\mu$ (low-p_T), $Z \to \mu\mu$ (high-p_T). Figure 6.3 shows the combined muon p_T uncertainty from this calibration. The total systematic uncertainty is less then 1% for all p_T ranges considered in this analysis.

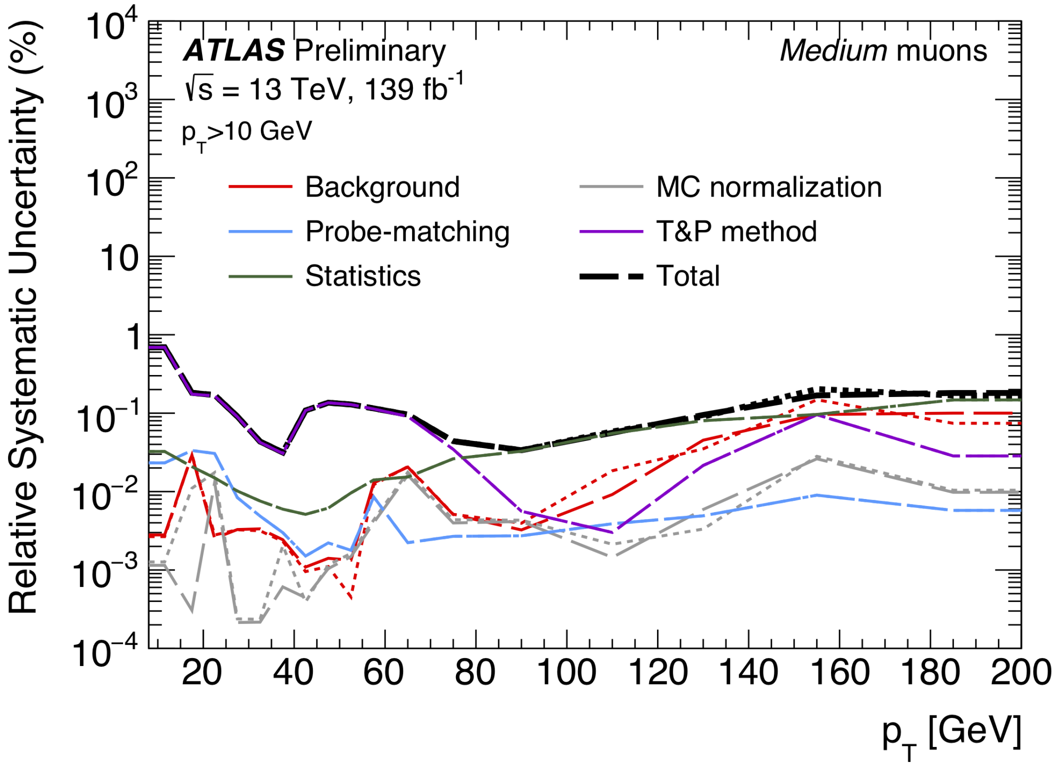

Figure 6.3: [4] This figure show the breakdown of the muon reconstruction efficiency scale factor measured in $Z \to \mu\mu$ as a function of p_T

.

6.3.3 small-R jets

Calorimeter jets are used to reconstruct the hadronically decaying W/Z candidates in the resolved analysis. These jets are less boosted and therefore spatially separated and reconstructed separately. These jets are constructed from topologically connected clusters of calorimeter cells (topoclusters), seeded from calorimeter cells with energy deposits significantly above the noise threshold. These cells are then used as inputs to the $anti - k_T$ algorithm [12] with a distance $= 0.4$, here called small-R jets. These jets are calibrated to compensate and account for biases from jet reconstruction.

The jet energy is calibrated sequentially as shown in Figure 6.4. After the jet direction is corrected to point to the PV, the energy of the jet is corrected. First, the jet energy is corrected to account for pileup contributions based on the p_T and area of the jet (these corrections are extracted from a $pp \rightarrow jj$ sample). Following this, another pileup correction is applied that scales with μ and N_{PV}.

Then, MC-based corrections are applied that are meant to transform the jet energy and η back to truth level. Therefore, these corrections account for the non-compensating nature of the ATLAS calorimeters and inhomogeneity of the detector. Following this the Global sequential calibration is applied that reduces flavor dependence and jet that deposit energy outside the calorimeters. Finally, in-situ corrections are applied that account for differences in jet responses between data and simulation (γ/Z+jet and multijet samples are used). These differences can be due to mismodelling of the hard scatter event, pile-up, jet formation, etc.

Jet used in this analysis must have $p_T > 30$ GeV and $|\eta| < 2.5$. To further reduce fake jets the jet-vertex-tagger (JVT) is used to reject pile-up jets [cite 43 P]. The JVT uses two track-based variables, corrJVF and R_{p_T} to calculate the likelihood that the jet originated from the PV. The corrJVF compares the scalar sum of the p_T of tracks associated with the jet and PV to the scalar sum of the p_T of tracks associated with the jet. This variable also includes a correction that reduces the depenency of corrJVF with the number of reconstructed vertices in the event. R_{p_T} is given by the ratio of the scalar sum of the p_T of tracks associated with the jet and PV to the p_T of the jet. Both of these variables peak around zero for pileup jets, as these jets are unlikely to have tracks associated with the PV. JVT cuts are applied to all jets with $p_T > 120$ GeV. Central jets ($|\eta| < 2.4$) are required to have a JVT > 0.59 and forward jets ($2.4 < |\eta| < 2.5$) are required to have JVT > 0.11.

To further reject fake jets, jets must pass quality requirements based on the following variables ([cite P42]):

- f_Q^{LAr}: fraction of energy of jet's LAr cells with poor signal shape
- f_Q^{HEC}: fraction of energy of jet's HEC cells with poor signal shape
- E_{neg}: sum of cells with negative energy
- f_{EM}: fraction of jet's energy deposited in EM calorimeter
- f_{HEC}: fraction of jet's energy deposited in HEC calorimeter
- f_{max}: maximum energy fraction in any single calorimeter layer
- f_{ch}: ratio of the scalar sum of the p_T of a jet's charged tracks to the jet's p_T

Jets selected for the resolved analysis must pass one of the following criteria:

- $f_{HEC} > 0.5$ and $|f_Q^{HEC}| > 0.5$ and $\langle Q \rangle > 0.8$
- $|E_{neg}| > 60$ GeV
- $f_{EM} > 0.95$ and $f_Q^{LAr} > 0.8$ and $\langle Q \rangle > 0.8$ and $|\eta| < 2.8$
- $f_{max} > 0.99$ and $|\eta| < 2$
- $f_{EM} < 0.05$ and $f_{ch} < 0.05$ and $|\eta| < 2$
- $f_{EM} < 0.05$ and $|\eta| > 2$

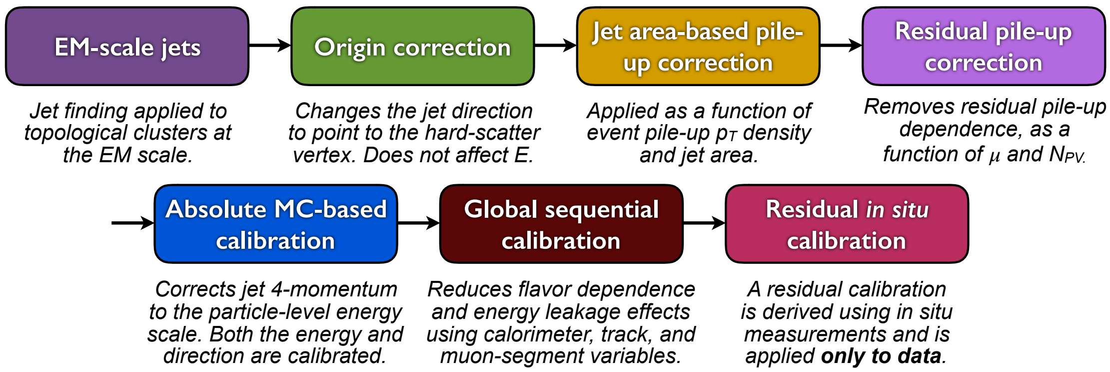

Figure 6.4: [6] This diagram shows the calibration stages for EM jets.

6.3.4 large-R jets

Large-R ($\Delta R = 1.0$) jets are used to reconstruct the high-p_T $W/Z \to qq$ candidates in the merged analysis. Track-Calo Clusters (TCCs) are used to reconstruct these jets [cite ANA 50]. These jets are constructed via a pseudo particle flow method using ID tracks matched to calorimeter clusters. The angular resolution of the calorimeter degrades sharply with jet p_T, but the jet energy resolution improves. The tracker has excellent angular resolution improves with p_T. Therefore, by matching tracks to jets, TCCs have more precise energy and angular resolution the jets constructed from calorimeter information only. These jets are required to have $p_T > 200$ GeV, $|\eta| < 2.0$ and $m_J > 50$ GeV.

TCC jets are trimmed as detailed in [cite ANA 45], which suppresses pileup and soft radiation in the jet, the jet mass is calculated as the four-vector sum of the jet's constituents (assuming massless constituents). The jet mass peaks around the W/Z boson mass for $W/Z \to qq$ jets, and more broadly for quark and gluon induced jets.

These jets are then tagged as W/Z jets if they pass the jet mass and D_2 cuts. The jet substructure variable D_2 is given by the ratio of energy correlation functions based on energies and pair-wise angles of a jet's constituents [cite ANA

46, 47]:

$$D_2^{\beta=1} = E_{CF3}\left(\frac{E_{CF1}}{E_{CF2}}\right)^3 \tag{6.1}$$

Where the energy correlation functions are defined as:

$$E_{CF1} = \sum_i p_{T,i} \tag{6.2}$$

$$E_{CF2} = \sum_{ij} p_{T,i} p_{T,j} \Delta R_{ij} \tag{6.3}$$

$$E_{CF3} = \sum_{ijk} p_{T,i} p_{T,j} p_{T,k} \Delta R_{ij} \Delta R_{jk} \Delta R_{ki} \tag{6.4}$$

A two-dimensional optimization of the jet mass and D_2 thresholds was performed to provide maximum sensitivity for this analysis. Figure **??** shows the optimized thresholds on D_2 and jet mass as a function of p_T. Figure 6.6 shows the efficiency of the optimized W/Z taggers as a function of jet p_T.

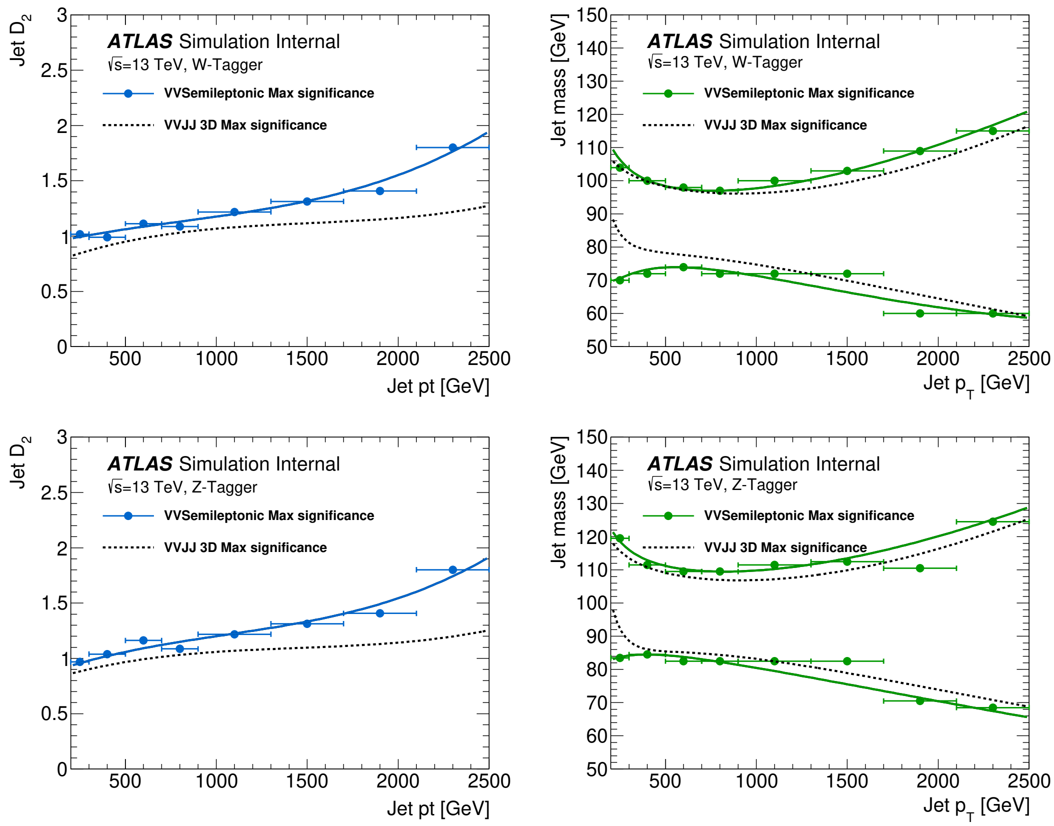

Figure 6.5: The upper cut on D_2 (a) and jet mass window cut i.e. the upper and lower boundary of the mass (b) of the W-tagger as a function of jet p_T. Corresponding values for Z-tagger are shown in (c) and (d). The optimal cut values for maximum significance are shown as solid markers and the fitted function as solid lines. Working points from $VV \to JJ$[ATLAS-HDBS-2018-31-002] is also shown as dashed lines as a reference. Natasha reword?

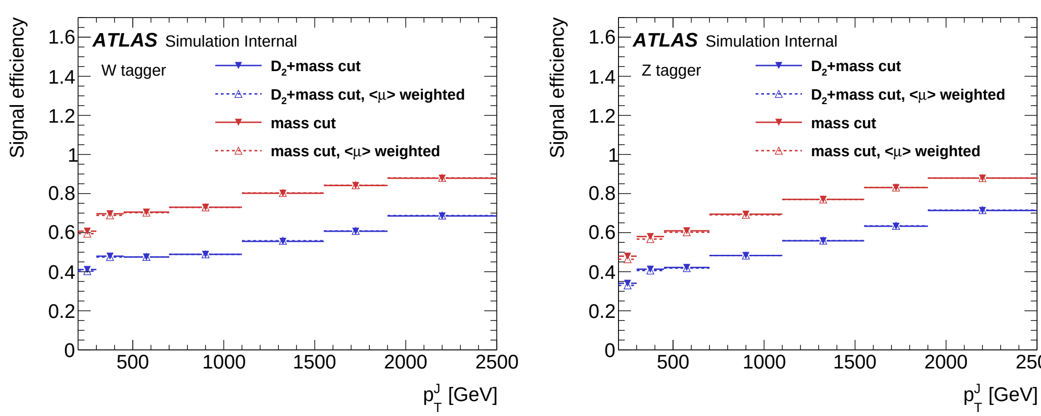

Figure 6.6: Natasha write caption

6.3.5 Variable Radius jets

Variable-radius (VR) track jets are used to identify b-quark induced jets in large-R jets [cite ANA 52]. These jets use a p_T dependent cone size defined as:

$$R_{eff}(p_{T,i} = \frac{\rho}{p_{T,i}} \tag{6.5}$$

for building jets from ID tracks with an anti-kt algorithm. For this analysis $\rho = 30$ GeV and an upper and lower limit on cone size are set to 0.02 and 0.4, respectively. Collinear VR jets are possible, so track jets that are not separated by the the smaller jet's cone size are not used. These jets are also required to have $p_T > 10$ GeV and $|\eta| < 2.5$.

6.3.6 MET/neutrinos

As neutrinos are uncharged and color less they do not leave tracks or jets in the detector. For this reason, neutrinos are reconstructed calculated the E_T^{miss}. This quantity is defined as negative vector sum of p_T all the physics objects and an extra "soft" term. The "soft" term accounts for energy depsoits not associated with any of the objects in the event. For this analysis the soft term is given by the summing the p_T of all ID tracks not associated with objects in the event. The selected tracks must be matched to the primary vertex, which decreases pile-up contamination [cite G 217 218]. The tight working point is used [Natasha look up what this means].

6.3.7 Jet Flavor Tagging

To further classify events, the small radius jets are identified as originated for a b-quark or not using the multivariate *b*-tagging algorithm (BDT), MC2c10 [cite G 210 199]. This algorithm uses the impact parameters of the jet's ID tracks, secondary vertices (if they exist), and reconstructed flight paths of b and c hadrons in the jet to determine if the jet was induced by a b-quark. For this analysis the 85% efficient working point of this algorithm is used to a fixed cut on the BDT discrimnant that yields an 85% tag rate, and c, τ, and light-flavor jet rejection of 3, 8, and 34 respectively in a simulated $t\bar{t}$.

6.3.8 Overlap Removal

The reconstructed jets and leptons in this analysis can arise from the same energy deposits. For instance, a jet may radiate an electron that is then reconstructed separately as the signal lepton in the event. To mitigate this confusion of multiple objects originating from a single jet or lepton overlapping objects are removed via a procedure referred to a overlap removal. In this procedure the separation of the two objects, $\Delta(R) = \sqrt{(\Delta\eta)^2 + (\Delta phi)^2}$ determines which object is removed from the event.

The overlap selections used in this analysis are:

- when an electron shares a track the electron with the lower p_T is rejected, as it is more likely to be a fake electron

- when a muon and electron share a track the muon is rejected if it is a calo-muon, otherwise the electron is rejected

- when $\Delta R < 0.2$ for an electron and jet, the jet is rejected to maximize signal acceptance

- when $\Delta R > 0.2$ for an electron and jet, the electron is rejected as likely originated from decays within the jet

- when $\Delta R < min(0.4, 0.04 + 10\text{GeV}/p_T^{\mu}$ the muon is rejected, again maximizing signal acceptance, otherwise the jet is rejected

- when $\Delta R < 1.0$ for the a large-R jet and electron, the jet is rejected

Chapter 7

Event Selection and Categorization

7.1 Pre-selection

Before applying topological cuts to suppress backgrounds and reduce data size in this search, preselection cuts are applied which include trigger and event requirements. Events must contain exactly one tight lepton (no additional loose leptons), the $p_T^{\ell\nu} > 75$ GeV, and there must be at least two small-R jets or one large-R jet.

7.2 Trigger

The data was collected using the lowest unprescaled single-lepton or E_T^{miss} triggers, as summarized in Table [natasha add table]. Since the muon term is not considered in the trigger E_T^{miss} calculation, the E_T^{miss} trigger is fully efficient to events with high-p_T muons. For this reason, the E_T^{miss} trigger is used for events where $p_T^{\mu} > 150$ GeV, to compensate for the poor efficiency of the single muon trigger below 150 GeV (due to detector coverage).

Table 7.1: The list of triggers used in the analysis.

Data-taking period	$e\nu qq$ channel	$\mu\nu qq$ ($p_T(\mu\nu) < 150$ GeV) channel	$\mu\nu qq$ ($p_T(\mu\nu) > 150$ GeV) channel
2015	HLT_e24_lhmedium_L1EM20 OR HLT_e60_lhmedium OR HLT_e120_lhloose	HLT_mu20_iloose_L1MU15 OR HLT_mu50	HLT_xe70
2016a (run < 302919) ($L < 1.0 \times 10^{34}\,cm^{-2}\,\mathrm{s}^{-1}$)	HLT_e26_lhtight_nod0_ivarloose OR HLT_e60_lhmedium_nod0 OR HLT_e140_lhloose_nod0 HLT_e300_etcut	HLT_mu26_ivarmedium OR HLT_mu50	HLT_xe90_mht_L1XE50
2016b (run $\geq$ 302919) ($L < 1.7 \times 10^{34}\,cm^{-2}\,\mathrm{s}^{-1}$)	same as above	same as above	HLT_xe110_mht_L1XE50
2017	same as above	same as above	HLT_xe110_pufit_L1XE55
2018	same as above	same as above	HLT_xe110_pufit_xe70_L1XE50

7.3 GGF/VBF RNN

To classify events as originating from GGF/DY or VBF production a recursive neural network (RNN) is used. This approach is more powerful than a cut-based classification as it improves signal efficiency and analysis sensitivity by exploiting correlations between variables that the RNN learns. In particular, a RNN architecture is ideal as it can handle variable numbers of jets in the events.

The RNN uses the four-momentum of candidate VBF jets to classify events as VBF or GGF topologies. As sometimes jets will be incorrectly reconstructed the number of jets in the event are expected to vary across the inputs samples. VBF candidate jets are identified by removing jets from the event that are likely from $W/Z \to qq$. For the resolved regime this means removing the two leading small-R jets from the VBF candidate jet list. For the merged regime this means removing small-R jets that are $\Delta R < 1.0$. Also the VBF candidate jets are also required to be within $|\eta| < 4.5$. From the list of remaining VBF candidate jets, the two highest-p_T jets are chosen.

The architecture of the RNN is show in Figure 7.1. LSTMs are a type of RNN that extract meaningful information and can retain it (unlike other neural networks architectures). This is useful for VBF event classification for events with two jets, where using the kinematic properties of both jets (and their correlations) will lead to more efficient event classification.

In this RNN architecture, the VBF candidates are first passed to a masking layer which checks the number of jets in the event. If there is only one jet, only one LSTM layer is used. The output of masking is then passed to a LTSM cell (with a tanh activation) [natasha cite LSTM], and then to a dropout layer, that has a probability of 0.3 to completely forget the output of the LSTM. Dropout is a regularization method, that prevents overfitting. The output of the dropout layer is then passed to the second LSTM and then through another dropout layer with a probability of 0.3.

The weights and other parameters of the network are learned by training the network with VBF and GGF signals over 200 epochs with an Adam Optimizer [natasha add reference]. The training is truncated if the network parameters are unchanged after ten iterations. The training, testing and validation sets are 56, 30, and 14 percent of the input samples, respectively. Figure [add INT figure 32] shows the loss function of the network as a function of training epochs. The validation test set has a smaller loss function as dropout was not applied. Figure 7.3 shows the ROC curve for the RNN using k-fold cross validation.

Finally this output is passed to a dense layer [natasha ask antonio about this] and then to a sigmoid activation layer, leading to an overall RNN score. Figure 7.2 shows the RNN discriminant for shows modeling of the discriminant. The RNN score is 0 for GGF and background processes and 1 for VBF processes. Figure **??** shows the limits for various signal processes based on the RNN cut applied. The most efficient cut was found to be RNN Score > 0.8, for VBF classification.

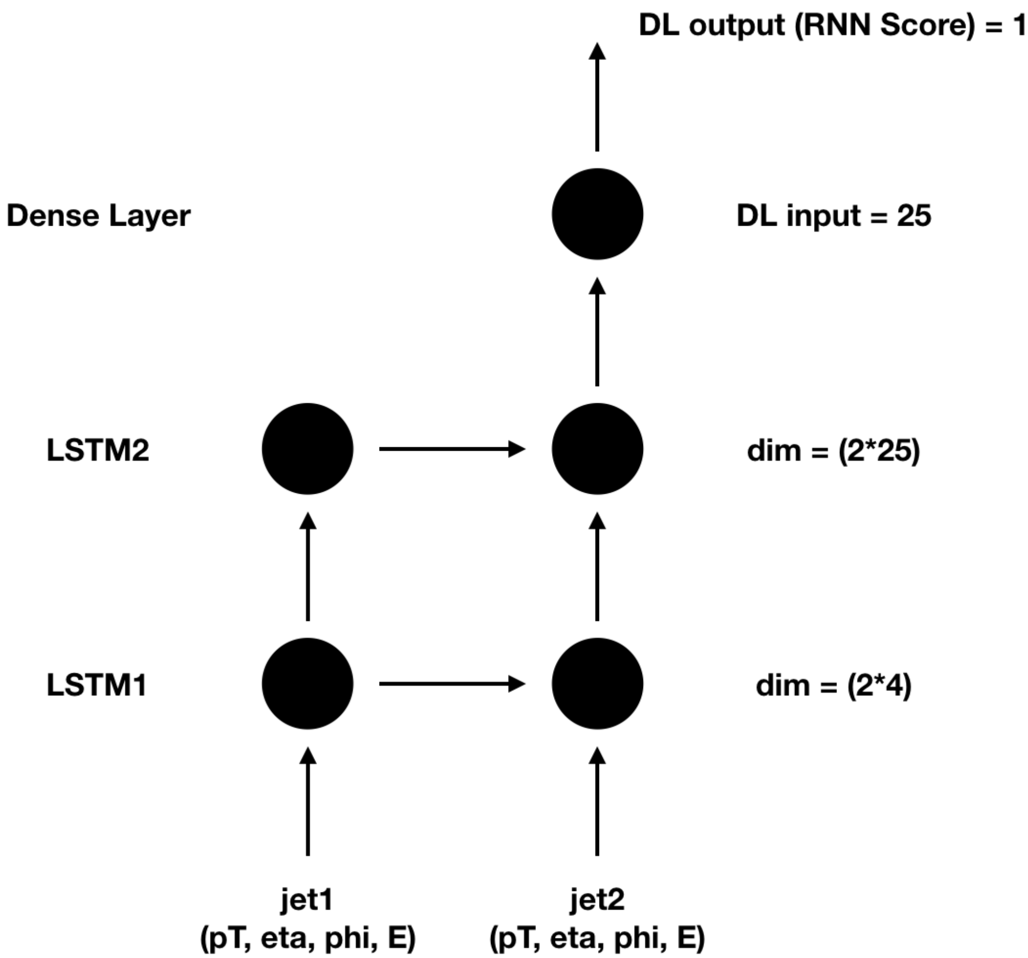

Figure 7.1: RNN architecture. Natasha add caption

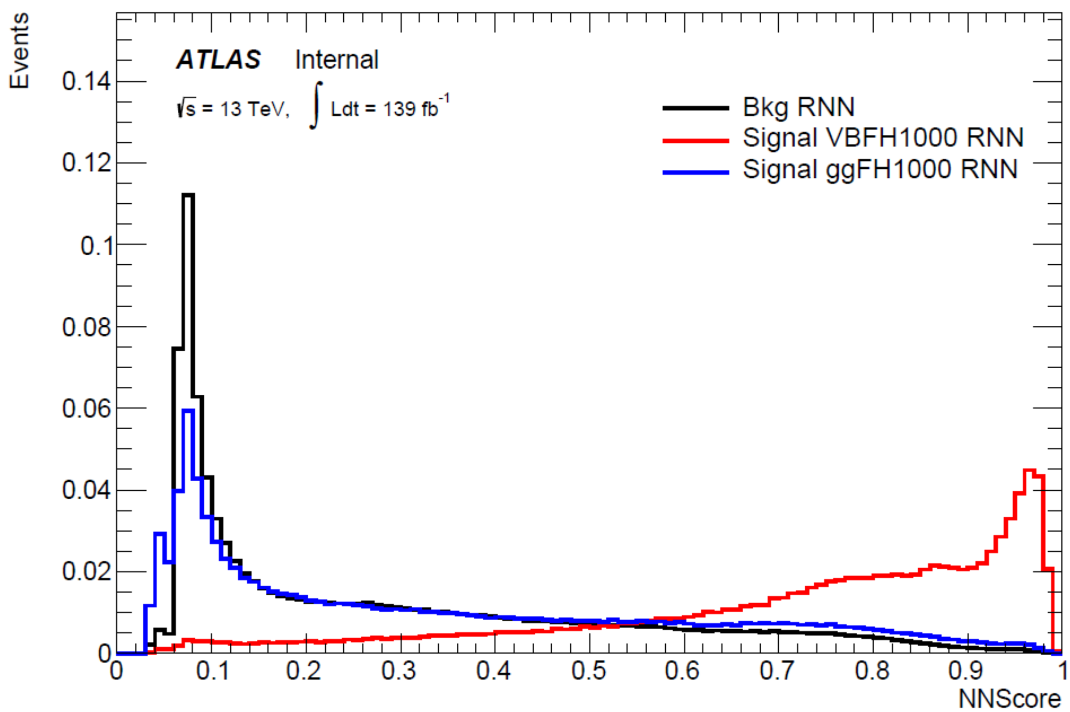

Figure 7.2: RNN Score distribution for ggF and VBF signals and backgrounds.

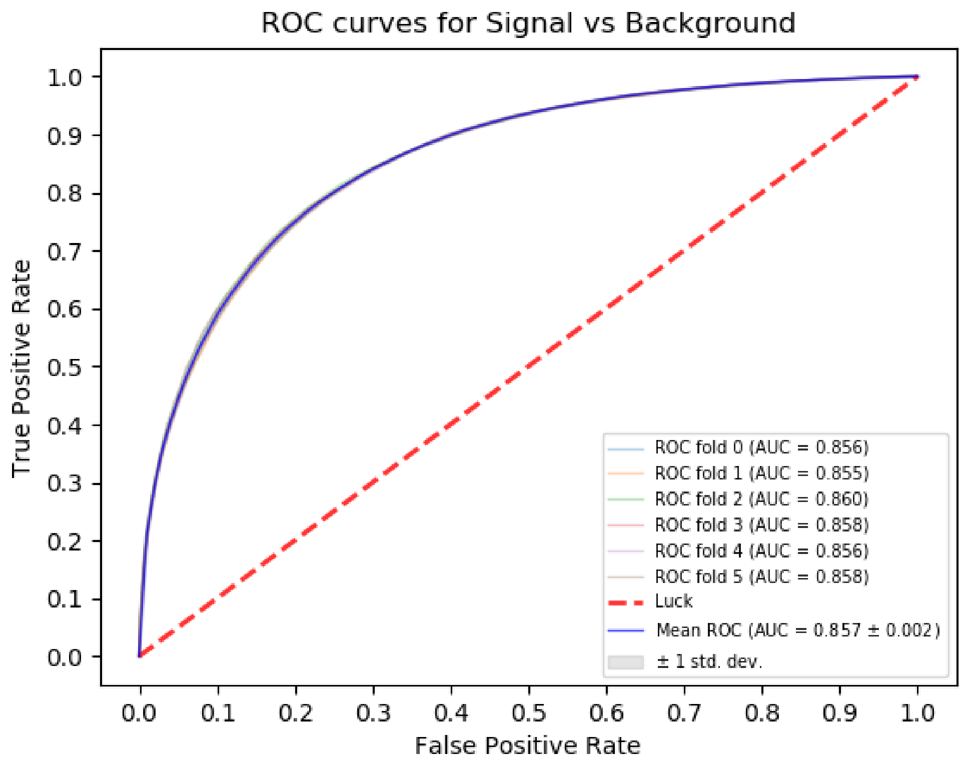

Figure 7.3: ROC curve using k-fold validation for RNN.

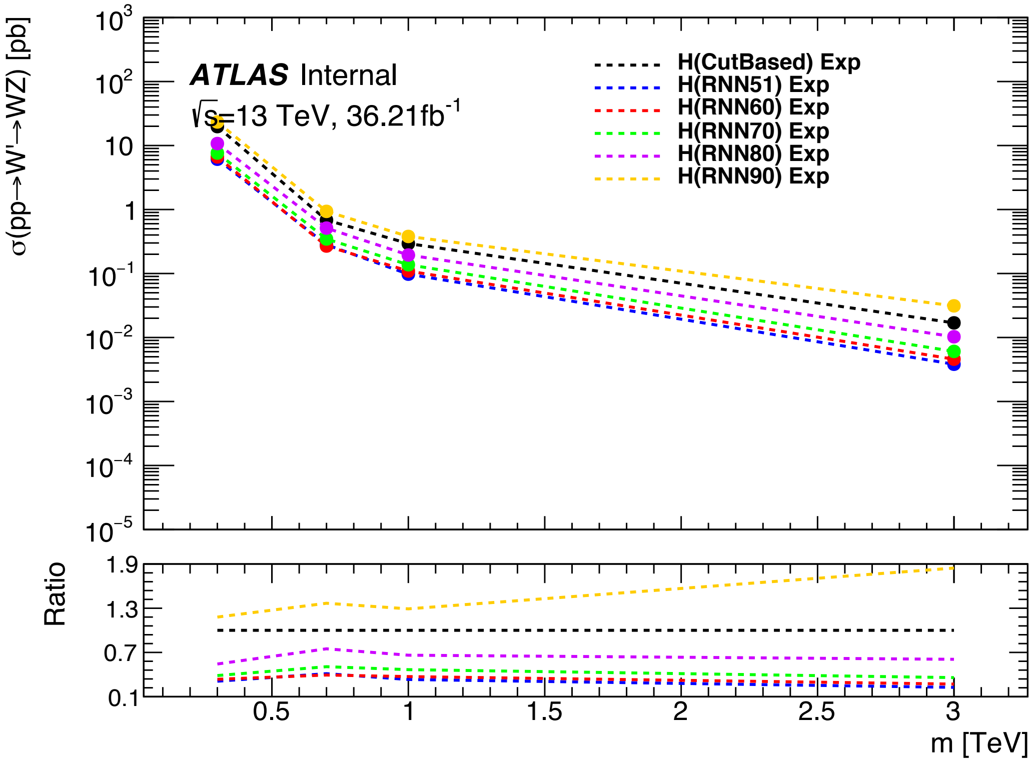

Figure 7.4: Comparison of GGF Z' limits for different RNN score selections.

7.4 Topological Cuts

Once an event is classified as VBF or GGF via the RNN it must pass other topological cuts that maximize signal efficiency and background rejection. First, to efficiently select events with $W \to \ell\nu$ candidate exactly one tight lepton is required and $E_T^{miss} > 100(60)$ GeV and $p_{T,\ell\nu} > 200(75)$ GeV in the merged (resolved) analysis to suppress the multi-jet background. To more accurately model the two dominant backgrounds in this analysis, W+jets and $t\bar{t}$, control regions are used constructed for each. These control regions are dominated by these processes and used to extract normalization factors that are then used in the signal region estimates.

For the merged analysis, in addition to the $W \to \ell\nu$ and $W/Z \to J$ selections above, the relative boson p_T is cut to enhance signals, i.e. $\min(p_{T,\ell\nu}, p_{T,J})/m_{WV} > 0.35(0.25)$ for the GGF (VBF) category. To minimize $t\bar{t}$ contamination the signal region and W+jets control region events with at least one b jet with $\Delta R > 1.0$ from the large-R jet are excluded. For the $t\bar{t}$ control region the event must contain at least one such b jet. High purity signal regions require the D_2 and W/Z mass window cut to be passed, whereas the low purity region only requires the W/Z mass window cut to be passed. Finally for events to be classified as tagged the large-R jet must contain exactly two b-tagged jets. Untagged events must have no more than one b-tagged jet matched to the large-R jet. These selections are shown in Table 7.2. The distributions for the variables used in merged analysis for top control regions are shown in Figure 7.6- 7.9.

Events failing the merged selection are then re-analyzed in the resolved category. To enhance resolved signals, the event should contain two high-p_T boson that are back-to-back in the x-y plane as shown by the cuts in Table 18. Again to suppress the $t\bar{t}$ background in the WCR and SR events are required to have no additional b-jets.

The WV system mass, m_{WV} is reconstructed from the lepton, neutrino, and hadronically-decaying boson candidate. The momentum of the neutrino along the z-direction is obtained by constraining the $W((Z)$ boson mass of the lepton neutrino system to be 80.3 (91.8) GeV/c^2. For complex solutions to this constraint, p_Z is taken as either the real component of the complex solutions or the one with the smaller absolute value of the two real solutions. For the resolved analysis, m_{WV} is reconstructed by constraining the $W(Z)$ dijet system:

$$p_{T,jj}^{corr} = p_{T,jj} \times \frac{m_{W/Z}}{m_{jj}} \tag{7.1}$$

$$m_{jj}^{corr} = m_{W/Z} \tag{7.2}$$

Table 7.2: Summary of selection criteria used to define the signal region (SR), W+jets control region (W CR) and $t\bar{t}$ control region ($t\bar{t}$ CR) for merged 1-lepton channel.

Selection		SR		W CR (WR)		$t\bar{t}$ CR (TR1)	
		HP	LP	HP	LP	HP	LP
$W \to \ell\nu$	Num of Tight leptons	1					
	Num of Loose leptons	0					
	E_T^{miss}	> 100 GeV					
	$p_T(\ell\nu)$	> 200 GeV					
$W/Z \to J$	Num of large-R jets	≥ 1					
	D_2 cut	pass	fail	pass	fail	pass	fail
	W/Z mass window cut	pass	pass	fail	fail	pass	pass
	Numb. of associated VR track jets b-tagged	For $Z \to J$: ≤ 1 (= 2) for untagged (tagged) category					
Topology cut	$\min\left(p_{T,\ell\nu}, p_{T,J}\right)/m_{WV}$	> 0.35(0.25) for DY/ggF (VBF) category					
Top-quark veto	Num of b-tagged jets outside of large-R jet	0				≥ 1	
Pass VBF selection		no (yes) for DY/ggF (VBF) category					

where m_{jj} and $m_{W/Z}$ are the reconstructed invariant mass of the hadronically-decaying W/Z boson and the PDG values of the W/Z boson masses, respectively. A summary of the resolved selections is shown in Table 7.3.The distributions for the variables used in the resolved analysis in the TCR are shown in Figure 7.10, 7.11.

Events classified as VBF events are classificed as Merged High purity, low purity or resolved signal region selections sequentially. If the event does not pass any of these selections but passes a VBF control region selection it is classified as a VBF CR event. If the event fails the VBF selection it is then checked if it passes the Merged High purity, Low purity or resolved signal region selections (NB: for the WZ decay modes all the region have tagged and untagged categories). If the event fails all the GGF signal region selections, it is then kept for GGF control region selections, if it passes those selections. This cutflow is shows in Figure 7.5.

Table 7.3: The list of selection cuts in the resolved analysis for the WW and WZ signal regions (SR), W+jets control region (WR) and $t\bar{t}$ control region (TR).

cuts		SR	W CR (WR)	$t\bar{t}$ CR (TR1)
$W \to \ell\nu$	Number of Tight leptons	1		
	Number of Loose leptons	0		
	E_T^{miss}	> 60 GeV		
	$\$p_T(\ell\nu)$	> 75 GeV		
$W/Z \to jj$	Number of small-R jets	≥ 2		
	Leading jet p_T	> 60 GeV		
	Subleading jet p_T	> 45 GeV		
	$Z \to q\bar{q}$	$78 < m_{jj} < 105$ GeV	$50 < m_{jj} < 68$ GeV or	$50 < m_{jj} < 150$ GeV
	$W \to q\bar{q}$	$68 < m_{jj} < 98$ GeV	$105 < m_{jj} < 150$ GeV	
	Num. of b-tagged jets	For $Z \to jj$: ≤ 1 ($= 2$) for untagged (tagged) category		
Topology cuts	$\Delta\phi(j, \ell)$	> 1.0		
	$\Delta\phi(j, E_T^{miss})$	> 1.0		
	$\Delta\phi(j, j)$	< 1.5		
	$\Delta\phi(\ell, E_T^{miss})$	< 1.5		
	$\min(p_{T,\ell\nu}, p_{T,jj})/m_{WV}$	$> 0.35(0.25)$ for DY/ggF (VBF) category		
Top veto	Number of additional b-tagged jets	0		≥ 1
Pass VBF selection		no (yes) for DY/ggF (VBF) category		

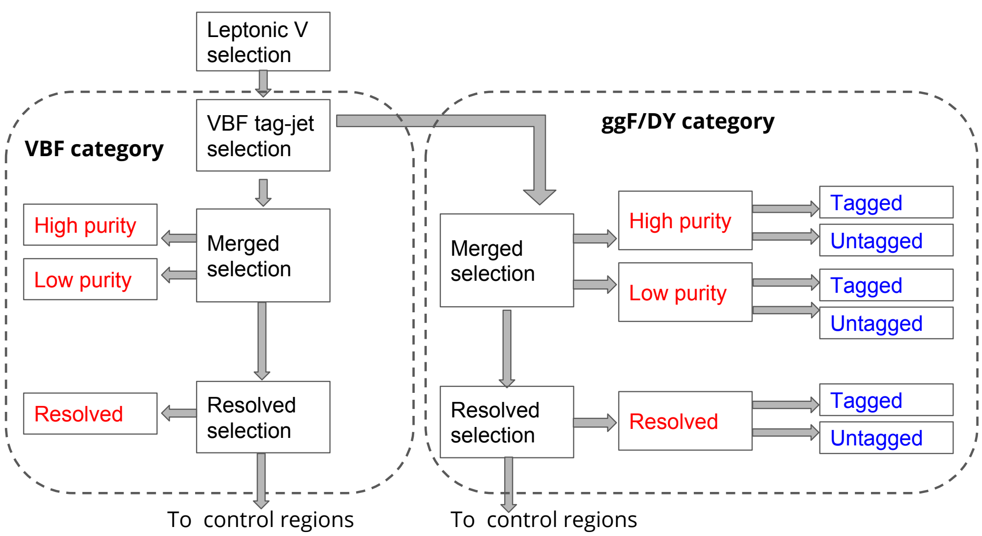

Figure 7.5: Event Categorization. Natasha write more.

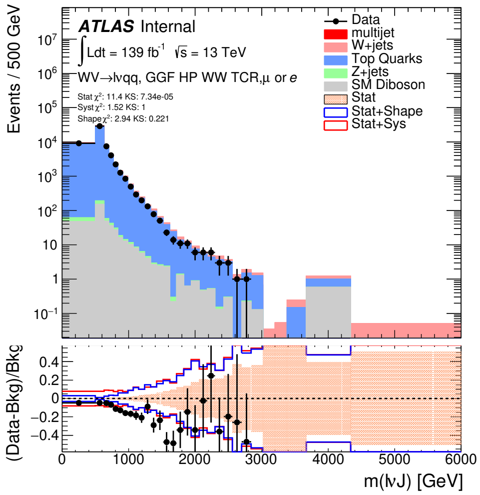

(a)

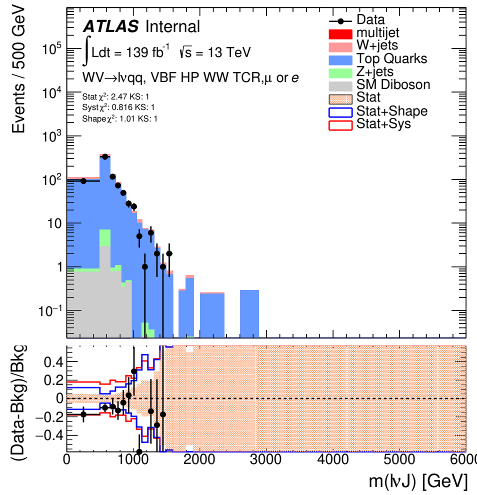

(b)

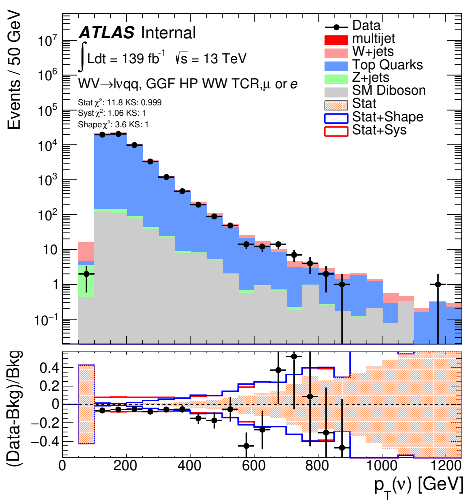

(c)

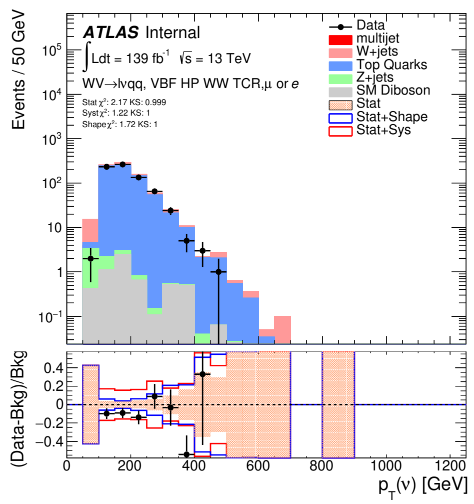

(d)

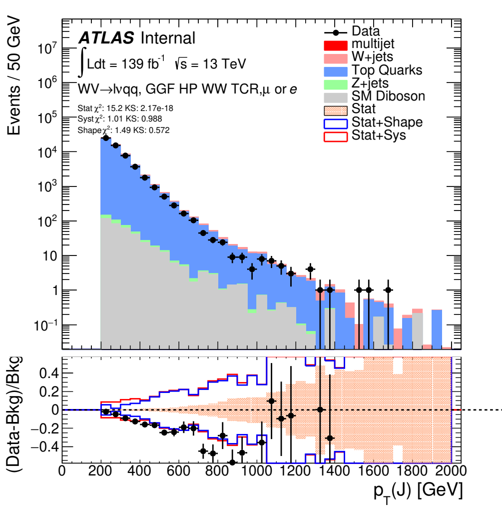

(e)

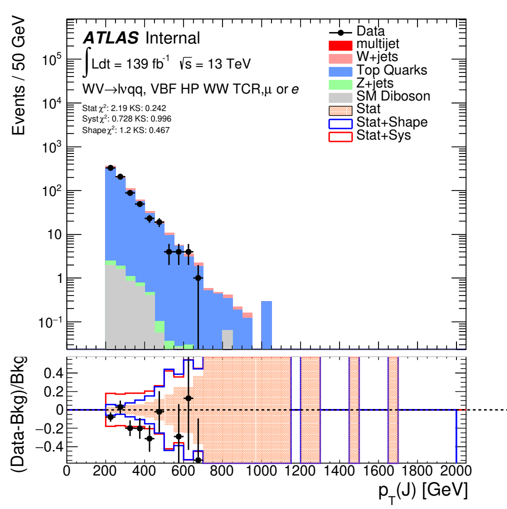

(f)

Figure 7.6: Data MC comparison for the merged WW HP TCR.

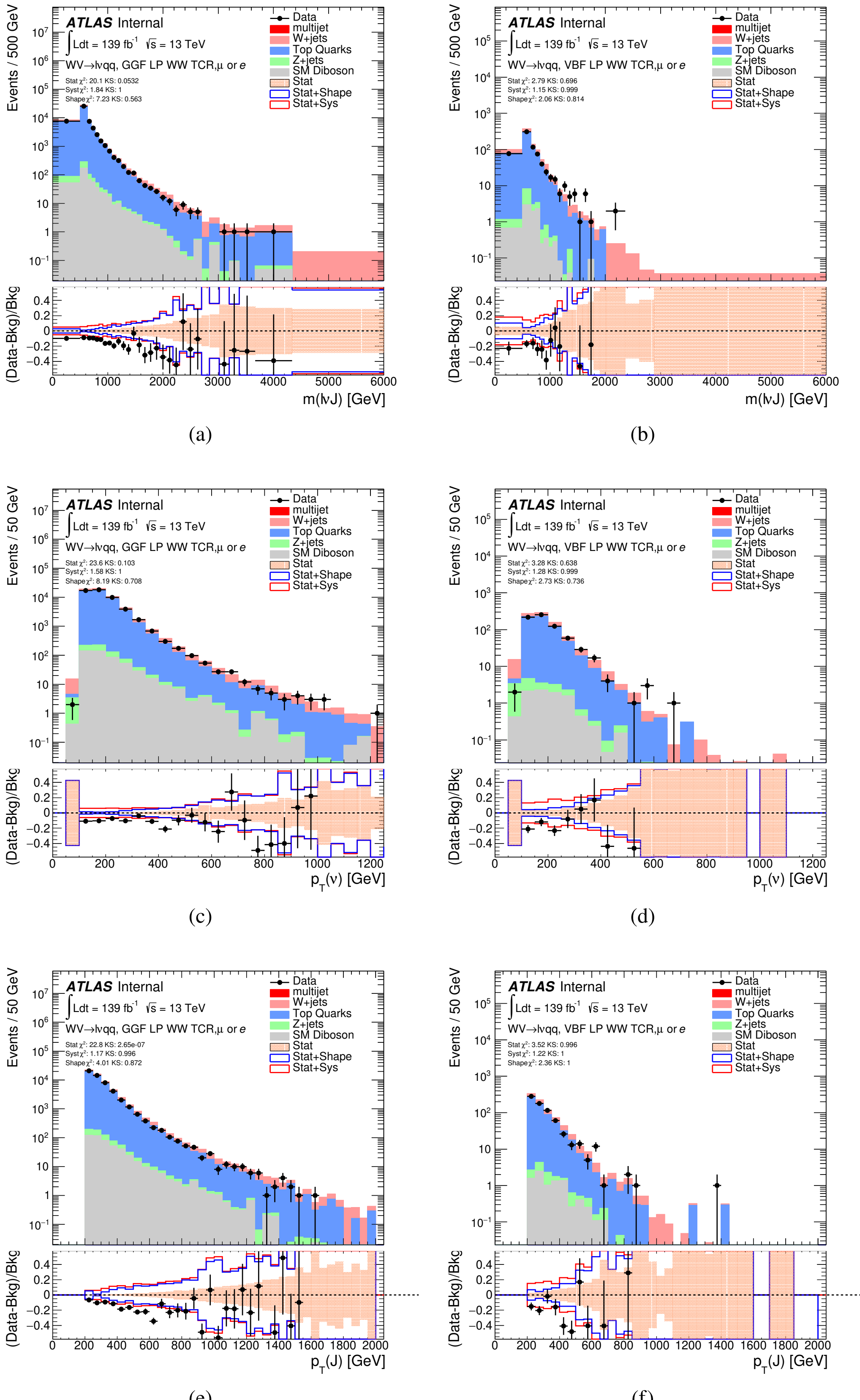

Figure 7.7: Data MC comparison for the merged WW LP TCR.

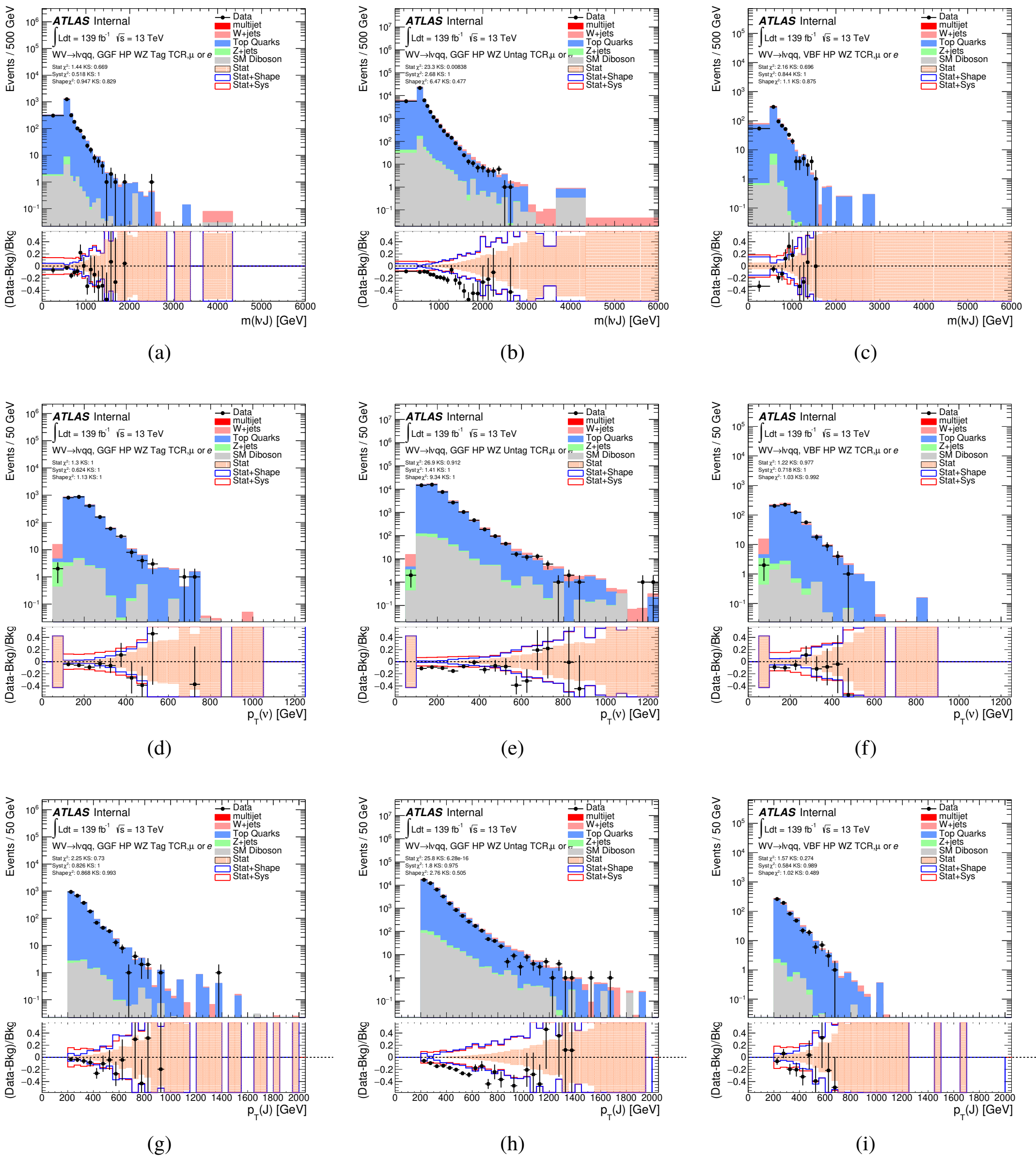

Figure 7.8: Data MC comparison for the merged WZ HP TCR.

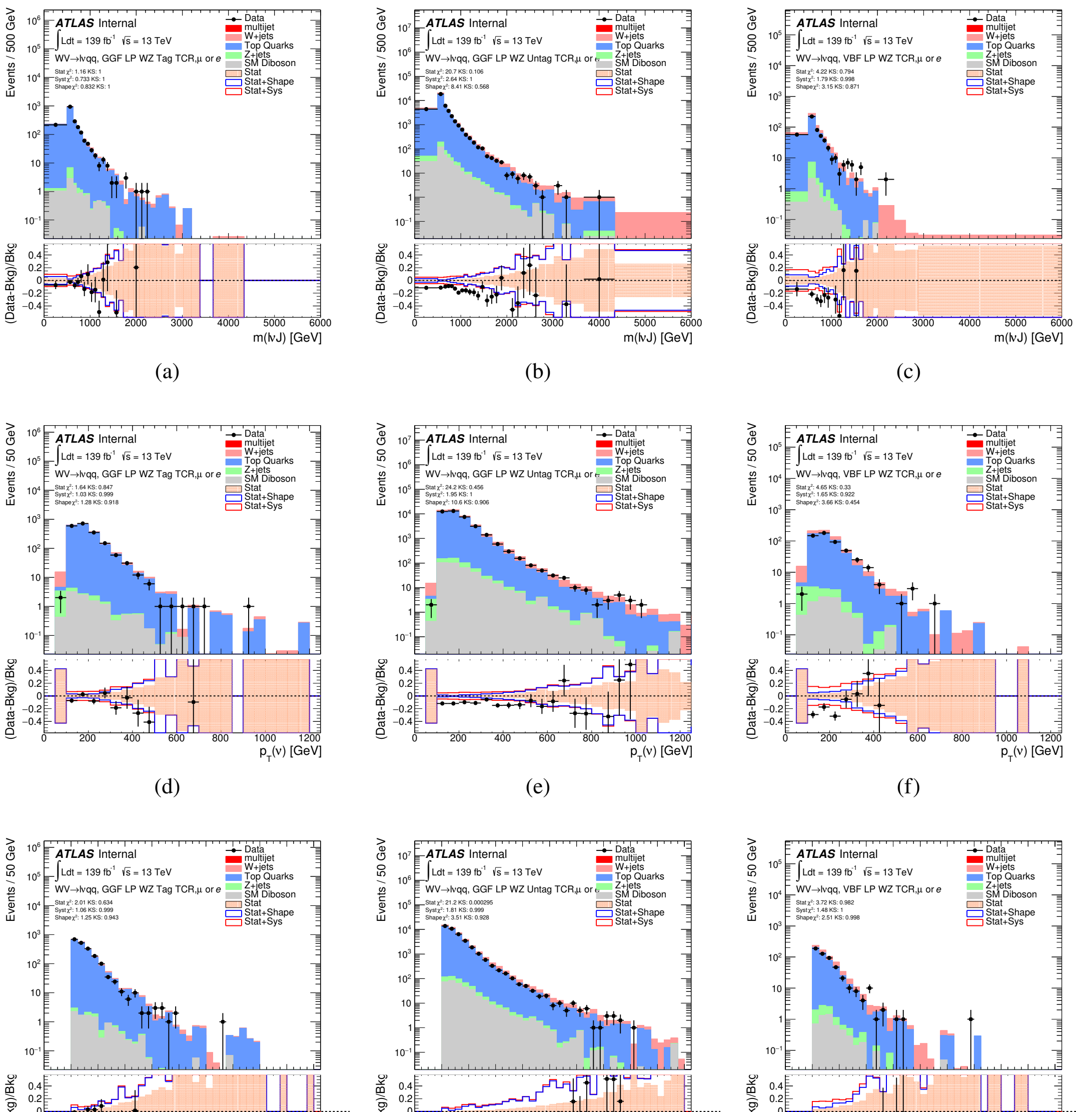

Figure 7.9: Data MC comparison for the merged WZ LP TCR.

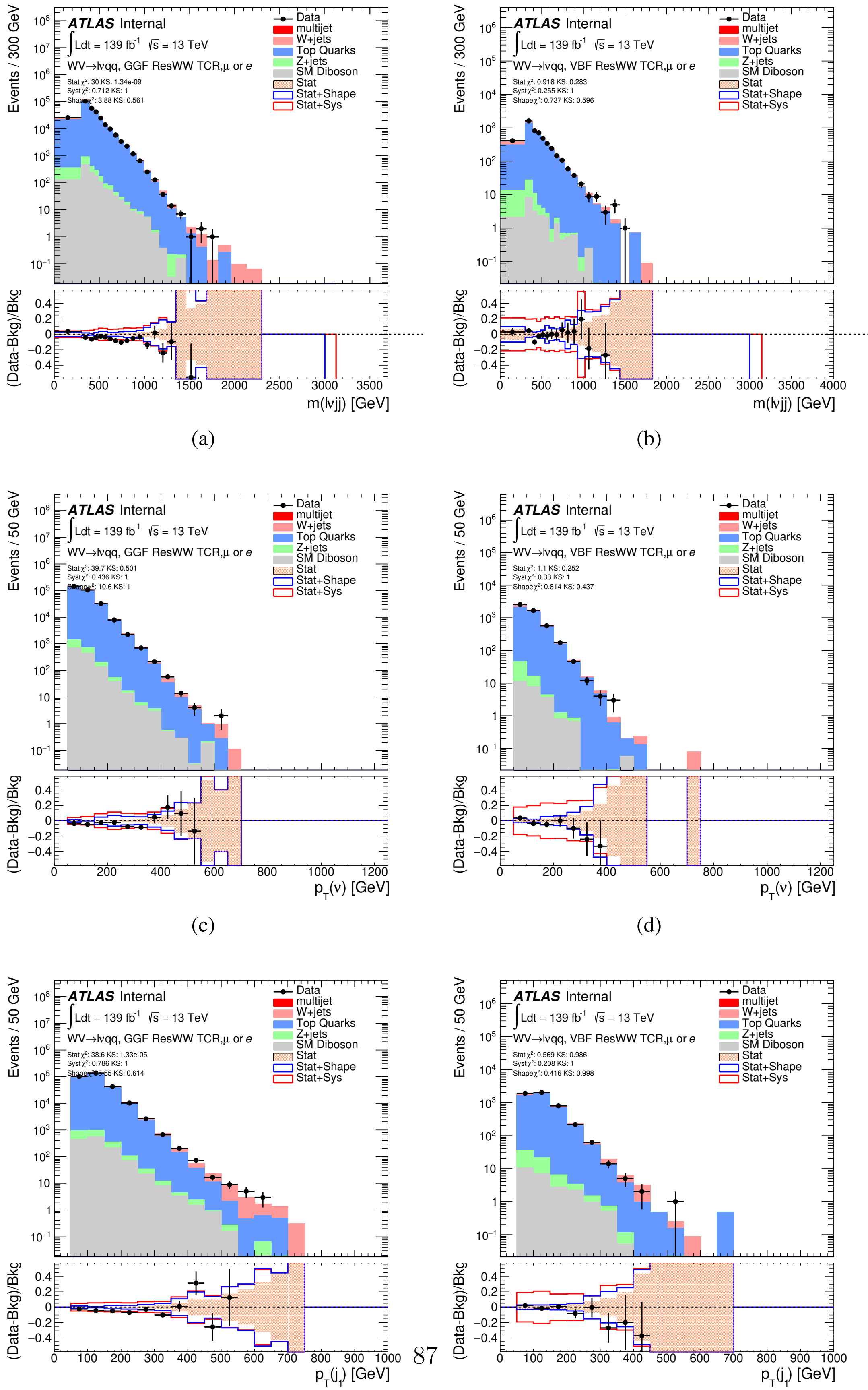

(a) (b) (c) (d) (e) (f)

Figure 7.10: Data MC comparison for the resolved WW TCR.

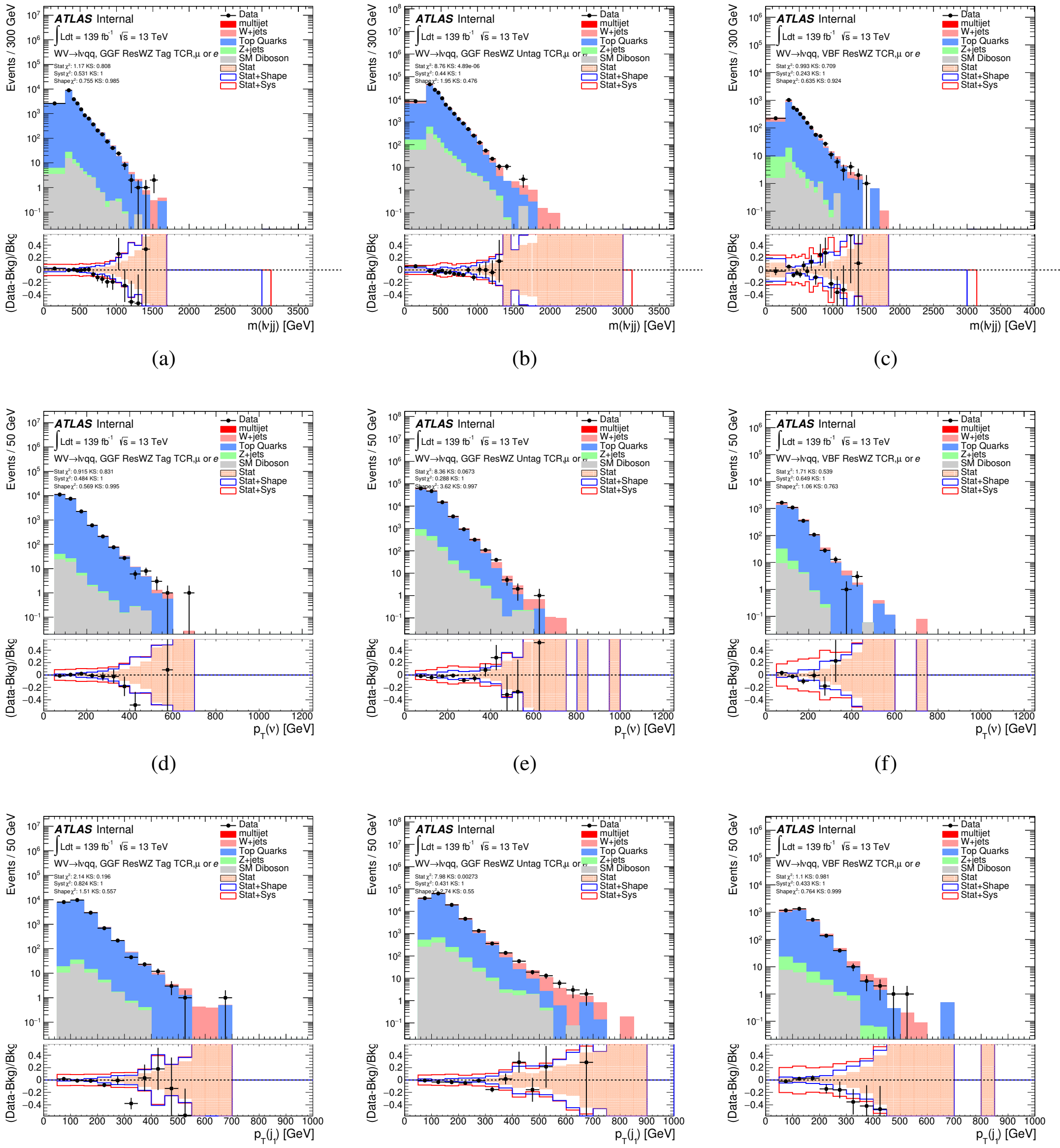

(a) (b) (c)

(d) (e) (f)

(g) (h) (i)

Figure 7.11: Data MC comparison for the resolved WZ TCR.

7.5 Background Estimate

7.5.1 Multijet Sample

Backgrounds in this analysis containing real leptons (e.g. W/Z+jets, diboson, $t\bar{t}$, single-t) are well-modeled with simulated samples and constrained with data from CRs. However, the multijet background containing fake leptons is not well-modeled with simulation. For this reason, the multijet background is extracted from data. Heavy flavor decay products, jets, and converted photons can be mistakenly reconstructed as jets. Fake electrons often arise from jet fakes while fake muons may also arise from heavy flavor decay. For this analysis, these fake electrons generally fail the electron ID criteria and fake muons fail the muon isolation requirement. Therefore, to derive the multijet template shape the SR and CR selections and inverted lepton requirements are used as seen in Table 7.4. NB: by inverting the lepton isolation/identification criteria the CR and SRs created are orthogonal to the CR and SRs.

The template shape of the MJ background is determined by using a multijet validiation region (MJVR) that requires the inverted lepton isolation/id requirement and the two signal jets to satisfy the m_{jj} requirement used in the W+jets CRs. The E_T^{miss} distribution in MJCR is shown in Figure 7.12 for 2017 data. The template is then extracted by subtracting the data in the MJVR from the electroweak background processes. This template is then added in the WCR and a "pre-MJ-fit" is preformed. In this fit the E_T^{miss} distribution is fit with the electroweak background normalizations constrained to expected ranges and the multijet electron and muon background normalizations free to float. The fitted scale factors from this MJVR template are then applied in the MJCR template. The fitted uncertainties on the MJCR normalizations are then used to create the

MJ template in the SRs. The electron and muon background normalizations are parameters in the final simulateous fit. Technically, there should be a separate template for every CR and SR, but some MJ regions have insufficient statistics to do this. Additionally, the shapes for the MJ templates for VBF and ggF regions are found to be compatible within statistical uncertainty. Therefore, the sample MJ template used for VBF and ggF CR/SRs, but with different pre-MJ-fit scale factors.

This template method was validated using WCR and full Run 2 data. The results of the fit are shown in Table 7.5. The multijet contribution in the muon channel for $p_T^W > 150$ GeV is consistent with zero, and therefore neglected in the final fit. Applying the extracted normalization factor to MJVR in WCRs for various kinematic variables such as E_T^{miss}, W transverse mass, lepton p_T, and the invariant mass as show in Figures 7.13 -7.22. These figures show good agreement between the data and background estimate.

	Criterion	signal lepton	inverted lepton
Electron	ID	TightLH	MediumLH !TightLH
	Calo Isolation	FixedCutHighPtCaloOnlyIso	FixedCutHighPtCaloOnlyIso
Muon	ID	WHSignalMuon	WHSignalMuon
	Track Isolation	FixedCutTightTrackOnlyIso	!FixedCutTightTrackOnlyIso $ptvarcone30/pt < 0.07$*
	*Only applied to events with $pTW < 150GeV$		

Table 7.4: Definitions of “inverted” leptons used in multijet control region

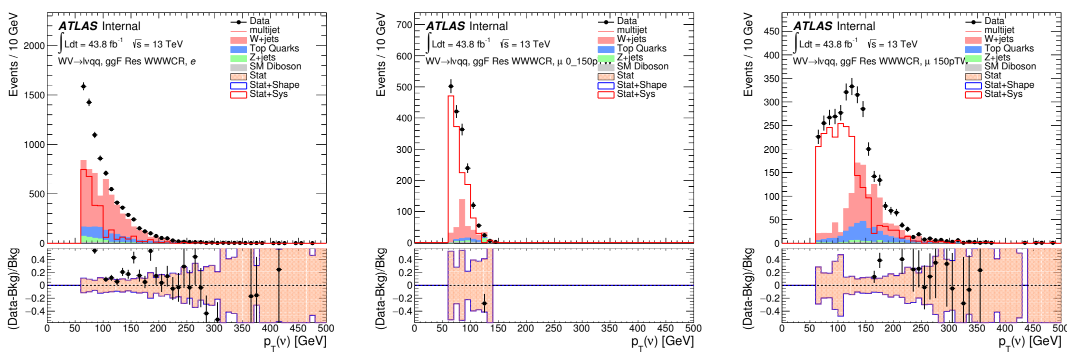

(a) (b) (c)

Figure 7.12: The E_T^{miss} distribution in MJCR for 2017 data in the electron channel(left), muon channel with W-boson pT < 150 GeV (center) and > 150 GeV (right). Multi-jet templates are calculated as remaining data components after excluding known MC

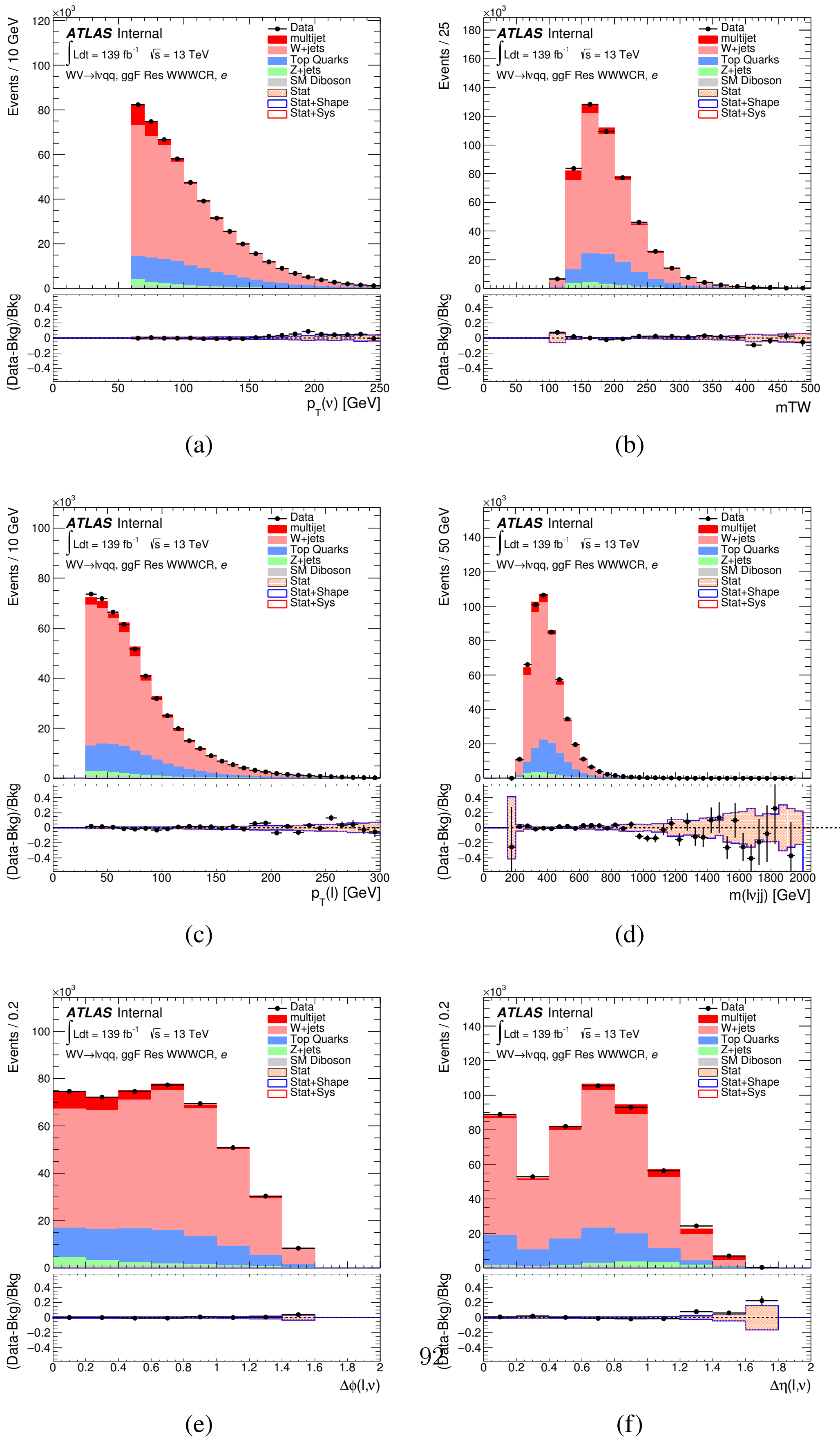

Figure 7.13: Postfit Data/MC comparison of distributions of E_T^{miss}, m_T^W, lepton

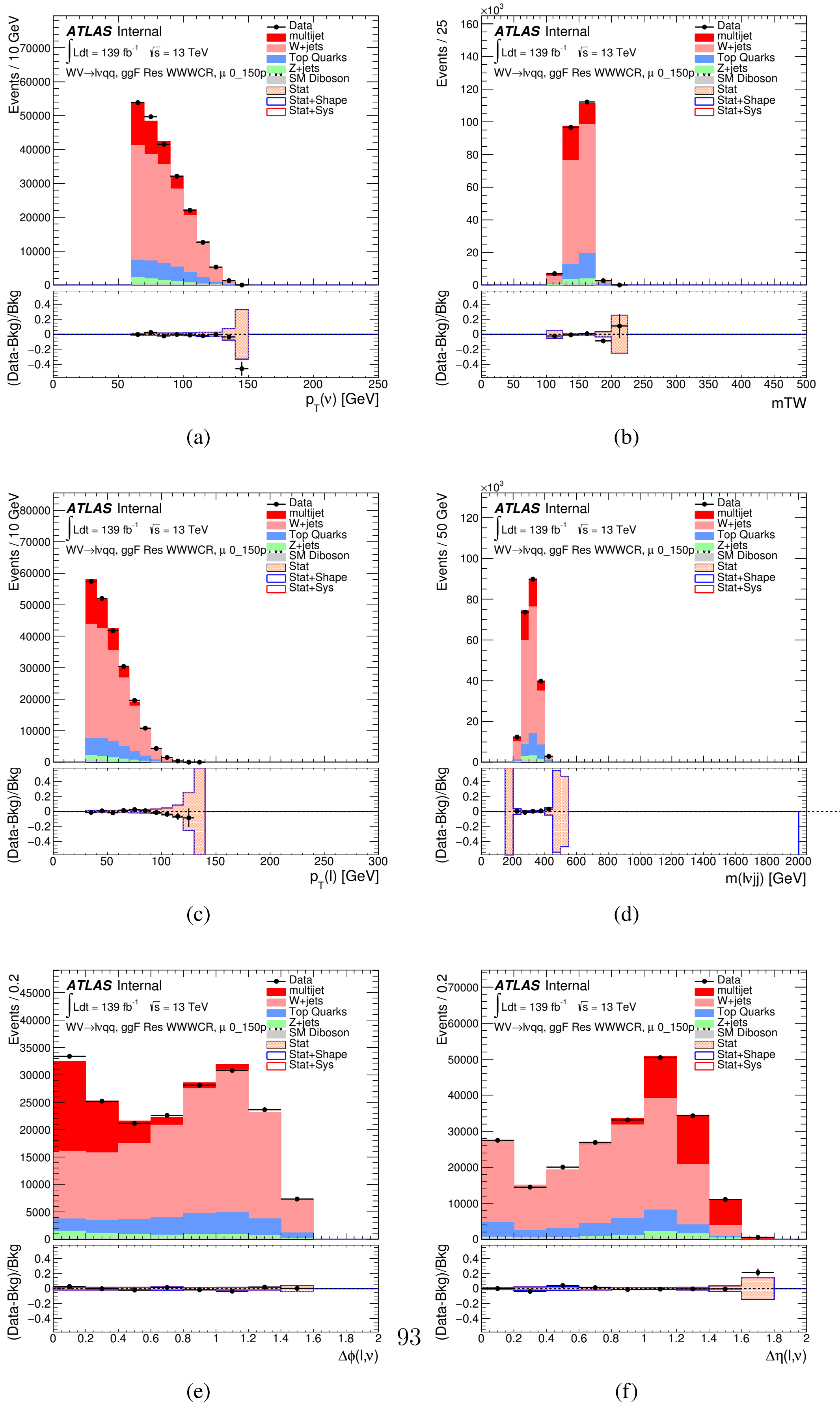

Figure 7.14: Postfit Data/MC comparison of distributions of E_T^{miss}, m_T^W, lepton and neutrino p_T, $m_{\ell\nu jj}$, lepton-ν angular distance in the WW muon channel. The

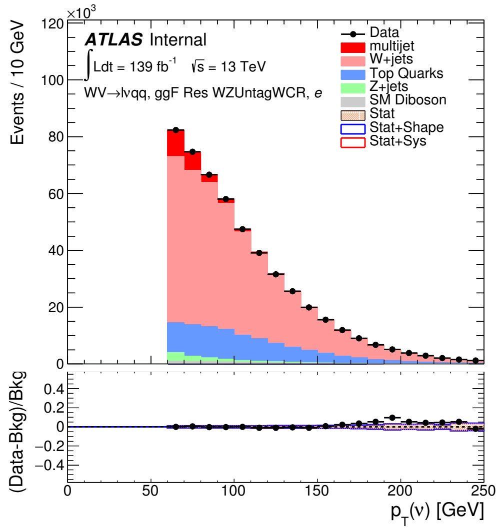
ATLAS Internal
∫Ldt = 139 fb⁻¹ √s = 13 TeV
WV→lνqq, ggF Res WZUntagWCR, e
Data
multijet
W+jets
Top Quarks
Z+jets
SM Diboson
Stat
Stat+Shape
Stat+Sys
Events / 10 GeV
×10³
(Data-Bkg)/Bkg
p_T(ν) [GeV]

(a)

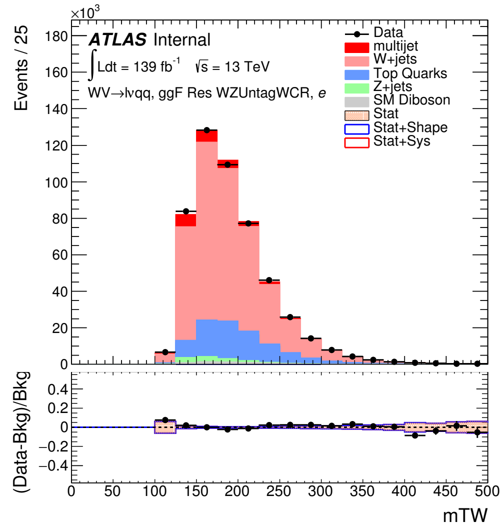
ATLAS Internal
∫Ldt = 139 fb⁻¹ √s = 13 TeV
WV→lνqq, ggF Res WZUntagWCR, e
Data
multijet
W+jets
Top Quarks
Z+jets
SM Diboson
Stat
Stat+Shape
Stat+Sys
Events / 25
×10³
(Data-Bkg)/Bkg
mTW

(b)

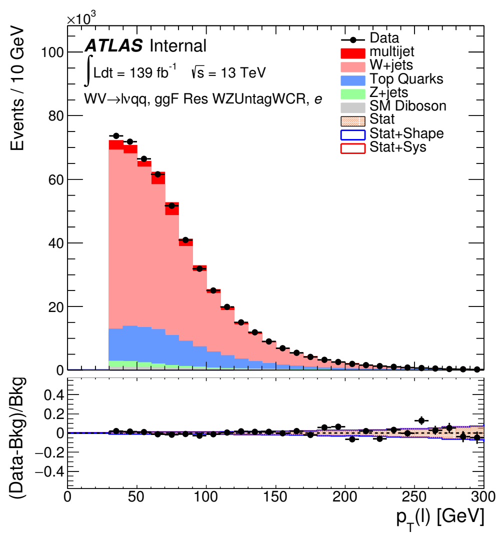
ATLAS Internal
∫Ldt = 139 fb⁻¹ √s = 13 TeV
WV→lνqq, ggF Res WZUntagWCR, e
Data
multijet
W+jets
Top Quarks
Z+jets
SM Diboson
Stat
Stat+Shape
Stat+Sys
Events / 10 GeV
×10³
(Data-Bkg)/Bkg
p_T(l) [GeV]

(c)

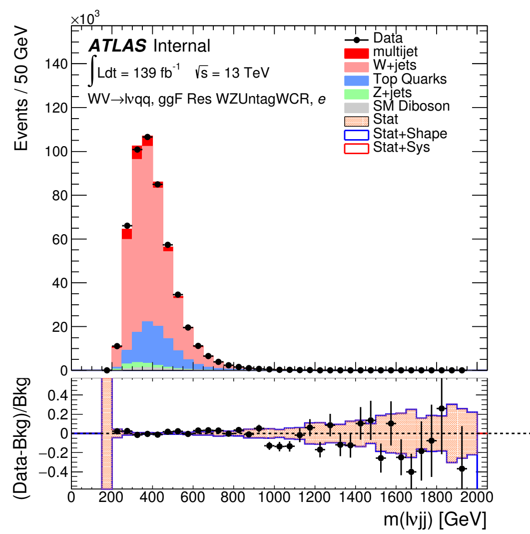
ATLAS Internal
∫Ldt = 139 fb⁻¹ √s = 13 TeV
WV→lνqq, ggF Res WZUntagWCR, e
Data
multijet
W+jets
Top Quarks
Z+jets
SM Diboson
Stat
Stat+Shape
Stat+Sys
Events / 50 GeV
×10³
(Data-Bkg)/Bkg
m(lνjj) [GeV]

(d)

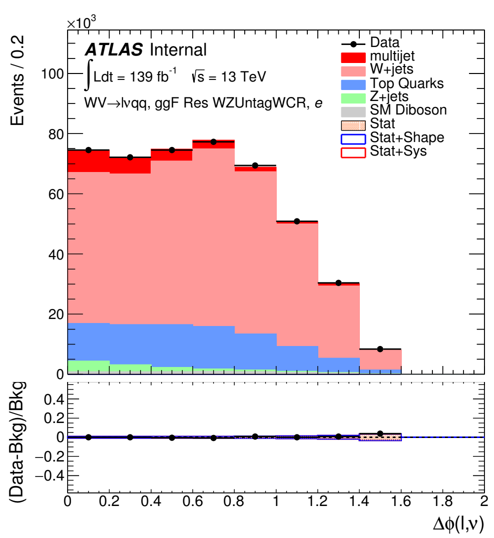
ATLAS Internal
∫Ldt = 139 fb⁻¹ √s = 13 TeV
WV→lνqq, ggF Res WZUntagWCR, e
Data
multijet
W+jets
Top Quarks
Z+jets
SM Diboson
Stat
Stat+Shape
Stat+Sys
Events / 0.2
×10³
(Data-Bkg)/Bkg
Δφ(l,ν)

(e)

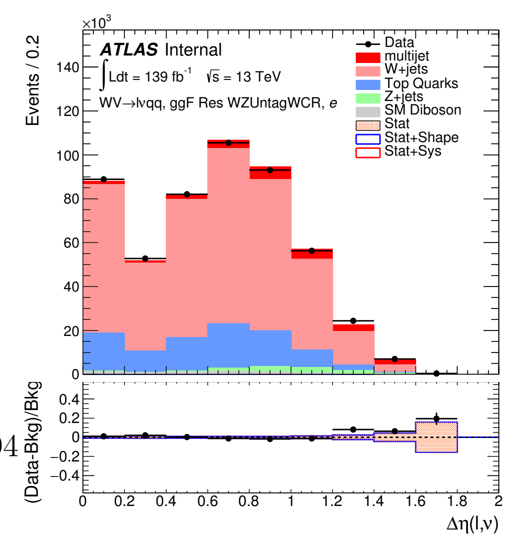
ATLAS Internal
∫Ldt = 139 fb⁻¹ √s = 13 TeV
WV→lνqq, ggF Res WZUntagWCR, e
Data
multijet
W+jets
Top Quarks
Z+jets
SM Diboson
Stat
Stat+Shape
Stat+Sys
Events / 0.2
×10³
(Data-Bkg)/Bkg
Δη(l,ν)

(f)

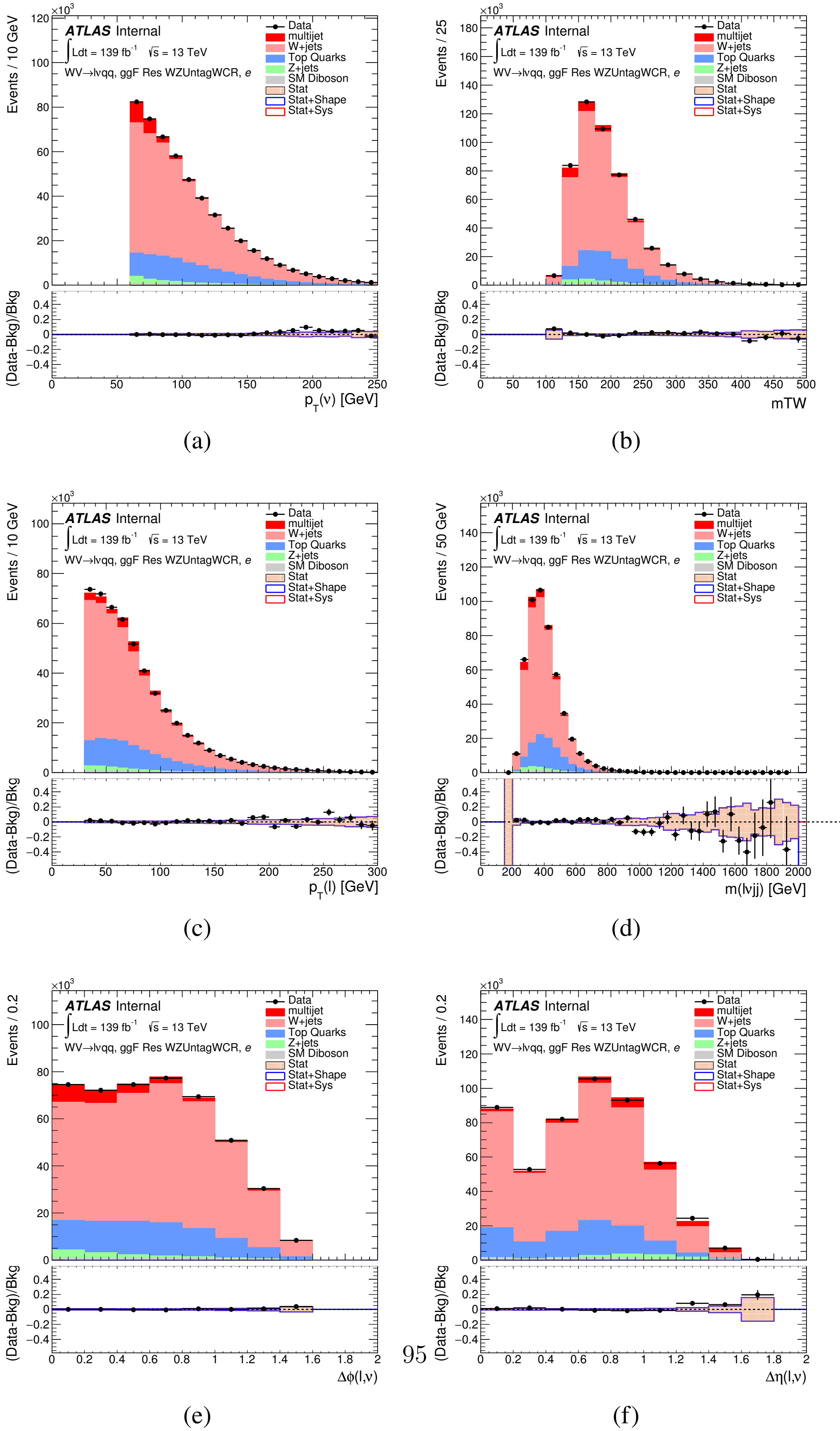

Figure 7.16: Postfit Data/MC comparison of distributions of E_T^{miss}, m_T^W, lepton

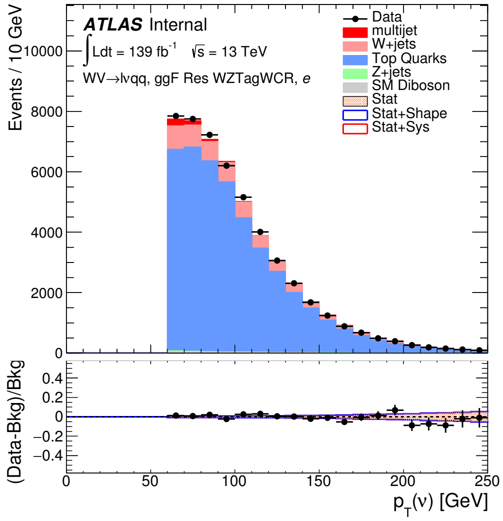
ATLAS Internal
∫Ldt = 139 fb⁻¹ √s = 13 TeV
WV→lνqq, ggF Res WZTagWCR, e
Data
multijet
W+jets
Top Quarks
Z+jets
SM Diboson
Stat
Stat+Shape
Stat+Sys
Events / 10 GeV
(Data-Bkg)/Bkg
$p_T(\nu)$ [GeV]

(a)

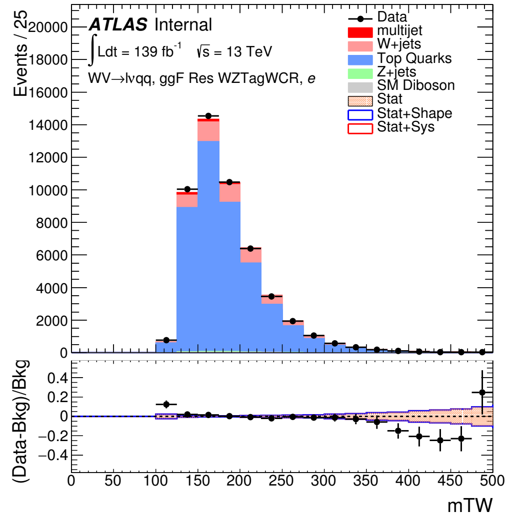
ATLAS Internal
∫Ldt = 139 fb⁻¹ √s = 13 TeV
WV→lνqq, ggF Res WZTagWCR, e
Data
multijet
W+jets
Top Quarks
Z+jets
SM Diboson
Stat
Stat+Shape
Stat+Sys
Events / 25
(Data-Bkg)/Bkg
mTW

(b)

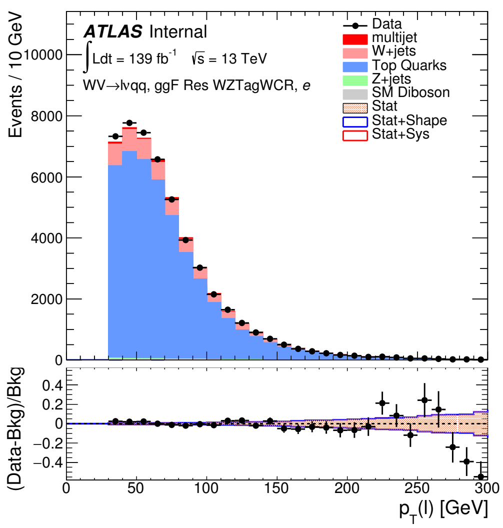
ATLAS Internal
∫Ldt = 139 fb⁻¹ √s = 13 TeV
WV→lνqq, ggF Res WZTagWCR, e
Data
multijet
W+jets
Top Quarks
Z+jets
SM Diboson
Stat
Stat+Shape
Stat+Sys
Events / 10 GeV
(Data-Bkg)/Bkg
$p_T(l)$ [GeV]

(c)

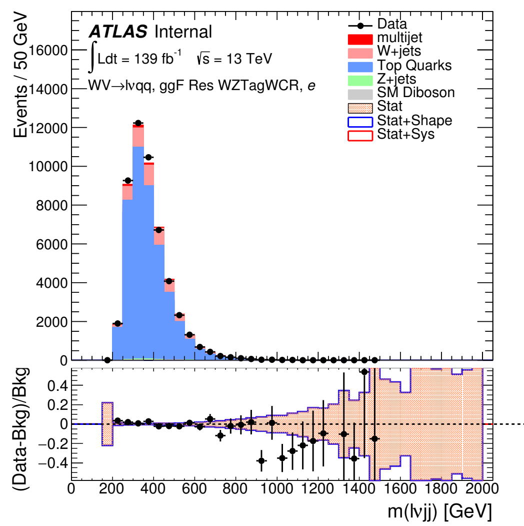
ATLAS Internal
∫Ldt = 139 fb⁻¹ √s = 13 TeV
WV→lνqq, ggF Res WZTagWCR, e
Data
multijet
W+jets
Top Quarks
Z+jets
SM Diboson
Stat
Stat+Shape
Stat+Sys
Events / 50 GeV
(Data-Bkg)/Bkg
m(lνjj) [GeV]

(d)

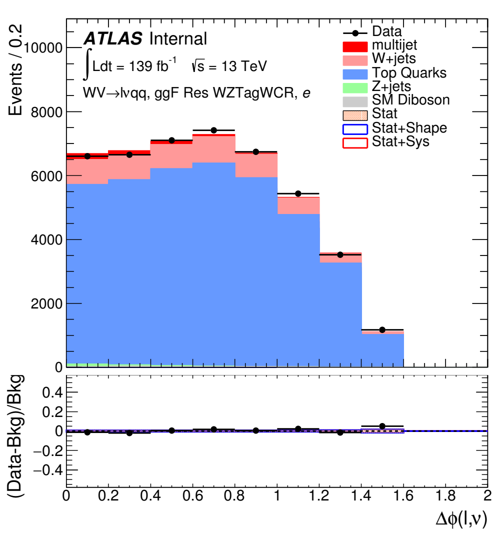
ATLAS Internal
∫Ldt = 139 fb⁻¹ √s = 13 TeV
WV→lνqq, ggF Res WZTagWCR, e
Data
multijet
W+jets
Top Quarks
Z+jets
SM Diboson
Stat
Stat+Shape
Stat+Sys
Events / 0.2
(Data-Bkg)/Bkg
Δφ(l,ν)

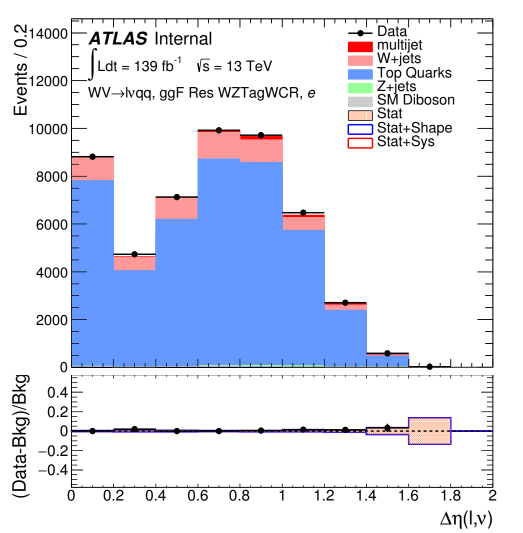
ATLAS Internal
∫Ldt = 139 fb⁻¹ √s = 13 TeV
WV→lνqq, ggF Res WZTagWCR, e
Data
multijet
W+jets
Top Quarks
Z+jets
SM Diboson
Stat
Stat+Shape
Stat+Sys
Events / 0.2
(Data-Bkg)/Bkg
Δη(l,ν)

(e)

(f)

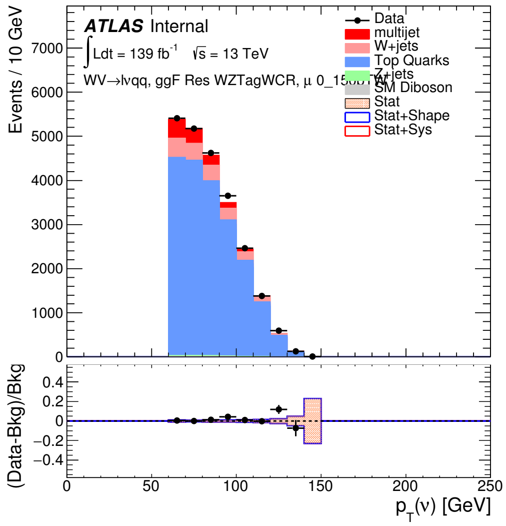
ATLAS Internal
∫Ldt = 139 fb⁻¹ √s = 13 TeV
WV→lvqq, ggF Res WZTagWCR
Data
multijet
W+jets
Top Quarks
Z+jets
SM Diboson
Stat
Stat+Shape
Stat+Sys
Events / 10 GeV
(Data-Bkg)/Bkg
p_T(ν) [GeV]

(a)

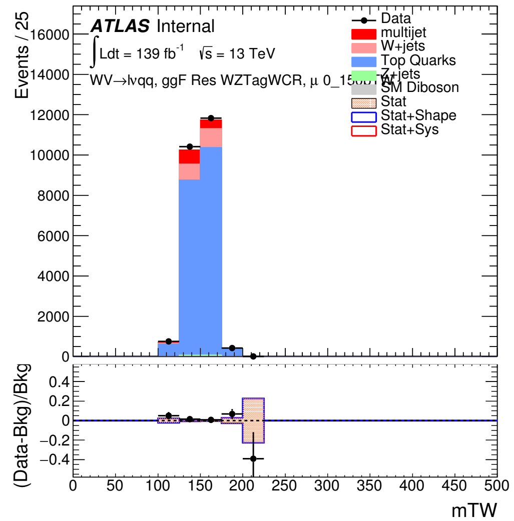
ATLAS Internal
∫Ldt = 139 fb⁻¹ √s = 13 TeV
WV→lvqq, ggF Res WZTagWCR
Data
multijet
W+jets
Top Quarks
Z+jets
SM Diboson
Stat
Stat+Shape
Stat+Sys
Events / 25
(Data-Bkg)/Bkg
mTW

(b)

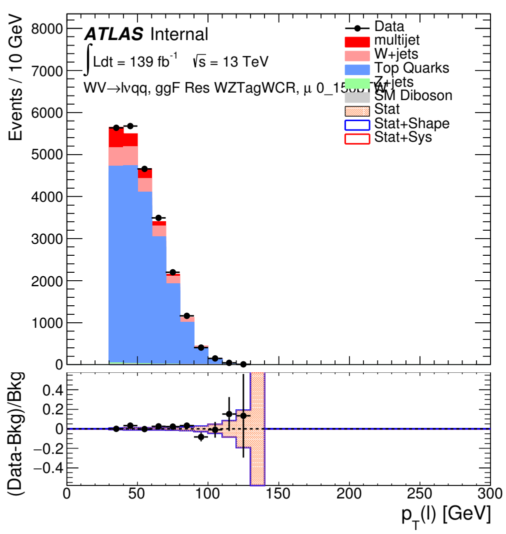
ATLAS Internal
∫Ldt = 139 fb⁻¹ √s = 13 TeV
WV→lvqq, ggF Res WZTagWCR
Data
multijet
W+jets
Top Quarks
Z+jets
SM Diboson
Stat
Stat+Shape
Stat+Sys
Events / 10 GeV
(Data-Bkg)/Bkg
p_T(l) [GeV]

(c)

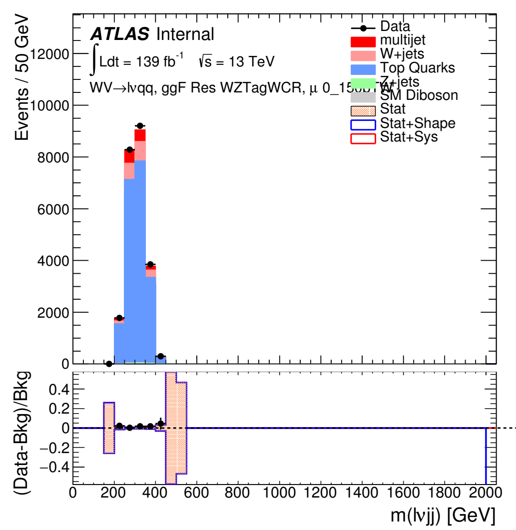
ATLAS Internal
∫Ldt = 139 fb⁻¹ √s = 13 TeV
WV→lvqq, ggF Res WZTagWCR
Data
multijet
W+jets
Top Quarks
Z+jets
SM Diboson
Stat
Stat+Shape
Stat+Sys
Events / 50 GeV
(Data-Bkg)/Bkg
m(lvjj) [GeV]

(d)

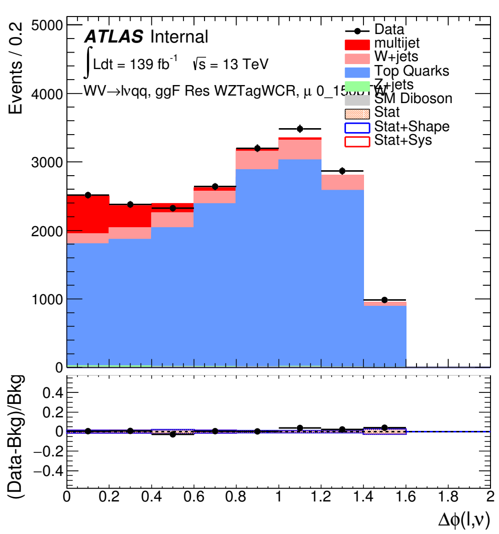
ATLAS Internal
∫Ldt = 139 fb⁻¹ √s = 13 TeV
WV→lvqq, ggF Res WZTagWCR
Data
multijet
W+jets
Top Quarks
Z+jets
SM Diboson
Stat
Stat+Shape
Stat+Sys
Events / 0.2
(Data-Bkg)/Bkg
Δφ(l,ν)

(e)

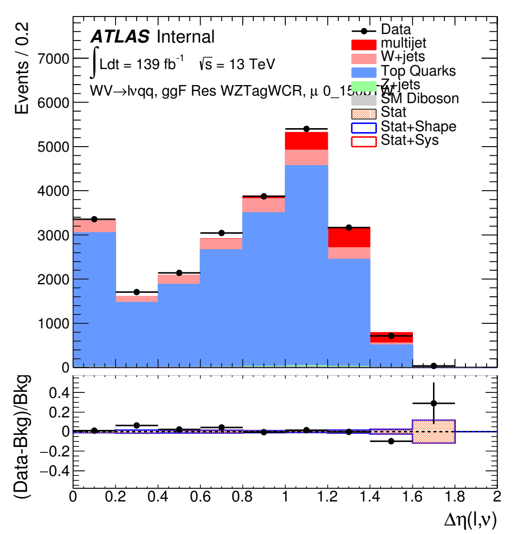
ATLAS Internal
∫Ldt = 139 fb⁻¹ √s = 13 TeV
WV→lvqq, ggF Res WZTagWCR
Data
multijet
W+jets
Top Quarks
Z+jets
SM Diboson
Stat
Stat+Shape
Stat+Sys
Events / 0.2
(Data-Bkg)/Bkg
Δη(l,ν)

(f)

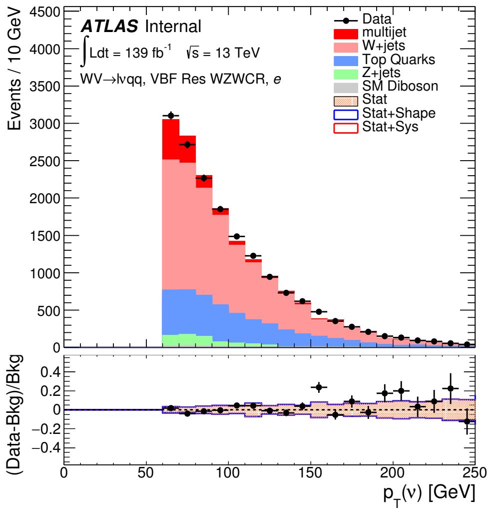
ATLAS Internal
∫Ldt = 139 fb⁻¹ √s = 13 TeV
WV→lνqq, VBF Res WZWCR, e
Data
multijet
W+jets
Top Quarks
Z+jets
SM Diboson
Stat
Stat+Shape
Stat+Sys
Events / 10 GeV
(Data-Bkg)/Bkg
p_T(ν) [GeV]

(a)

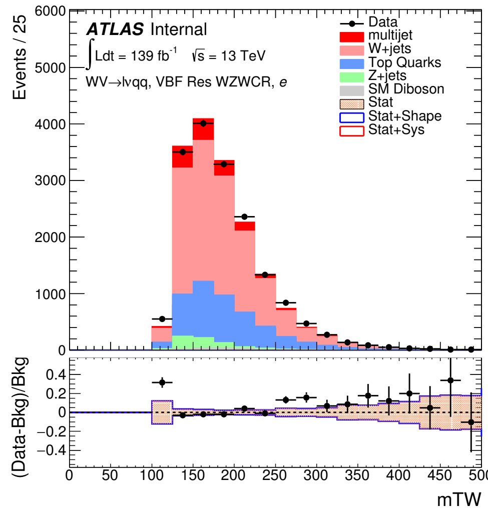
ATLAS Internal
∫Ldt = 139 fb⁻¹ √s = 13 TeV
WV→lνqq, VBF Res WZWCR, e
Data
multijet
W+jets
Top Quarks
Z+jets
SM Diboson
Stat
Stat+Shape
Stat+Sys
Events / 25
(Data-Bkg)/Bkg
mTW

(b)

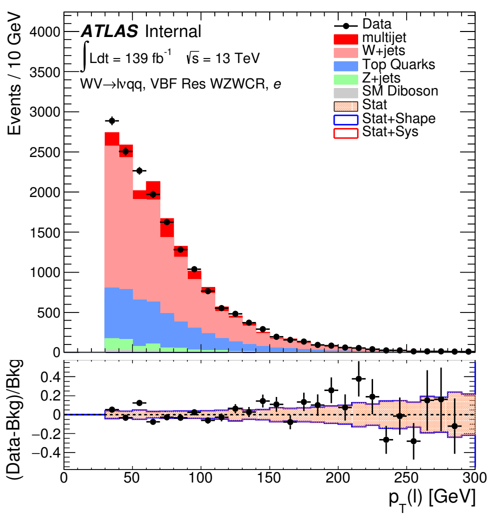
ATLAS Internal
∫Ldt = 139 fb⁻¹ √s = 13 TeV
WV→lνqq, VBF Res WZWCR, e
Data
multijet
W+jets
Top Quarks
Z+jets
SM Diboson
Stat
Stat+Shape
Stat+Sys
Events / 10 GeV
(Data-Bkg)/Bkg
p_T(l) [GeV]

(c)

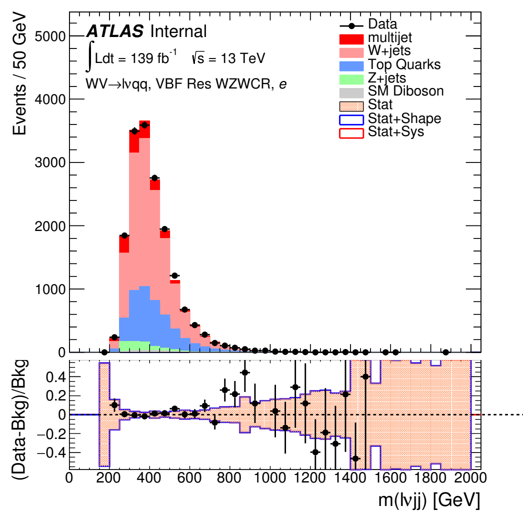
ATLAS Internal
∫Ldt = 139 fb⁻¹ √s = 13 TeV
WV→lνqq, VBF Res WZWCR, e
Data
multijet
W+jets
Top Quarks
Z+jets
SM Diboson
Stat
Stat+Shape
Stat+Sys
Events / 50 GeV
(Data-Bkg)/Bkg
m(lνjj) [GeV]

(d)

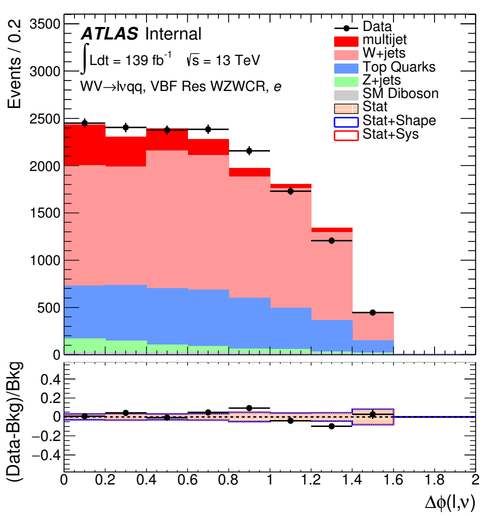
ATLAS Internal
∫Ldt = 139 fb⁻¹ √s = 13 TeV
WV→lνqq, VBF Res WZWCR, e
Data
multijet
W+jets
Top Quarks
Z+jets
SM Diboson
Stat
Stat+Shape
Stat+Sys
Events / 0.2
(Data-Bkg)/Bkg
Δφ(l,ν)

(e)

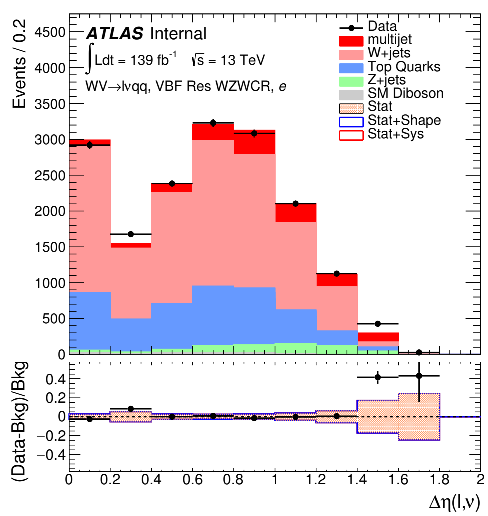
ATLAS Internal
∫Ldt = 139 fb⁻¹ √s = 13 TeV
WV→lνqq, VBF Res WZWCR, e
Data
multijet
W+jets
Top Quarks
Z+jets
SM Diboson
Stat
Stat+Shape
Stat+Sys
Events / 0.2
(Data-Bkg)/Bkg
Δη(l,ν)

(f)

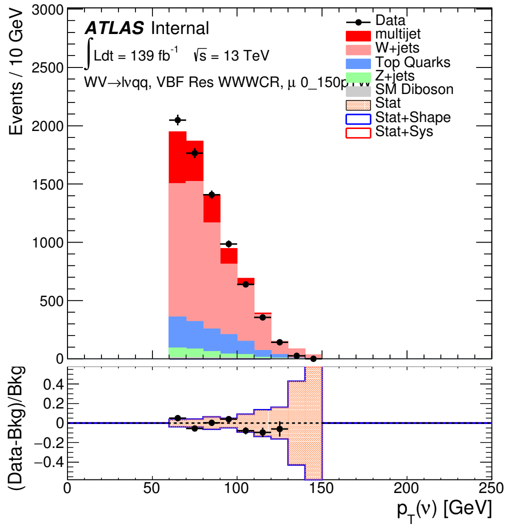
ATLAS Internal
∫Ldt = 139 fb⁻¹ √s = 13 TeV
WV→lνqq, VBF Res WWWCR, μ 0_150p
Data
multijet
W+jets
Top Quarks
Z+jets
SM Diboson
Stat
Stat+Shape
Stat+Sys
Events / 10 GeV
(Data-Bkg)/Bkg
p_T(ν) [GeV]

(a)

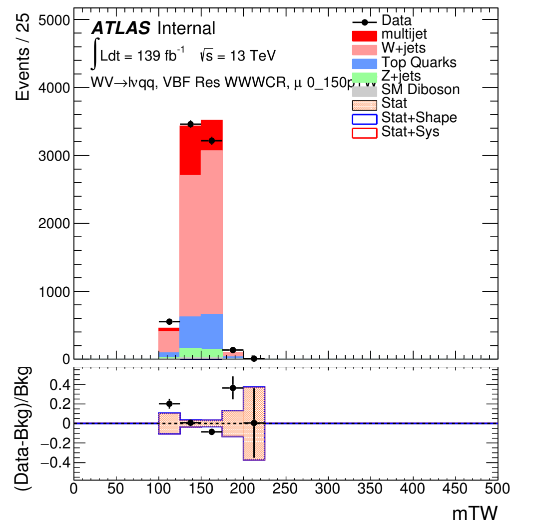
ATLAS Internal
∫Ldt = 139 fb⁻¹ √s = 13 TeV
WV→lνqq, VBF Res WWWCR, μ 0_150p
Data
multijet
W+jets
Top Quarks
Z+jets
SM Diboson
Stat
Stat+Shape
Stat+Sys
Events / 25
(Data-Bkg)/Bkg
mTW

(b)

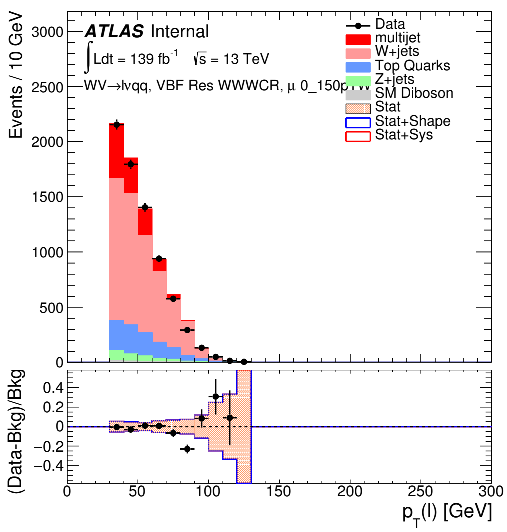
ATLAS Internal
∫Ldt = 139 fb⁻¹ √s = 13 TeV
WV→lνqq, VBF Res WWWCR, μ 0_150p
Data
multijet
W+jets
Top Quarks
Z+jets
SM Diboson
Stat
Stat+Shape
Stat+Sys
Events / 10 GeV
(Data-Bkg)/Bkg
p_T(l) [GeV]

(c)

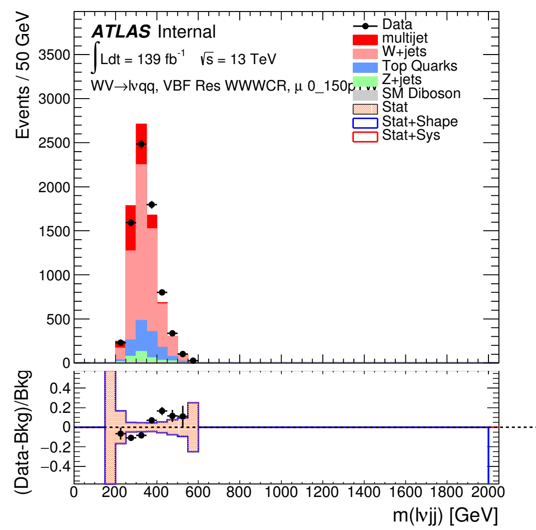
ATLAS Internal
∫Ldt = 139 fb⁻¹ √s = 13 TeV
WV→lνqq, VBF Res WWWCR, μ 0_150p
Data
multijet
W+jets
Top Quarks
Z+jets
SM Diboson
Stat
Stat+Shape
Stat+Sys
Events / 50 GeV
(Data-Bkg)/Bkg
m(lνjj) [GeV]

(d)

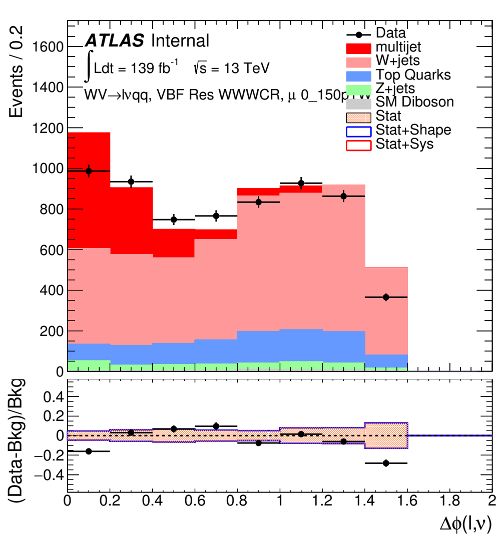
ATLAS Internal
∫Ldt = 139 fb⁻¹ √s = 13 TeV
WV→lνqq, VBF Res WWWCR, μ 0_150p
Data
multijet
W+jets
Top Quarks
Z+jets
SM Diboson
Stat
Stat+Shape
Stat+Sys
Events / 0.2
(Data-Bkg)/Bkg
Δφ(l,ν)

(e)

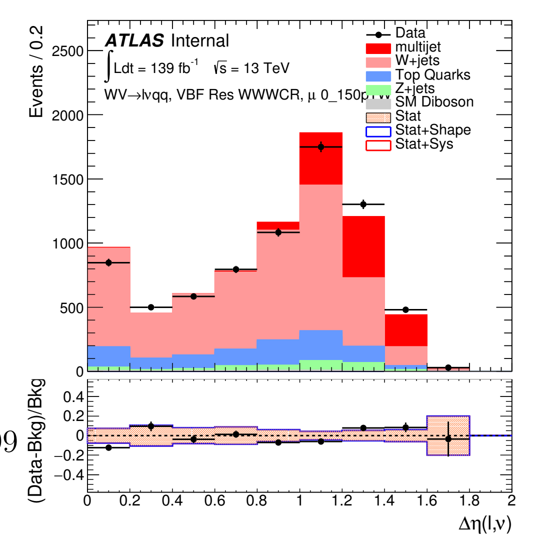
ATLAS Internal
∫Ldt = 139 fb⁻¹ √s = 13 TeV
WV→lνqq, VBF Res WWWCR, μ 0_150p
Data
multijet
W+jets
Top Quarks
Z+jets
SM Diboson
Stat
Stat+Shape
Stat+Sys
Events / 0.2
(Data-Bkg)/Bkg
Δη(l,ν)

(f)

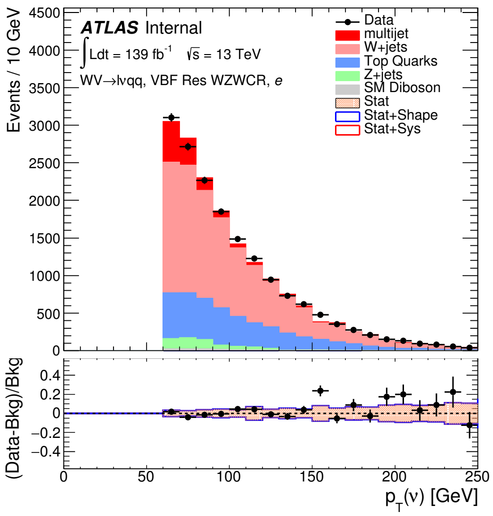
ATLAS Internal
∫Ldt = 139 fb⁻¹ √s = 13 TeV
WV→lvqq, VBF Res WZWCR, e
Data
multijet
W+jets
Top Quarks
Z+jets
SM Diboson
Stat
Stat+Shape
Stat+Sys
Events / 10 GeV
(Data-Bkg)/Bkg
p_T(ν) [GeV]

(a)

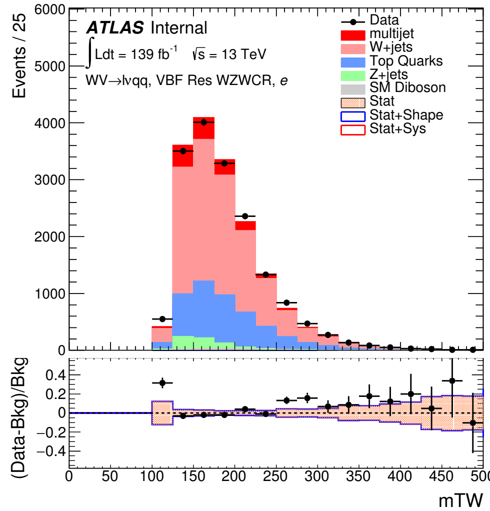
ATLAS Internal
∫Ldt = 139 fb⁻¹ √s = 13 TeV
WV→lvqq, VBF Res WZWCR, e
Data
multijet
W+jets
Top Quarks
Z+jets
SM Diboson
Stat
Stat+Shape
Stat+Sys
Events / 25
(Data-Bkg)/Bkg
mTW

(b)

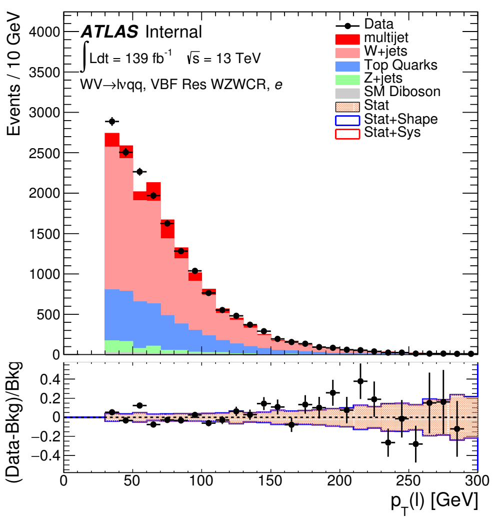
ATLAS Internal
∫Ldt = 139 fb⁻¹ √s = 13 TeV
WV→lvqq, VBF Res WZWCR, e
Data
multijet
W+jets
Top Quarks
Z+jets
SM Diboson
Stat
Stat+Shape
Stat+Sys
Events / 10 GeV
(Data-Bkg)/Bkg
p_T(l) [GeV]

(c)

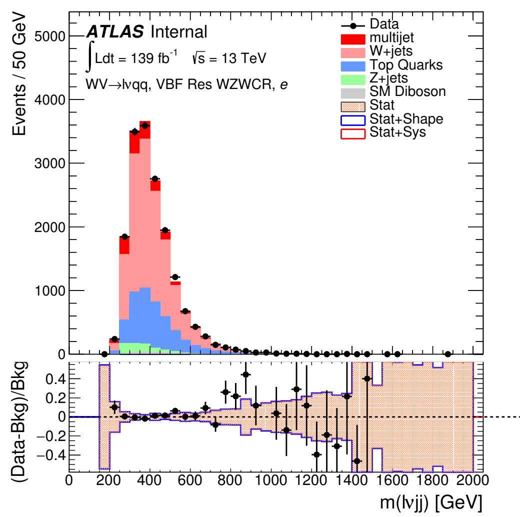
ATLAS Internal
∫Ldt = 139 fb⁻¹ √s = 13 TeV
WV→lvqq, VBF Res WZWCR, e
Data
multijet
W+jets
Top Quarks
Z+jets
SM Diboson
Stat
Stat+Shape
Stat+Sys
Events / 50 GeV
(Data-Bkg)/Bkg
m(lvjj) [GeV]

(d)

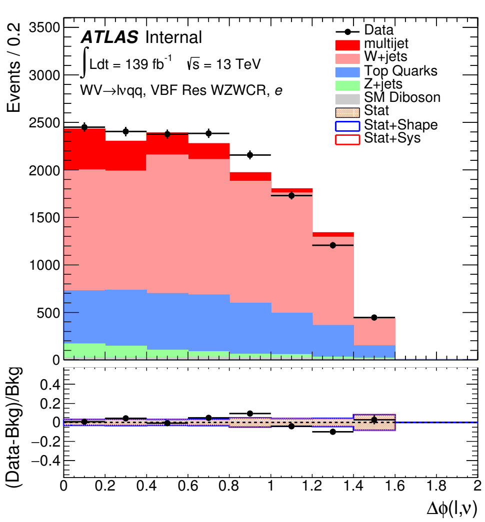
ATLAS Internal
∫Ldt = 139 fb⁻¹ √s = 13 TeV
WV→lvqq, VBF Res WZWCR, e
Data
multijet
W+jets
Top Quarks
Z+jets
SM Diboson
Stat
Stat+Shape
Stat+Sys
Events / 0.2
(Data-Bkg)/Bkg
Δφ(l,ν)

(e)

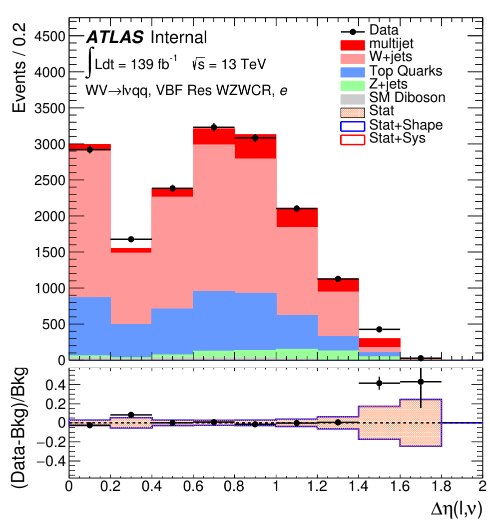
ATLAS Internal
∫Ldt = 139 fb⁻¹ √s = 13 TeV
WV→lvqq, VBF Res WZWCR, e
Data
multijet
W+jets
Top Quarks
Z+jets
SM Diboson
Stat
Stat+Shape
Stat+Sys
Events / 0.2
(Data-Bkg)/Bkg
Δη(l,ν)

(f)

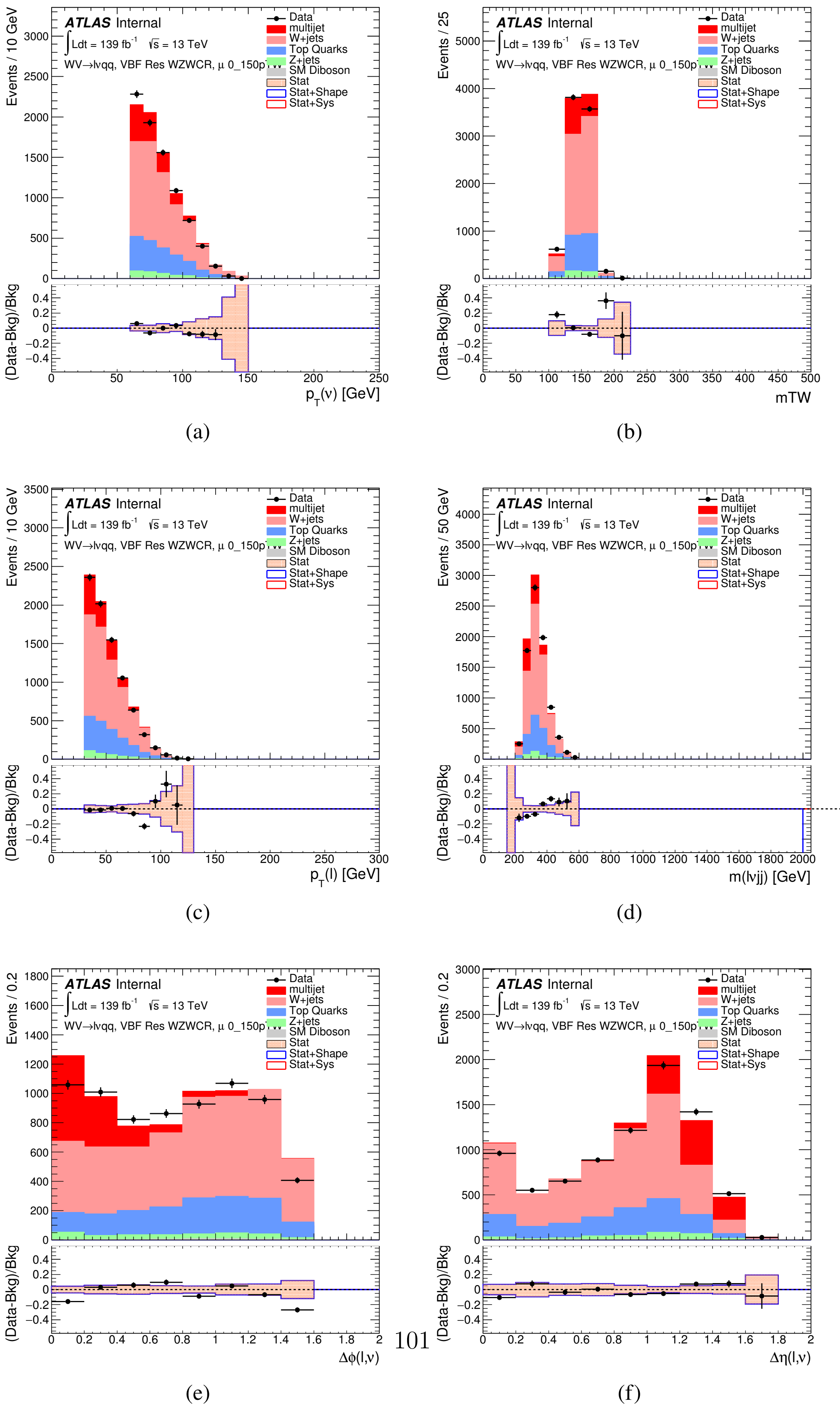

Figure 7.22: Postfit Data/MC comparison of distributions of E_T^{miss}, m_T^W, lepton

Full Run 2

ggF Res WWWCR

Sample	Yield	R.U.	SF
Top&W	645040 ± 1971.68	0.31%	0.998
Z&VV	24075.9	fixed	
MJ_el	24156.3 ± 1224.62	5.06%	3.973
MJ_mu	35528.5 ± 923.94	2.60%	9.019

ggF Res WZ01bWCR

Sample	Yield	R.U.	SF
Top&W	644690 ± 1981.4	0.31%	0.997
Z&VV	24075.9	fixed	
MJ_el	24366.5 ± 1232.69	5.05%	3.874
MJ_mu	35528.5 ± 921.27	2.58%	8.746

ggF Res WZ2bWCR

Sample	Yield	R.U.	SF
Top&W	71236.5 ± 688.74	0.97%	1.031
Z&VV	518.5	fixed	
MJ_el	595.63 ± 449.34	75.44%	0.094
MJ_mu	1196.9 ± 222.13	18.56%	0.294

VBF Res WWWCR

Sample	Yield	R.U.	SF
Top&W	19032.3 ± 364.43	1.91%	0.928
Z&VV	1091.63	fixed	
MJ_el	1425.73 ± 214.42	15.03%	0.235
MJ_mu	1281.36 ± 157.21	11.83%	0.314

VBF Res WZWCR

Sample	Yield	R.U.	SF
Top&W	21341.8 ± 392.21	1.84%	0.942
Z&VV	1111.75	fixed	
MJ_el	1413.76 ± 230.36	16.29%	0.225
MJ_mu	1281.36 ± 157.21	12.27%	0.314

Table 7.5: Fit validation result in WCRs for 2015+16 data. The fit is done in various WCRs, in order to obtain the corresponding scale factors for MJ templates: ggF resolved WCR for the $WW \to lvqq$ selection, ggF resolved untagged WCR for the $WZ \to lvqq$ selection, ggF resolved tagged WCR for the $WZ \to lvqq$ selection, VBF resolved WCR for the $WW \to lvqq$ selection,and VBF resolved WCR for the $WZ \to lvqq$ selection. Post-fit event yields for electroweak processes and MJ contributions are shown. The SF column shows the corresponding normalization scale factors for electroweak processes from the fit. R.U. stands for relative uncertainty.

Chapter 8

Systematic Uncertainties

This section describes the sources of systematic uncertainties considered in this analysis. These uncertainties are divided into three categories: experimental uncertainties, background modeling uncertainties, and theoretical uncertainties on signal processes. In the statistical analysis each systematic uncertainty is treated as a nuisance parameter estimated on the m_{VV} distribution.

8.1 Experimental Systematics

The uncertainty on the integrated luminosity of the dataset used is 1.7% and a systematic in the final fit. The luminosity uncertainty is calculated following a methodology similar to the one in [ref P55].

Also, multiple pile up interactions are simulated to match data conditions. This ensures simulated detector response and particle reconstruction conditions are as similar as possible. The distribution of the average number of interactions per bunch crossing applied to simulation is called the μ profile. The pileup modeling uncertainty is accounted for by re-weighting simulated events so the average number of interactions per bunch crossing varies within its uncertainty due to systematics from vertex reconstruction [ref ATL-COM-SOFT-2015-119]. The associated re-weighting factors are propagated through the entire analysis chain to construct a systematic uncertainty on m_{VV}.

The single-lepton and E_T^{miss} triggers used are not fully efficient and therefore simulated data must be scaled to account for trigger inefficiencies. Trigger efficiences are given by the ratio of the distribution of offline objects before trigger selection and after trigger selection.

Uncertainties on small-R jet energy scale and resolution are measured in-situ by calculating the response between data and simulation. This analysis uses a reduced set of JES and JER uncertainties (totaling 30 and 8 systematics, respectively). These reduced sets of systematics are calculated using a principal component analysis, yield largely uncorrelated independent systematics. These uncertainties account for the dependence on p_T, η, μ, flavor response and global sequential corrections. Systematic uncertainties associated with b-tagging are also considered. These systematics are evaluated as uncertainties on the scale factor which account for the difference in b-tagging efficiencies in data and MC, and the flavor dependence (between b, c, and light jets).

The uncertainty on the p_T scale of the large-R jets is determined by comparing the jet's p_T^{calo} to p_T^{track} in di-jet simulation and data. In addition to this uncertainties from tracking, modeling (Pythia vs Herwig), and statistical constraints are also calculated. The large-R jet p_T resolution is given by smearing the jet p_T with a Gaussian with a 2% width.

The W/Z-tagging efficiency cannot be evaluated using the Rtrk method as the TCC algorithm uses track measurements to reconstruct jet substructure variables. In order to avoid this potential bias, the W/Z-tagging estimated in data using a control sample and correct by comparing it with simulation. The efficiency to

W/Z-induced signal is estimated by a $t\bar{t}$ control sample, while the efficiency to single-q/g background is estimated using a dijet sample. The effects of experimental and theoretical uncertainties on the efficiency scale factor are by taking the ratio of efficiencies in data and simulation. By taking this ratio the uncertainties not arising for jet mass and D_2 cancel.

Lepton identification, reconstruction, isolation systematic uncertainties are determined by reconstructing the Z mass peak with a tag and probe method. The lepton energy and momentum scales are also measured with the Z mass peak. Additionally, the track-to-vertex association efficiency is used for muons.

As E_T^{miss} is calculated using all the physics objects in the event, all those objects associated errors result in an uncertainty on E_T^{miss}. Additionally, the unassociated tracks used to construct E_T^{miss} contribute to the uncertainty on E_T^{miss}.

8.2 Theory Systematics

Theoretical uncertainties for signal and background processes arise from uncertainties in the parameters used in Monte Carlo simulation. In particular for the $t\bar{t}$, W/Z+jets, and diboson backgrounds and signal samples the QCD scale, PDF, generator and hadronization uncertainties were evaluated. To assess the QCD scale uncertainty the renormalization and factorization scales were scaled up (2.0) and down (0.5) at the event generation stage of sample production. Uncertainties due to the choice of the parton distribution functions were evaluated by re-weighting samples from the nominal PDF to a set of error PDFs which account for the uncertainty of the fits used to produce the PDF set. In addition to this samples are re-weighted to different PDF sets to account for the arbitrariness of the PDF choice. The difference between the m_{WV} distributions using different event generators is assessed by comparing samples generated with different generators. Similarly, the uncertainty in hadronization models is account for by comparing samples created using different hadronization models (e.g. Pythia8 vs. Herwig7). Figures 8.2 - 8.8 show the impact of these uncertainties on the $t\bar{t}$ and W/Z + jets backgrounds.

Additionally, contributions to the diboson background for the VBF analysis were included in [SOME WAY that is not determined yet].

The normalization of the $t\bar{t}$ and W+jets processes impact the multijet template shape. The impact of these normalization is assess by including a shape systematic on the multijet background from varying the $t\bar{t}$ and W+jets normalization factors.

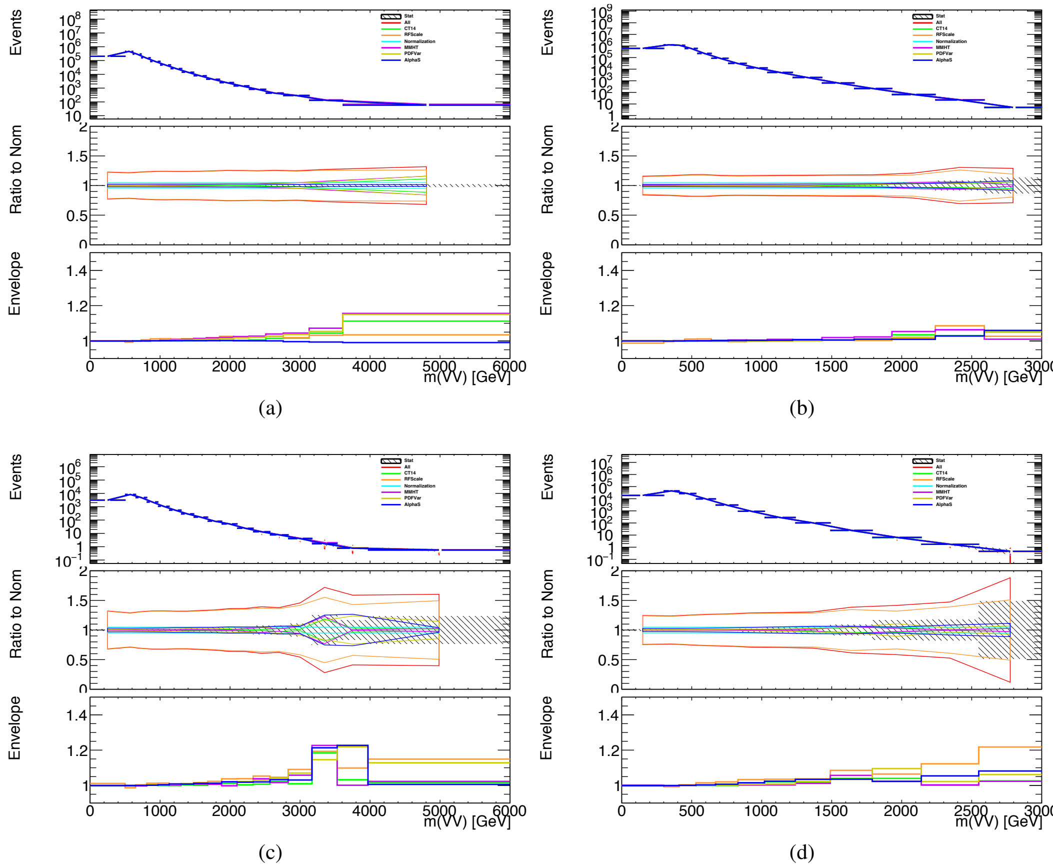

Figure 8.1: The W/Z+jet systematics for the a) Merged ggF, b) Resolved ggF, c) Merged VBF, and d) Resolved VBF regions. The top subplot shows the nominal and variation distributions/bands, the middle shows the ratio of the two, and the final shows just the shape of the envelope (the final uncertainty).

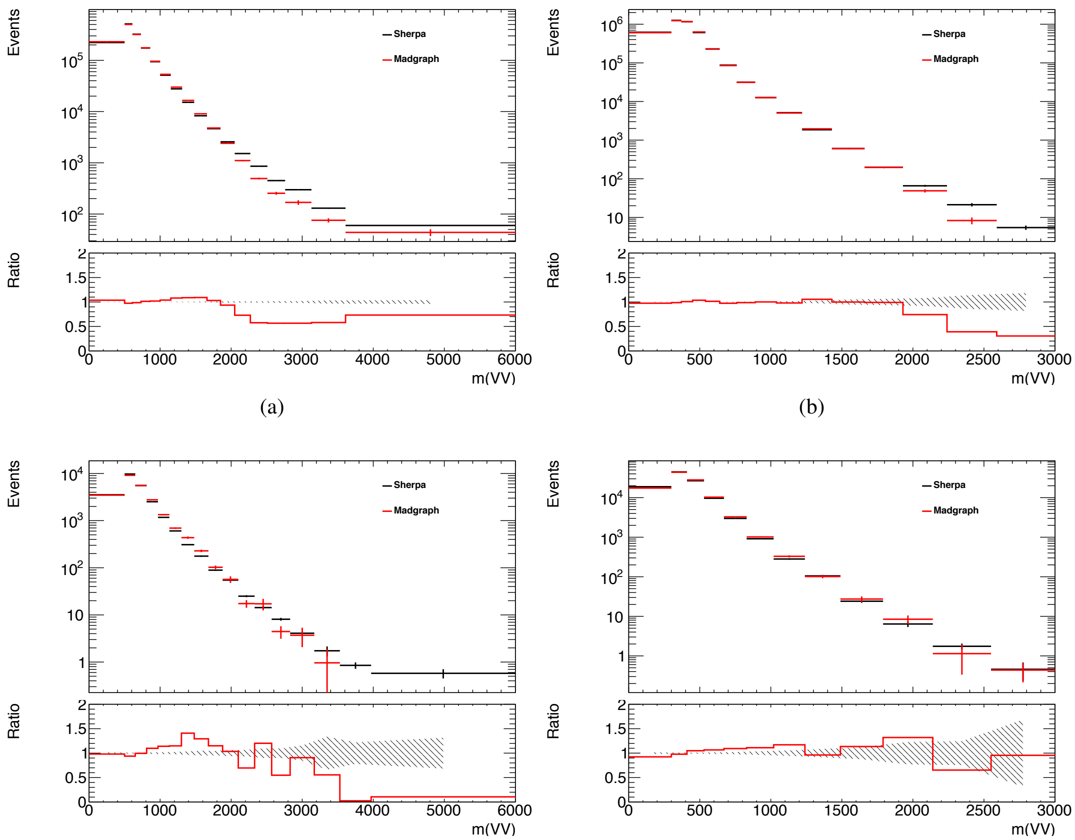

(a) (b) (c) (d)

Figure 8.2: The two-point generator comparison between Sherpa and MadGraph for the W/Z+jet samples in the a) Merged ggF, b) Resolved ggF, c) Merged VBF, and d) Resolved VBF regions. The normalization of the Madgraph sample is set to the Sherpa value to consider only shape effects. The bottom inlet shows the ratio of the two.

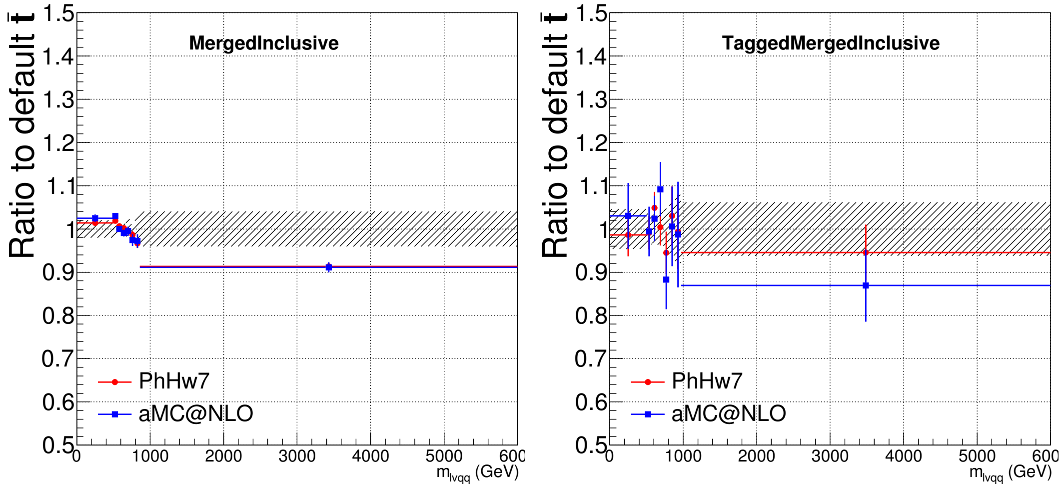

Figure 8.3: Ratio between the variations of generator (red) and hadronization (blue) variations for the Merged regime for $t\bar{t}$ sample.

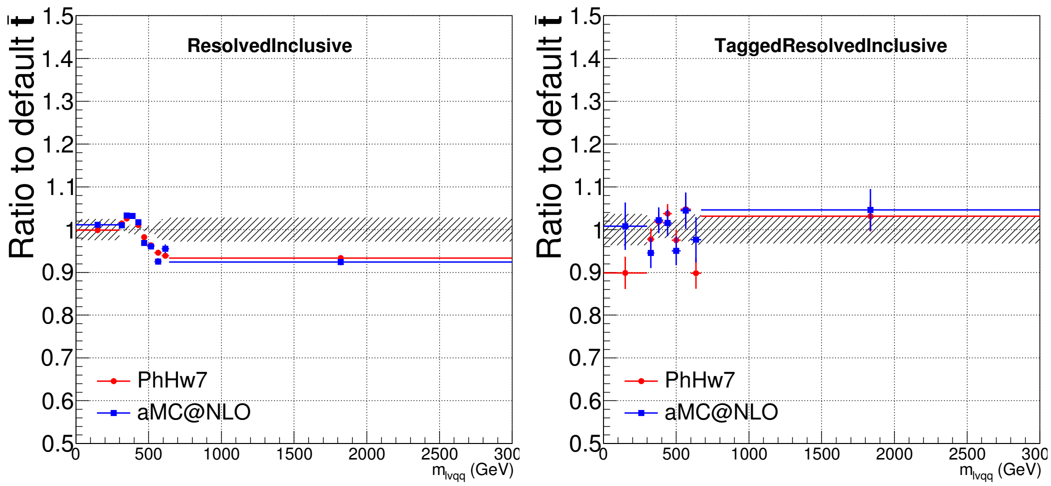

(a) ggF 1-lep

(b) VBF 1-lep

Figure 8.4: Ratio between the variations of generator (red) and hadronization (blue) variations for the Resolved regime for $t\bar{t}$ sample.

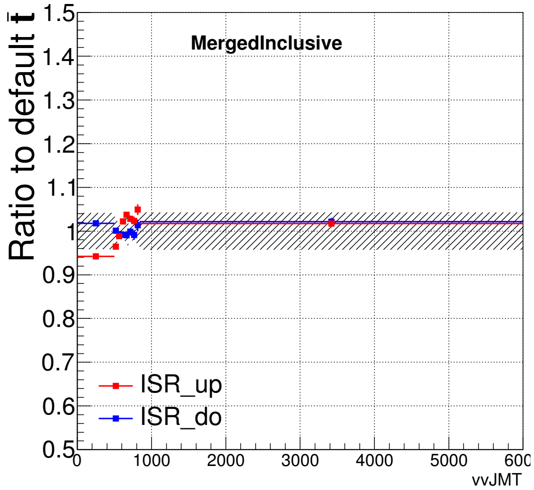

(a) ggF 0-lep

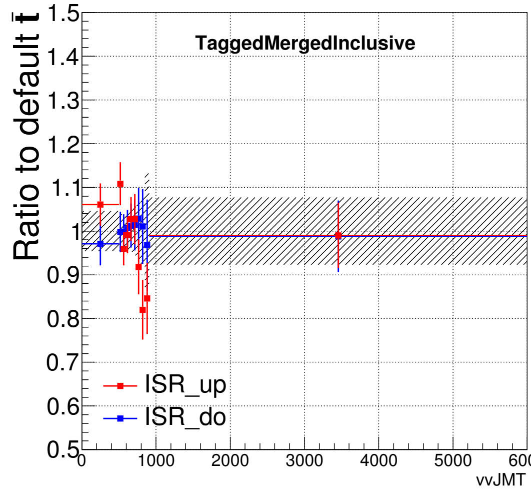

(b) VBF 0-lep

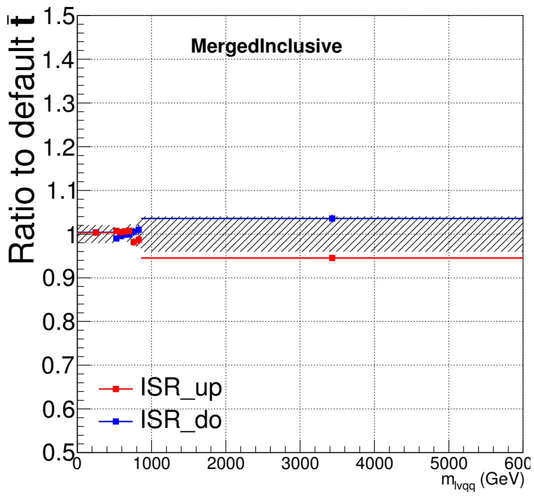

(c) ggF 1-lep

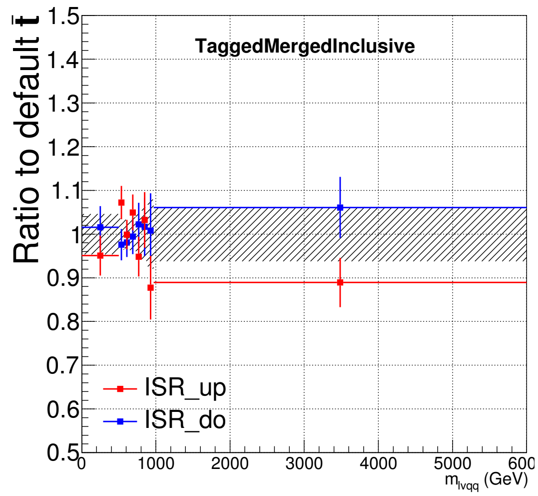

(d) VBF 1-lep

Figure 8.5: Ratio between the variations of ISR up (red) and down (blue) variations for the Merged regime for $t\bar{t}$ sample.

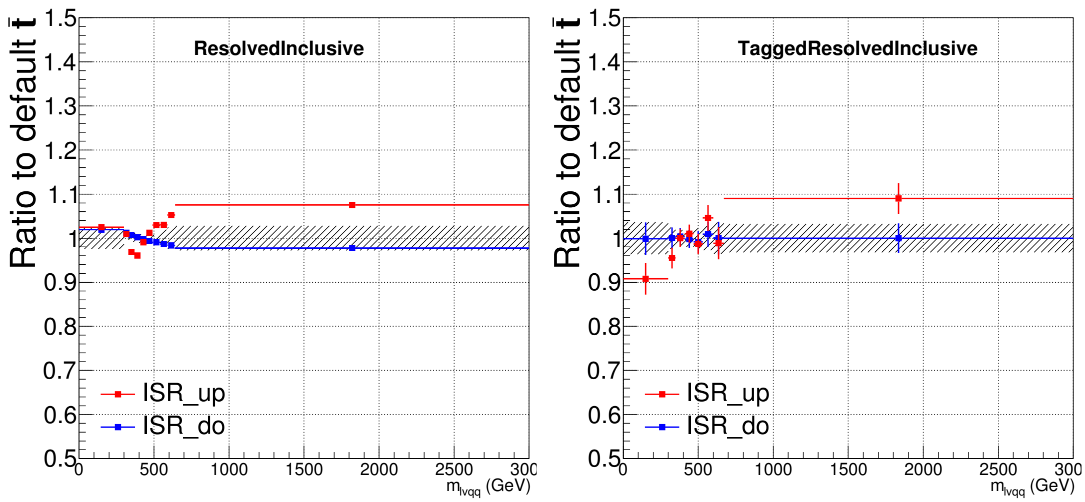

(a) ggF 1-lep

(b) VBF 1-lep

Figure 8.6: Ratio between the variations of ISR up (red) and down (blue) variations for the Resolved regime for $t\bar{t}$ sample.

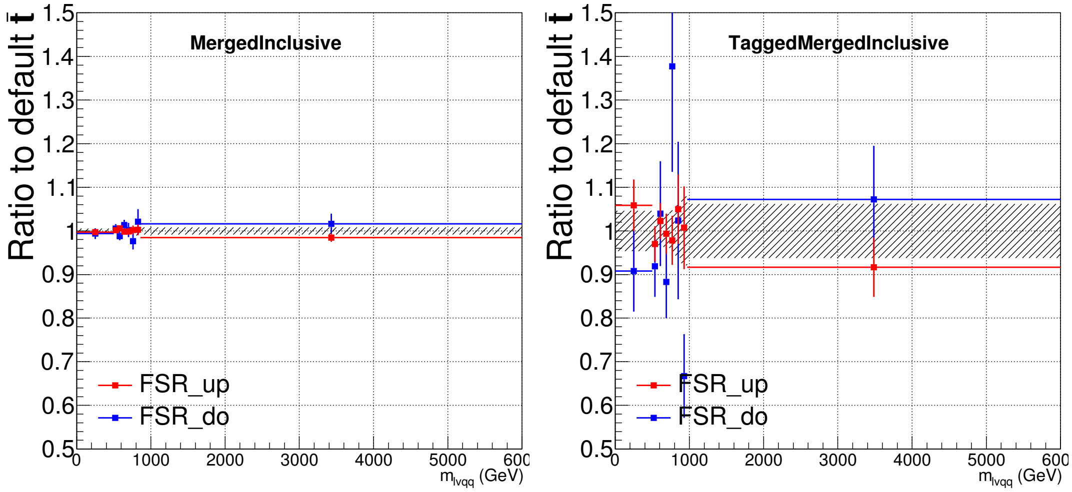

Figure 8.7: Ratio between the variations of FSR up (red) and down (blue) variations for the Merged regime for $t\bar{t}$ sample.

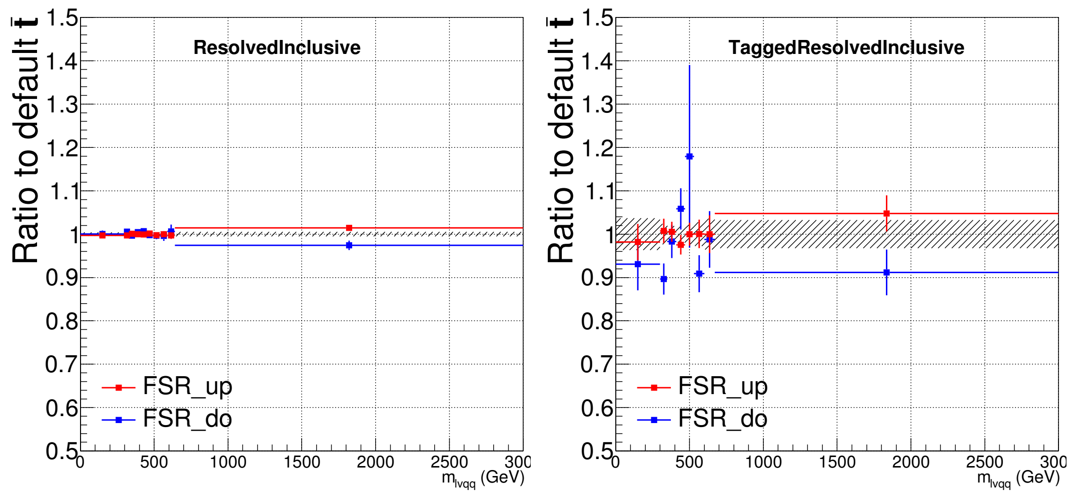

(a) ggF 1-lep

(b) VBF 1-lep

Figure 8.8: Ratio between the variations of FSR up (red) and down (blue) variations for the Resolved regime for $t\bar{t}$ sample.

Chapter 9

Statistical Analysis

To determine the compatibility of the data collected with the proposed resonances a statistical procedure based on a likelihood function is used. A discovery test is used to measure the compatibility of the observed data with the background only hypothesis. If the observed data is sufficiently incompatible with the background only hypothesis, this could indicate a discovery. In the absence of discovery, upper limits on the signal strength parameter, μ, are assessed using the CLs method.

9.1 Likelihood Function Definition

The likelihood function is product of Poisson probabilities for all analysis bins and systematic constraints:

$$\mathcal{L}(\mu, \boldsymbol{\theta}) = \prod_c \prod_i \frac{(\mu s_{ci}(\boldsymbol{\theta}) + b_{ci}(\boldsymbol{\theta}))^{n_{ci}}}{n_{ci}!} e^{-(\mu s_{ci}(\boldsymbol{\theta}) + b_{ci}(\boldsymbol{\theta}))} \prod_k (\theta'_k | \theta_k) \tag{9.1}$$

Here c are the analysis channels considered and i runs over all the $m_{\ell\nu qq}$ bins used in the fit. The signal strength parameter, μ, multiplies the expected signal yield in each analysis bin, s_{ci}. The background content for channel c and bin i is given by b_{ci} . The dependence of signal and background predictions on systematic uncertainties is described by the aforementioned set of nuisance parameters $\boldsymbol{\theta}$, which are parameterized by Gaussian or log-normal priors denoted here as θ_k. Statistical uncertainties of the simulated bin contents are also included as systematic uncertainties. Most systematics are correlated among all the analysis regions and considered to be independent from each other. The validity of this assumption is checked by evaluating the covariance of nuisance parameters.

9.2 Fit Configuration

The binning of $m_{\ell\nu qq}$ in the likelihood fit is determined by the statistical uncertainty of signal mass width. For each signal mass point, the signal mass resolution is given by the fitted Gaussian width of the $m_{\ell\nu qq}$. The fitted signal widths are then fit to a line to give a parameterized signal mass width, as shown in Figures 9.1 and 9.2. Bin widths are set first to this parameterized signal mass resolution. Then if the statistical uncertainty of the data or simulated background is more than 50%, bins are merged until the statistical uncertainty is less than 50%.

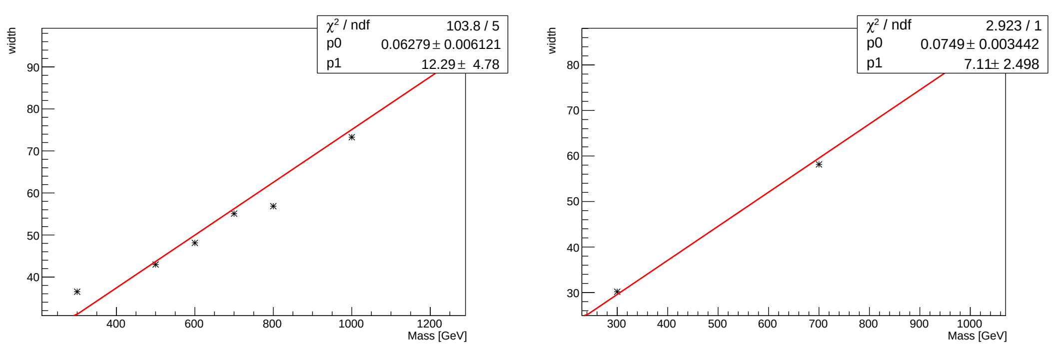

Figure 9.1: The HVT signal mass resolution as a function of mass fit with a straight line in the Resolved ggF region (left) and VBF (right) region.

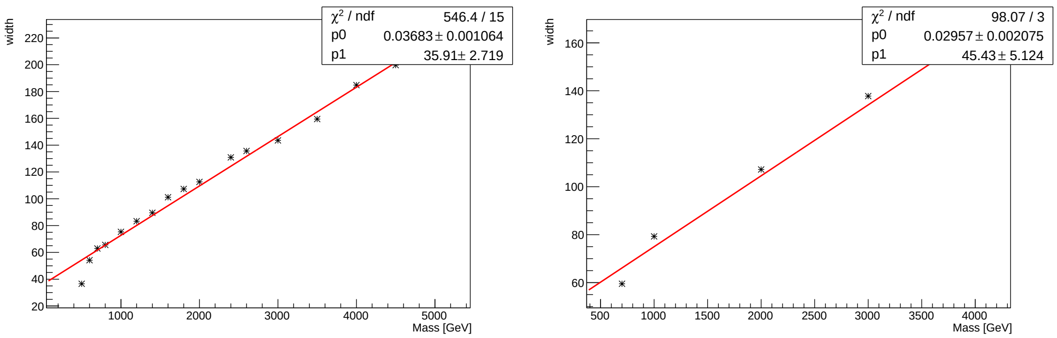

Figure 9.2: The HVT signal mass resolution as a function of mass fit with a straight line in the Merged ggF region (left) and VBF (right) region.

9.3 Best Fit μ

9.4 Discovery Test

9.5 Exclusion Limits

The nominal fit results in terms of μ and θ_μ are obtained from maximizing the likelihood function with respect to all parameters. The test statistic, q_μ, is then constructed as:

$$q_\mu = -2\frac{\mathcal{L}(\mu, \hat{\hat{\theta}}_\mu)}{\mathcal{L}l(\hat{\mu}, \hat{\theta})} \tag{9.2}$$

where $\hat{\mu}$ and $\hat{\theta}$ are the parameter values that maximize the likelihood and $\hat{\hat{\theta}}_\mu$ are the nuisance parameter values that maximize the likelihood for a given μ. As defined, larger values of q_μ correspond to increasing incompatibility between the observed data and the background + signal hypothesis. The observed value of the test statistic, $q_{\mu,obs}$, is then compared to its expected distribution, f_k, to calculate p-values to assess the likelihood of the background+signal hypothesis. Using these distributions, CL_s values are computed as:

$$CL_{s+b} = \int_{q_{\mu,obs}}^{\infty} f(q_\mu|\mu)dq_\mu \tag{9.3}$$

$$CL_b = \int_{q_0^{obs}}^{\infty} f(q_\mu|\mu = 0)dq_\mu \tag{9.4}$$

$$CL_s = \frac{CL_{s+b}}{CL_b} \tag{9.5}$$

CL_{s+b} is the p-value for the signal + background hypothesis and CL_b is the p-value for the background only hypothesis. The CL_s value is interpreted as the probability to observe the background + signal hypothesis normalized to the probability of background-only hypothesis. Normalizing by CL_b prevents setting artificially strong exclusion limits due to downward fluctuations in data.

In this analysis, μ values are scanned for each bin in the fit to find the μ value that yields CL_s=0.05, meaning the likelihood of finding data more incompatiable with the signal+background hypothesis (relative to the background only hypothesis) is 5%. The 95% upper limit on the cross section is then calculated as the product of the μ value found, branching ratio, and theory cross section.

9.6 Fit Configuration

For this analysis, each signal model is fit simultaneously with for the Merged and Resolved channels from VBF and DY production. The WCR and TCR are used to extract the normalizations for the W+jets and $t\bar{t}$ backgrounds in the SRs. The binning is in [Natasha add binning table]. The binning is set by signal resolution and stats. Additionally, talk about NP correlations [Natasha].

Systematics may be affected by low statistics, leading to unsmooth m_{VV} distributions with unphysically large fluctuations. This can lead to artifical pulls and constraints in the fit. To remove such issues a multi-step smoothing procedure is applied to all systematic variation distributions in all regions. First, distributions are rebinned until the statistical error per bin is at least 5%. Next all local extrema are identified. The bins around smallest extrema are iteratively merged until only four local extrema remain. Then distributions are rebinned so that statistical uncertainities in each bin are $< 5\%$.

For some systematics, up and down variations may be in the same direction with respect to the nominal distributions, leading to asymmetric distributions. This causes the variations to not cover the nominal choice, and the interpretation of the confidence interval is skewed. This asymmetry may also lead to unconstrained systematics in the fit. To handle such asymmetric systematics, if the up and down variation for a given systematic are in the same direction for at least three m_{VV} bins the variation is averaged for those bins. The averaging procedure replaces bin-by-bin the up and down variation bins by $b_{\pm}^{new} = b_{nom} \pm \frac{|b_{+} - b_{-}|}{2}$, where b_{nom} is the nominal bin content and $b_{\pm}$ are the original up and down variation bin content. The same procedure is also applied to any variations where the integral of the difference between the up/down variation and the nominal distribution is twice that of the other down/up variation, further ensuring variations are symmetric around the nominal distribution.

Finally, systematics that have a negligible effect on the m_{WV} distribution are not considered in the fit. Shape systematics where no bin in the variational distribution deviates more than 1% from the nominal distribution (after normalizing all histograms to the nominal) are not included in the fit. Also, statistical bin uncertainties $< 1\%$ are ignored.

Part IV

Results

Chapter 10

Fitted Systematics

add Ranking plots add Correlations add Asimov pulls

Chapter 11

Fit Results

yield table background xs limits

Part V

Quark and Gluon Tagging

Chapter 12

Prospects

For the resolved analysis, signal jets are quark enriched and background jets are gluon dominated. By classifying jets in the event as quark or gluon initiated, less background would contaminate the signal region. Figure 12.1 shows the PDGID for the truth parton matched to the jet (meaning the highest energy parton in the jet catchment area) in events passing the resolved signal region selections. PDGID = -1 corresponds to pileup jets, $0 <$ PDGID < 6 correspond to quarks and PDGID = 21 corresponds to gluons. From this Figure, it is evident that are notable fraction of the background that contaminates the signal region contains gluon jets, especially for the sub-leading jet.

As gluons jets have more constituents and therefore more tracks (n_{trk}), the background jets have more tracks than the signal jets. This is shown in Figure 12.2. Therefore, by cutting on the number of tracks in a jet, quark and gluon jets may be distinguished (i.e. jets with less than a given number of tracks are classified as a quark, otherwise the jet is classified as a gluon.) Moreover, as the momentum of the jet increases the number of tracks also increases logarithmically. Therefore by applying a cut on the number of tracks that scales with the $ln(p_T)$ is more powerful than a threshold cut on the number of tracks. Figure 12.3-

Figure 12.6 show normalized heat maps of $ln(p_T)$ vs the number of reconstructed tracks for the background and a 300 GeV Z' signal. In these plots it is evident that the number of tracks in the background jets grows more quickly with $ln(p_T)$ than for the signal jets. This is expected given that the signal is quark dominated and the background is gluon dominated.

In Figure 12.8 is the ROC Curve for quark gluon tagging with cut on the number of tracks in a jet that depends on $ln(p_T)$. The sum of the backgrounds in the signal region were used for this curve. Here the quark tagging efficiency is the ratio of quarks tagged as quarks to the total number of quarks in the signal region. The gluon rejection is calculated as the reciprocal of the gluon tagging efficiency. Choosing a 90 efficient working point with a rejection of 1.4 corresponds to a slope of 4 and intercept of -5. Focusing on the background in Figure 12.9, this cut helps minimize gluon contamination in the signal region. Also, from these heat maps it is obvious that the number of tracks in gluon jets grows more quickly than those in quark jets.

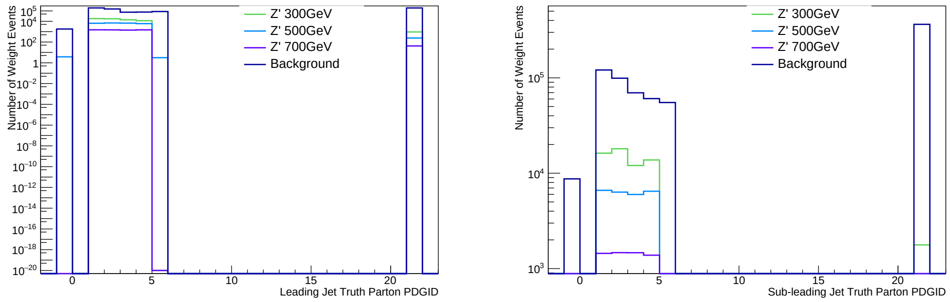

Figure 12.1: PDGID of the truth-level parton matched to the small-R jets passing the Resolved GGF WW Signal Region selections for the (a) Leading (b) Sub-Leading jets . These distributions are shown for 300, 500, and 700GeV Z' signals and the background.

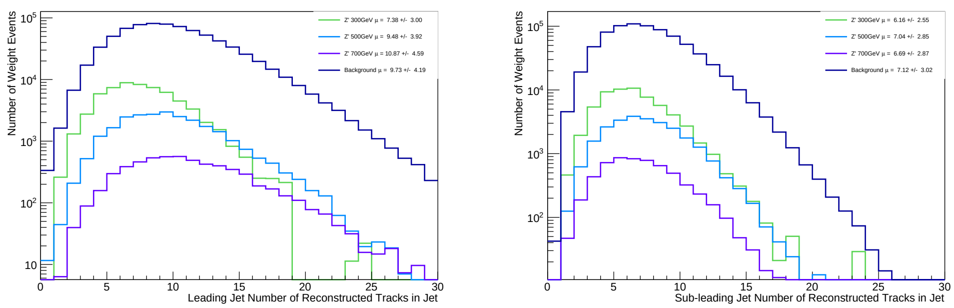

Figure 12.2: The number of tracks in small-R jets in events passing the Resolved GGF WW Signal Region selections for the (a) Leading (b) Sub-Leading jets. These distributions are shown for 300, 500, and 700GeV Z' signals and the background.

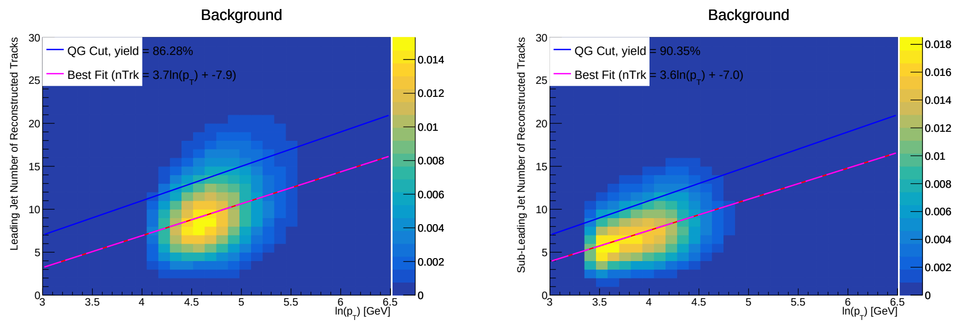

Figure 12.3: The number of tracks in background small-R jets in events passing the Resolved GGF WW Signal region selection vs. $ln(p_T)$ for (a)Leading (b) Sub-Leading jets. The best fit line for the distribution is also shown, as well as the percentage of jets that pass a cut of number of tracks $< 4 \times ln(p_T) - 5$. Note the number of total entries in these plots has been normalized to one.

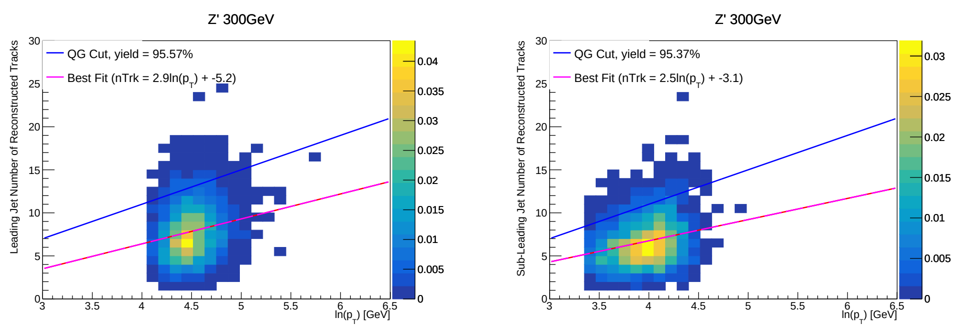

Figure 12.4: The number of tracks in small-R jets in 300GeV Z' events passing the Resolved GGF WW Signal region selection vs. $ln(p_T)$ for (a)Leading (b) Sub-Leading jets. The best fit line for the distribution is also shown, as well as the percentage of jets that pass a cut of number of tracks $< 4 \times ln(p_T) - 5$.Note the number of total entries in these plots has been normalized to one.

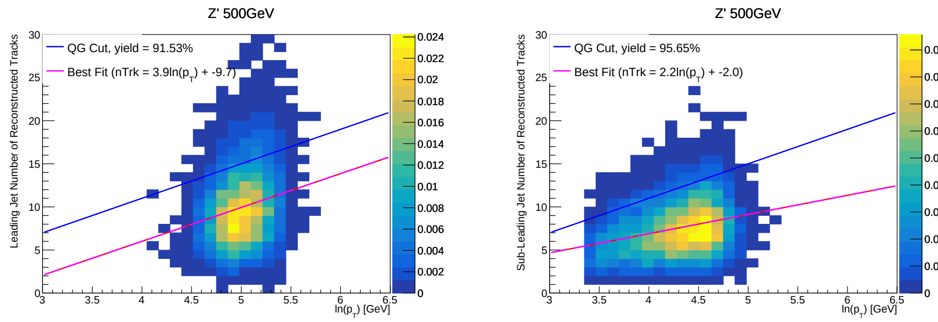

Figure 12.5: The number of tracks in small-R jets in 500GeV Z' events passing the Resolved GGF WW Signal region selection vs. $ln(p_T)$ for (a)Leading (b) Sub-Leading jets. The best fit line for the distribution is also shown, as well as the percentage of jets that pass a cut of number of tracks $< 4 \times ln(p_T) - 5$.Note the number of total entries in these plots has been normalized to one.

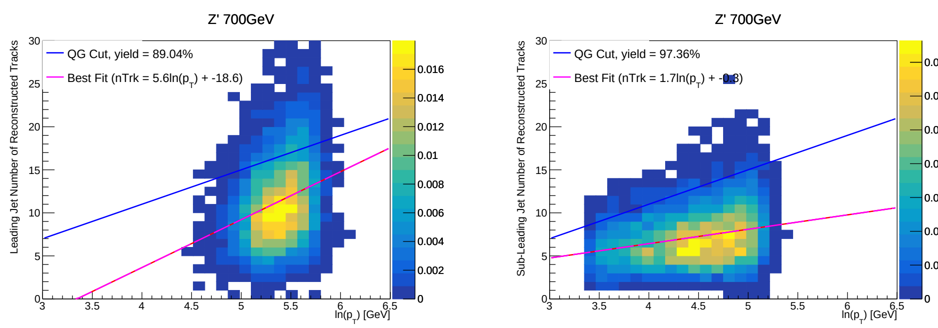

Figure 12.6: The number of tracks in small-R jets in 700GeV Z' events passing the Resolved GGF WW Signal region selection vs. $ln(p_T)$ for (a)Leading (b) Sub-Leading jets. The best fit line for the distribution is also shown, as well as the percentage of jets that pass a cut of number of tracks $< 4 \times ln(p_T) - 5$.Note the number of total entries in these plots has been normalized to one.

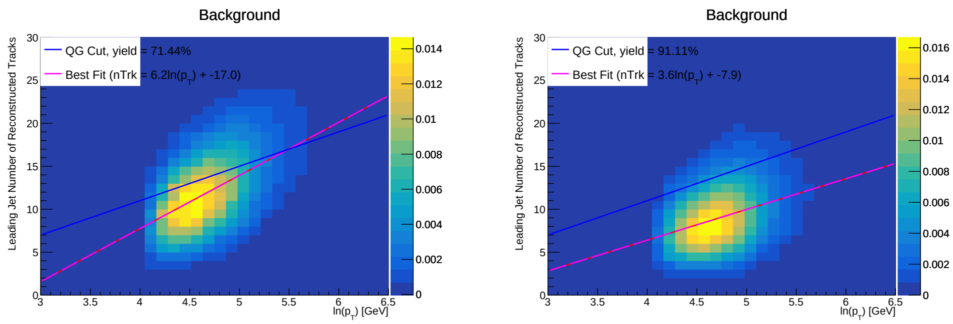

Figure 12.7: The number of tracks in leading small-R jets in background events passing the Resolved GGF WW Signal region selection vs. $ln(p_T)$ for (a)Gluons (b) Quarks jets. The best fit line for the distribution is also shown, as well as the percentage of jets that pass a cut of number of tracks $< 4 \times ln(p_T) - 5$.Note the number of total entries in these plots has been normalized to one.

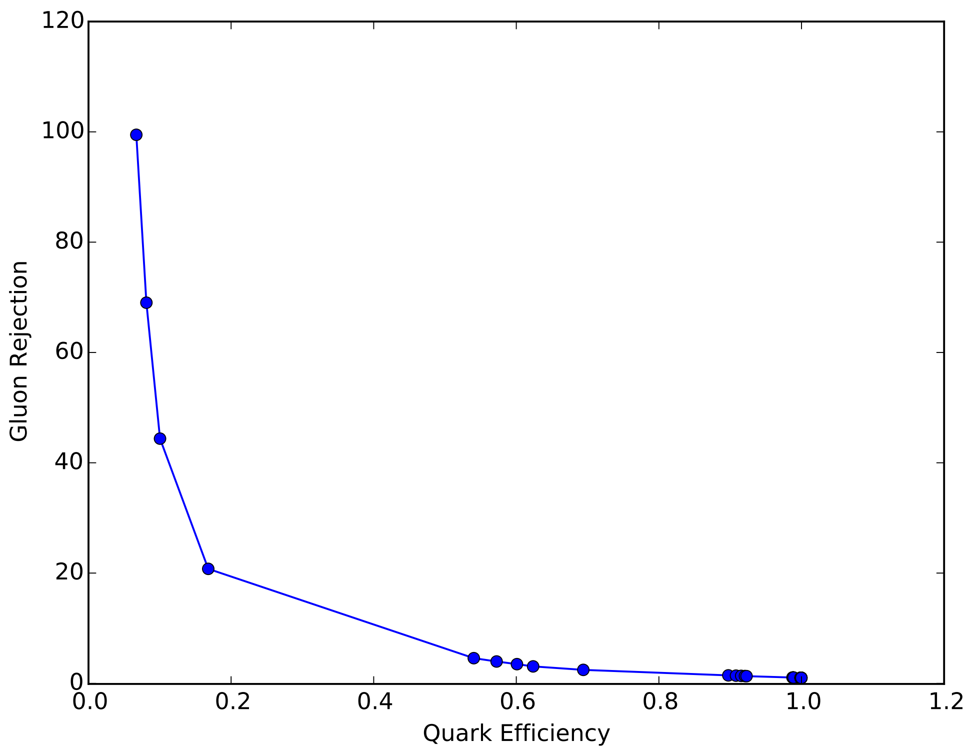

Figure 12.8: ROC Curve for Quark and Gluon Tagging with a cut on the number of tracks that depends on the $ln(p_T)$.

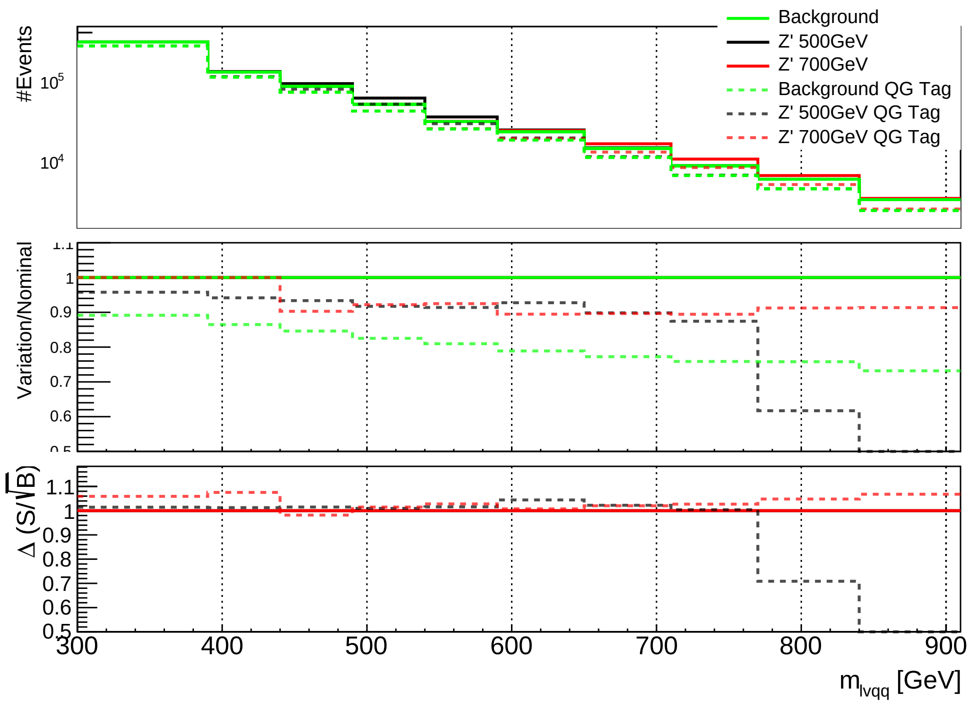

Figure 12.9: The top panel shows the distribution of m_{lvqq} with and without quark gluon tagging. The middle panel shows the ratio of the signals and backgrounds with and without quark gluon tagging. The bottom panel shows the change in $S/\sqrt{B}$ with quark gluon tagging.

Chapter 13

n_{trk} Calibration

As tagger based on nTrk cuts on the number of tracks in jets, a quantity that is not known with infinite precision, relevant systematic uncertainties must be evaluated. The sources of uncertainty in n_{trk} may be split into modeling and experimental uncertainties.

Modeling uncertainties are obtained by assessing PDF and ME uncertainties on the number of charged particles in particle-level jets in dijet events. The number of charged particles as a function of jet p_T is calculated using an Iterative Bayesian (IB) technique [cite paper].

This measurement ([7]) uses the ATLAS 2012 pp collision dataset, corresponding to 20.3/fb at center-of-mass energy $\sqrt{s} = 8$TeV. Monte Carlo (MC) samples are used to determine the response matrix. The MC sample is a dijet sample generated with Pythia 8.175 using CT10 PDF and AU2 tune. The anti-k_T algorithm is used to cluster jets with a radius parameter R = 0.4. Jets are required to have $|\eta| < 2.1$. Tracks in jets are required to have $p_T > 500 MeV$, $|\eta| < 2.5$, track-fit $\chi^2 < 3.0$ and originate from the primary vertex. Matching tracks to jets is accomplished using ghost-association [cite]. In this technique, jets are re-clustered with the track collection augmented with "ghost" versions of tracks. These "ghosts" tracks have the same direction as their parent track, but infinitesimal track p_T. This insures meta-jet properties (e.g. η, p_T, etc) are unchanged. A track is matched to a jet if it's ghost version remains in the jet after re-clustering. Further details of the data, object, and event selection may be found in [cite 35].

To select dijet topologies events are required to have at least two jets with $p_T > 50GeV$ that are relatively well-balanced ($p_T^{lead}/p_T^{sub-lead} < 1.5$).

In the IB technique, the prior distribution and number of iterations are the inputs [cite Bayesian paper]. The IB response matrix connects number of charged particles to the number of tracks in jets determined using the simulated samples. This response matrix is used to unfold data to extract the n_c. Before applying the response matrix a fake factor is applied. This accounts for jets that pass detector level selections, but not particle level selections. Following this, the IB method iteratively applies the response matrix using the nominal Pythia 8.175 sample as a prior. The number of IB iterations is chosen to minimize unfolding bias and statistical fluctuations. For this measurement four iterations was found to be optimal by minimizing the unfolding bias from pseudodata simulated with Herwig++ with a prior from Pythia 8 AU2. Finally, the inefficiency factor is applied to account for events passing particle level selection but not detector level, yielding the unfolded nCharged distribution.

This process is prone to three main sources of bias: response matrix, correction factor, and unfolding procedure uncertainties. The response matrix is sensitive to experimental uncertainties impacting jet track reconstruction and calorimeter jet p_T. Correction factors are also sensitive to experimental uncertainties (e.g. JES) as such uncertainties modify detector level acceptance. Sensitivity to particle level acceptance is calculated by comparing Pythia and Herwig. Finally, the bias from the IB prior choice is determined by reweighting the particle-level spectrum, so the simulated detector level spectrum more closely matches the uncorrected data. Unfolding this modified detector-level simulation and comparing it re-weighted particle-level spectrum indicates bias from the prior distribution choice.

A summary of all the systematic uncertainties associated with this unfolding may be found in [ref paper]. Total uncertainties are $< 7\%$ for the number of charged particles in jets. The unfolded distribution of the nCharged in jets from data are further analyzed to extract the quark and gluon nCharged distributions. In dijet events, the jet with a larger η is more energetic and therefore more likely to be a quark. This is due to the quarks in protons generally having a larger fraction of the total momentum of the proton constituents. The more central jet is more likely to be a gluon-initiated jet. This correlation between jet η and flavor may then be used to extract nCharged in p_T bins using:

$$< n_c^f >= f_q^f < n_c^q > + f_g^f < n_c^g > \tag{13.1}$$

$$< n_c^c >= f_q^c < n_c^q > + f_g^c < n_c^g > \tag{13.2}$$

In this equation the f and c subscripts denote the more forward and central jets, respectively. The q and g subscripts denote quark and gluon. The fraction of more forward jets that are say gluons is denoted by f_g^f. The other relevant jet fractions are denoted with the same naming scheme. Finally, $< n_c >$ is the average number of charged particles in a jet in a given p_T bin. To show that Eq. (**??**) may be used to extract quark and gluon n_c distributions the extracted distributions are compared to n_c distributions determined using the jet flavor in simulation. Figure [add figure natasha] shows that the extracted and true distributions differ by $< 1\%$ over the p_T ranged probed for this study. Moreover, this implies that n_c depends only on the flavor of the initiating parton and jet p_T.

These extracted distributions are prone to PDF and ME biases. The bias from the choice of the CT10 PDF for the Pythia sample is accounted for by comparing quark/gluon fractions for the nominal CT10 sample with its eigenvector variations. Comparing the quark/gluon fractions from Pythia 8 and Herwig++ quantify the uncertainity from the ME calculation. These uncertainities are added in quadrature with the unfolding uncertainity to give the total modelling uncertainity on the extracted n_c distribution. This is shown in Figure 14.2.

To apply these uncertainities in n_c distributions in data, per-jet event weights are associated with each uncertainity according to:

$$w_i(n_c) = \frac{P(n_c| < n_c > \pm\sigma^i_{n_c})}{P(n_c| < n_c >)} \tag{13.3}$$

In Eq. (**??**), i denotes the uncertainty considered, P is the Poisson probability, and $\sigma^i_{n_c}$ represents the average impact of the uncertainity on n_c.

The previous uncertainties described accounted for modeling uncertainty associated with the number of charged particles in a jet. However, n_c is not a measurable quantity. Instead the number of tracks in a jet is measured, which is a proxy for n_c. Therefore the uncertainties associated with the measurement of nTracks must also be considered ([9]). These uncertainties were calculated using a Pythia 8 dijet sample with NNPDF 23. Track reconstruction efficiency and fake rates are the dominant sources of nTrack uncertainties.

The track reconstruction efficiency is effected by the uncertainty of the description of the ID material in simulation and the modeling of charged-particle interactions with this material. These uncertainties are accounted for by varying the ID material by 5-25% (dependent on the region of the detector considered). The difference in the tracking efficiency between the nominal and varied simulation give the uncertainty on the track reconstruction efficiency. Another important source of track reconstruction efficiency arises in the core of jets. The high density of tracks in the jet cores can cause ID clusters to merge. The fraction of lost tracks due to merging is given by the fraction of tracks that have a charge of two minimum ionizing particles. This quantity is compared between data and simulation resulting in an uncertainty of 0.4% on tracks with $\Delta R < 0.1$. Combining these effects gives a total uncertainty as a function of p_T and η that is generally $< 2\%$ [references figure 44 from [9]).

Fake tracks are the other dominant source of nTrk uncertainity. Fake tracks are tracks that cannot be associated to a single particle. Often these tracks are a result of random combinations of hits from charged particles that overlap in space. In dense environments, such as the core of jets or high-pileup environments, fake tracks are more likely. Fake tracks are estimated with a 'control region method' which is briefly summarized here [[8]]. By applying a series of track selections to enrich the fraction of fake tracks (e.g. $|d_0| > 0.1$, track $\chi^2 > 1.4$, etc) in simulation, templates for fake track parameters are calculated. These templates are then fit to data to determine the fraction of fake tracks. On average the fake rate is found to be 30% (independent of p_T and η).

To assess the impact of these two detector level uncertainties, tracks are randomly dropped according to the rates described above. Reconstruction and fake uncertainties both lower the number of tracks, hence these uncertainties are one-sided. By dropping tracks in this way a varied nTrk distribution is calculated for both uncertainties. The associated per-jet event weights are then calculated in the same way as the modeling weights as:

$$w_i(n_c) = \frac{P(n_{trk}| < n_{trk} > \pm\sigma^i_{n_{trk}})}{P(n_{trk}| < n_{trk} >)} \tag{13.4}$$

Adding the modeling and detector level uncertainties in quadrature gives the overall nTrack uncertainty. The effects of the individual uncertainties on the nTrk distributions can be seen in Fig 14.4. Fig 14.3 shows the m_{lvqq} and nTrk distributions for the W and Top control regions before likelihood fitting. In these plots the nTrk uncertainties improve agreement between data and MC. The remaining differences are likely covered by likelihood fitting and improving the analysis itself.

Chapter 14

Application

Using the 90% WP of the n_{trk} tagger improves $S/\sqrt{B}$ is $< 3\%$ as shown in Figure 12.9. Although, n_{trk} is the single most powerful discriminating variable for quark and gluon jets, the addition of other jet variables would improve the classification efficiency. Figure 14.1 shows the possible improvement of 10% in jet classification using the truth label of the jets to classify jets. This type of improvement is possible by using variables such as jet width, and energy correlatators. Figure [add BDT figure/use 1612.01551.pdf] shows for a 90% quark tagging efficiency for a 100 GeV jet, a BDT improve the gluon rejection by 0.4. Once this tagger is calibrated it would improve the analysis sensitivity of this channel.

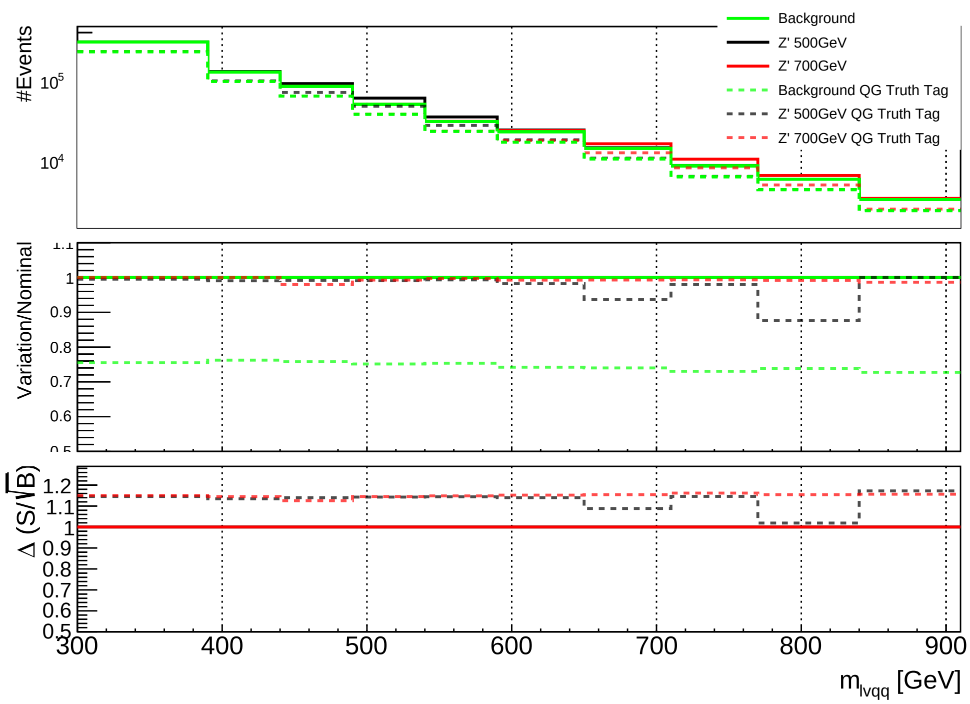

Figure 14.1: The top panel shows the distribution of m_{lvqq} with and without requiring jets to be true quarks. The middle panel shows the ratio of the signals and backgrounds with and without requiring jets to be true quarks. The bottom panel shows the change in $S/\sqrt{B}$ when requiring jets to be true quarks..

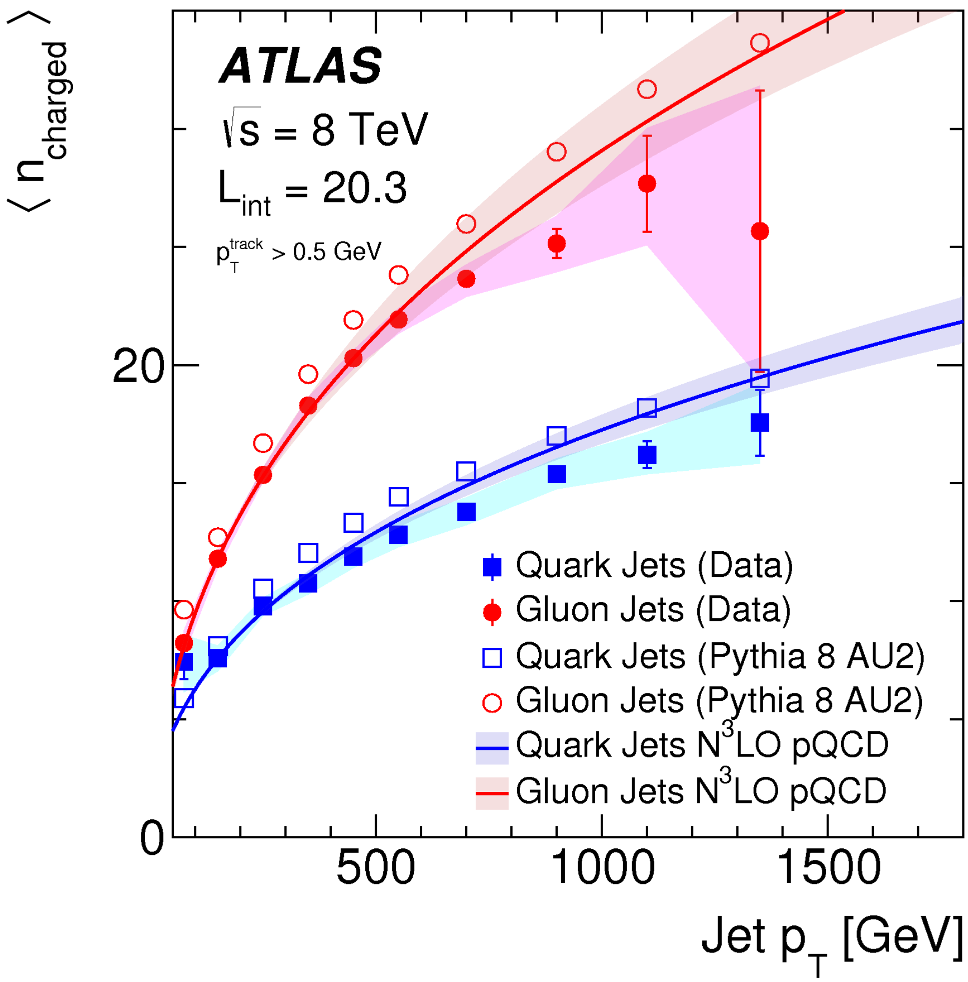

Figure 14.2: Unfolded and extracted n_C qg dstbs..

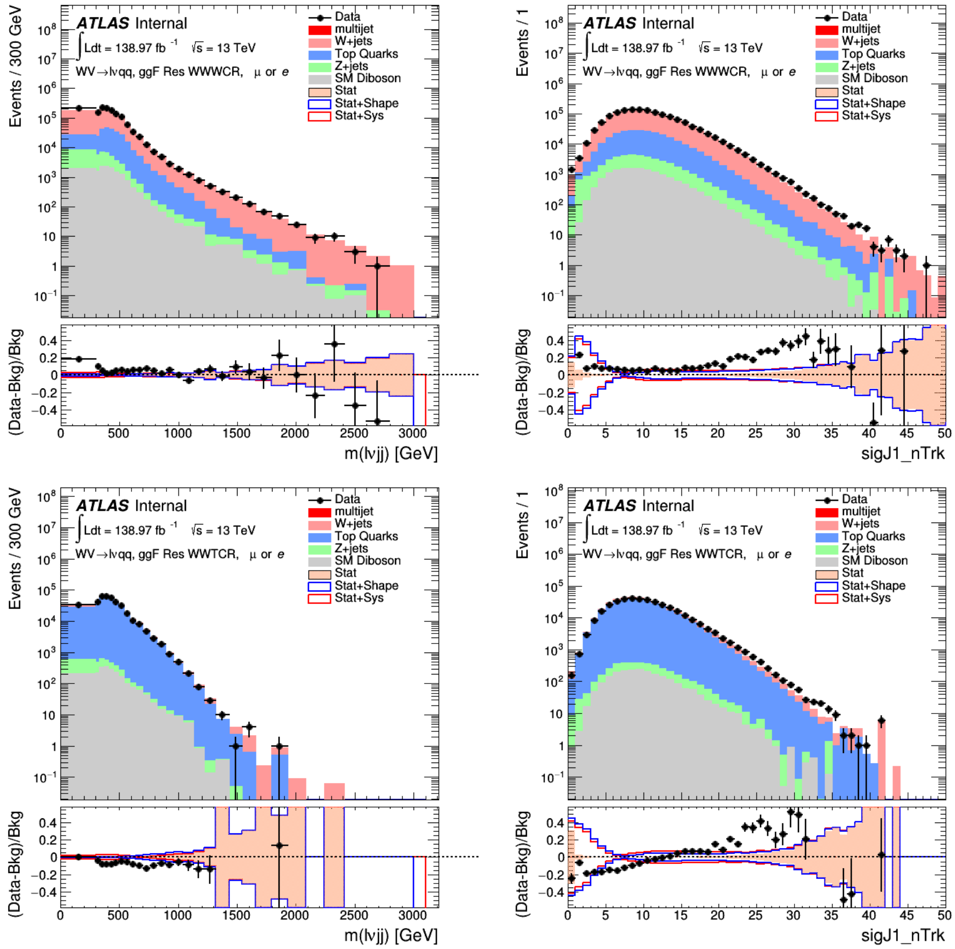

Figure 14.3: PDGID of the truth-level parton matched to the small-R jets passing the Resolved GGF WW Signal Region selections for the (a) Leading (b) Sub-Leading jets . These distributions are shown for 300, 500, and 700GeV Z' signals and the background.

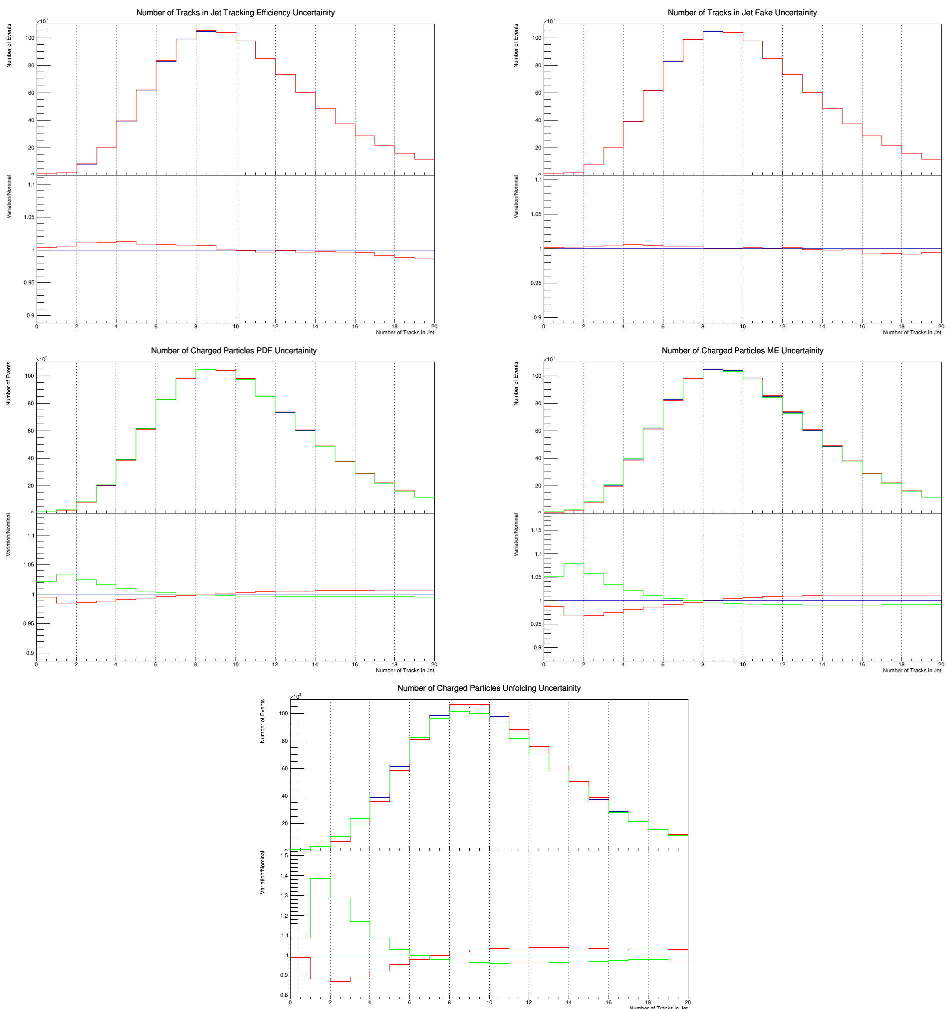

Figure 14.4: These figures show the impact of the uncertainities on the number of tracks in the leading jet in the sum of the background sample in the Resolved GGF WW SR (a) tracking efficiency (b) fake (c) PDF (d) ME (e) unfolding uncertainties.

Part VI

Conclusion

Chapter 15

Conclusions

This is where conclusions go.

Bibliography

[1] Lecture notes particle physics ii.

[2] Kaustubh Agashe, Hooman Davoudiasl, Gilad Perez, and Amarjit Soni. Warped Gravitons at the LHC and Beyond. *Phys. Rev.*, D76:036006, 2007.

[3] G. Altarelli and G. Parisi. Asymptotic freedom in parton language. *Nuclear Physics B*, 126(2):298 – 318, 1977.

[4] ATLAS Collaboration. Atlas muon reconstruction performance in lhc run 2.

[5] ATLAS Collaboration. Summary plots from the atlas standard model physics group.

[6] ATLAS Collaboration. Jet energy scale measurements and their systematic uncer- tainties in proton–proton collisions at $\sqrt{s} = 13$ tev with the atlas detector. arXiv: 1703.09665 [hep-ex].

[7] ATLAS Collaboration. Measurement of the charged-particle multiplicity inside jets from s=$\sqrt{8}$ tev pp collisions with the atlas detector. arXiv:1602.00988 [hep-ex].

[8] ATLAS Collaboration. Performance of the atlas track reconstruction algorithms in dense environments in lhc run 2. arXiv:1704.07983 [hep-ex].

[9] ATLAS Collaboration. Properties of jet fragmentation using charged particles measured with the atlas detector in pp collisions at $\sqrt{s}$ =13 tev. arXiv:1906.09254 [hep-ex].

[10] Alex Dias and V. Pleitez. Grand unification and proton stability near the peccei-quinn scale. *Physical Review D*, 70, 07 2004.

[11] Stefan Höche, Frank Krauss, Marek Schönherr, and Frank Siegert. Qcd matrix elements + parton showers. the nlo case. *Journal of High Energy Physics*, 2013(4), Apr 2013.

[12] Gregory Soyez Matteo Cacciari, Gavin P. Salam. The anti-k_T jet clustering algorithm. arXiv:0802.1189 [hep-ph].

[13] Duccio Pappadopulo, Andrea Thamm, Riccardo Torre, and Andrea Wulzer. Heavy vector triplets: bridging theory and data. *Journal of High Energy Physics*, 2014(9), Sep 2014.

[14] Antonio Pich. The Standard Model of Electroweak Interactions. In *Proceedings, High-energy Physics. Proceedings, 18th European School (ESHEP 2010): Raseborg, Finland, June 20 - July 3, 2010*, pages 1–50, 2012. [,1(2012)].

[15] Lisa Randall and Raman Sundrum. A Large mass hierarchy from a small extra dimension. *Phys. Rev. Lett.*, 83:3370–3373, 1999.

[16] Tania Robens and Tim Stefaniak. Lhc benchmark scenarios for the real higgs singlet extension of the standard model. *The European Physical Journal C*, 76(5), May 2016.